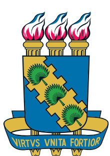

UNIVERSIDADE FEDERAL DO CEARÁ
CENTRO DE CIÊNCIAS
DEPARTAMENTO DE FÍSICA
PROGRAMA DE PÓS-GRADUAÇÃO EM FÍSICA

UNIVERSITEIT ANTWERPEN
FACULTEIT WETENSCHAPPEN
DEPARTEMENT FYSICA

LUCAS DE PAULA MIRANDA

ELECTRONIC TRANSPORT IN TWO DIMENSIONAL SYSTEMS WITH DEFECTS

TRANSPORTE ELETRÔNICO EM MATERIAIS DE DUAS DIMENSÕES COM DEFEITOS

ELEKTRONISCH TRANSPORT IN TWEEDIMENSIONALE SYSTEMEN MET DEFECTEN

FORTALEZA
2022

LUCAS DE PAULA MIRANDA

ELECTRONIC TRANSPORT IN TWO DIMENSIONAL SYSTEMS WITH DEFECTS

TRANSPORTE ELETRÔNICO EM MATERIAIS DE DUAS DIMENSÕES COM DEFEITOS

ELEKTRONISCH TRANSPORT IN TWEEDIMENSIONALE SYSTEMEN MET DEFECTEN

Tese apresentada ao Curso de Pós-graduação em Física da Universidade Federal do Ceará como parte dos requisitos necessários para a obtenção do título de Doutor em Física. Áread de concetração: Física.

Orientador:
Prof. Dr. Raimundo Nogueira da Costa Filho
Co-orientador:
Prof. Dr. François M. Peeters

FORTALEZA
2022

Dados Internacionais de Catalogação na Publicação
Universidade Federal do Ceará
Sistema de Bibliotecas
Gerada automaticamente pelo módulo Catalog, mediante os dados fornecidos pelo(a) autor(a)

M644t Miranda, Lucas de Paula.
Transporte eletrônico em materiais de duas dimensões com defeitos / Lucas de Paula Miranda. – 2022.
104 f. : il. color.

Tese (doutorado) – Universidade Federal do Ceará, Centro de Ciências, Programa de Pós-Graduação em Física , Fortaleza, 2022.
Orientação: Prof. Dr. Raimundo Nogueira da Costa Filho.
Coorientação: Prof. Dr. François M. Peeters.

1. Transporte eletrônico. 2. Nanomateriais. 3. Efeitos de vacâncias. I. Título.
CDD 530

LUCAS DE PAULA MIRANDA

ELECTRONIC TRANSPORT IN TWO DIMENSIONAL SYSTEMS WITH DEFECTS

TRANSPORTE ELETRÔNICO EM MATERIAIS DE DUAS DIMENSÕES COM DEFEITOS

ELEKTRONISCH TRANSPORT IN TWEEDIMENSIONALE SYSTEMEN MET DEFECTEN

Tese de doutorado apresentada ao Curso de Pós-graduação em Física da Universidade Federal do Ceará como parte dos requisitos necessários para a obtenção do título de Doutor em Física. Área de concentração: Física.

Aprovada em: 29/08/2022.

BANCA EXAMINADORA

Prof. Dr. Raimundo Nogueira da Costa Filho
Departamento de Física – UFC

Prof. Dr. François Maria Leopold Peeters (Co-orientador)
Department of Physics - University of Antwerp
Belgium

Prof. Dr. Diego Rabelo da Costa (Co-orientador)
Departamento de Física – UFC

Prof. Dr. Andrey Chaves
Departamento de Física – UFC

Prof. Dr. André Jorge Carvalho Chaves
Instituto Tecnológico da Aeronática – ITA

To my family,

to my friends

and everyone who helped me during this journey.

ACKNOWLEDGMENTS

First, I would like to thanks my parents João Artur and Maria Irlanda for all their support and care. To my brother and sister, for company and strives during these years. Also to my uncle Afrânio Fonseca for his support, care and thoughts specially during these last years.

I am greatly grateful to my supervisor Professor Raimundo Nogueira da Costa Filho for all the guidance, support, friendship and (a lot of) patience. Since my first as a physics he has been giving not only academic teachings but also life and personal advices that brought me to where I am.

To all of my professors in academic for their great (and hard) lessons. I am specially thanks to Professor François Peeters for his support and attention during my time in Antwerp. And also to Professor Diego Rabelo da Costa whom only recently I started to work but has being immensely helpful and insightful.

To all of my friends that were present and carried me during this years. There were many that walked with me and changed the way I see the world. Among them, Daniel Brito, Mardãnio França, Raul Victor and Ramon Sampaio helped me to endure the hard and harder times of my academic years. Specially I am grateful to Isabel Cordeiro, a special and bright person that was present during my hardest times and helped me carry it through.

To Misael Moura (li!), Emanuel Fonteles, Sofia Magalhães, Vandeley Junior, Junior de Schrödinger, Barbara Sales, and many others for the company during my academic life.

To Slaviša Milovanović, Claudia Strambini, Rai Menezes, Sara Conti and Nikolas Garofil, for made my time abroad much more enjoyable.

To many others that direct and indirectly contribute to my academic development.

I also would like to thanks CAPES and the Flemish Science Foundation (FWO) for the financial support that made this work possible

ABSTRACT

The pursuit for the next generation of nanodevices made scientists focus the attention to two dimensional materials. Experimental works of two dimensional materials are hardly free of structural defects, which, in turn, modify drastically the physical properties of its defect-free counterpart. In this work the presence of structural defects is study in two different materials. First, the dependence of the Hall, bend and longitudinal resistances to a perpendicular magnetic field and to vacancy defects in a four-terminal phosphorene single layer Hall bar is investigated. A tight-binding model in combination with the Landauer-Büttiker formalism is used to calculate the energy spectrum, the lead-to-lead transmissions, and the Hall and bend resistances of the system. It is shown that the terminals with zigzag edge orientation are responsible for the absence of quantized plateaus in the Hall resistance and peaks in the longitudinal resistance. A negative bend resistance in the ballistic regime is found due to the presence of high- and low- energy transport modes in the armchair and zigzag terminals, respectively. The system density of states, with single vacancy defects, shows that the presence of in-gap states is proportional to the number of vacancies. Quantized plateaus in the Hall resistance are only formed in a sufficiently clean system. The effects of different kinds of vacancies in the regime where the quantized plateaus are destroyed and a diffusive regime appears in the bend resistance are investigated. Next, we explore effects due to point defect clustering on the electronic and transport properties of bilayer graphene nanoribbons, for AA and AB stacking and zigzag and armchair boundaries, by means of the tight-binding approach and scattering matrix formalism. Evidence of vacancy concentration signatures exhibiting a maximum amplitude and an universality regardless of the system size, stacking and boundary types, in the density of states around the zero-energy level are observed. Our results are explained via the coalescence analysis of the strong sizeable vacancy clustering effect in the system and the breaking of inversion symmetry at high vacancy densities, demonstrating a similar density of states for two equivalent degrees of concentration disorder, below and above the maximum value.

Keywords: electronic transport; nanomaterials; vacancies effects.

RESUMO

A busca pela próxima geração de nanodispositivos fez com que cientistas concentrassem a atenção nos materiais bi-dimensionais (2D). Realizações experimentais de materiais 2D dificilmente estão livres de defeitos estruturais, o que, por sua vez, modificam drasticamente suas propriedades físicas em relação ao seu sistema livre de defeitos. Neste trabalho a presença de defeitos estruturais é estudada em dois materiais diferentes. Primeiramente investigamos a dependência das resistências Hall, *bend* e logintudinal em relação a aplicação de um campo magnético e defeitos de vacância em uma barra Hall de fosforeno com quatro terminais. Um modelo *tight-binding*, em combinação com o o formalismo de Landauer-Büttiker, é usado para calcular o espectro de energia, a transmissões entre terminais e as resistências do sistema. Em trabalhos anteriores foi mostrado que os terminais com orientação *zigzag* são responsáveis por a ausência de platôs quantizados na resistência Hall e picos na resistência longitudinal. Uma resistência *bend* negativa no regime balístico é encontrados devido à presença de modos de transporte de alta e baixa energia no terminais *armchair* e *zigzag*, respectivamente. A densidade de estados do sistema, com defeitos de vacância única, mostra que a presença de estados *in-gap* é proporcional ao número de vacâncias. Platôs quantizados na resitência Hall são formadas apenas em um sistema suficientemente livre de defeitos. Os efeitos de diferentes tipos de vacâncias são investigados analisando a destruição dos platôs quantizados e através da presença de um regime difusivo aparece na resistência *bend*. Em seguida, exploramos os efeitos devidos ao agrupamento de defeitos pontuais nas propriedades eletrônicos e de transporte de nanofitas de grafeno de camada dupla, para empilhamento AA e AB e bordas em *zigzag* e *armchair*, usando modelos *tight-binding* e formalismo da matriz de espalhamento. Assinaturas evidentes de concentração de vacâncias exibindo uma amplitude máxima e uma universalidade, independentemente do sistema tamanho, empilhamento e tipos de borda, na densidade de estados ao redor do nível de energia zero são observados. Nossos resultados são explicados através da análise coalescência do forte efeito de agrupamento de vacâncias no sistema e a quebra da simetria de inversão em altas densidades de vacância, demonstrando uma densidade semelhante de estados para dois valores equivalentes de concentração de desordem, abaixo e acima do valor máximo.

Palavras-chave: transporte eletrônico; nanomateriais; efeitos de vacâncias.

ABSTRACT

Het streven naar de volgende generatie van nano-apparaten heeft de aandacht van wetenschappers gebrachtnaar tweedimensionale materialen. Experimentele realisaties van tweedimensionale materialen zijn nauwelijks vrij van structurele defecten, die drastisch fysieke eigenschappen heeft van zijn defectvrij tegenhanger. In dit werk worden de transporteigenschoppen in de aanwezigheid van structurele defecten bestudeerd in twee verschillende materialen. In eerste instantie, voordt de afhankelijkheid van de Hall en buigweerstanden op een loodrecht magnetisch veld en op vacaturedefecten bestudeert in een vier-terminal fosforeen-enkel laag Hall bar. Een *tight-binding* model in combinatie met de Landauer-Büttiker formalisme wordt gebruikt om het energiespectrum te berekenen, de *lead-to-lead* transmissies en de Hall en buig weerstand van het systeem. We vonden dat de terminals met *zigzag* randen verantwoordelijk zijn voor: de afwezigheid van gekwantiseerde plateaus in de Hall-weerstand en pieken in de longitudinale weerstand. Een negatieve buig weerstand is gevonden in het ballistische regime vanwege de aanwezigheid van hoog- en laag-energetische transportmodi in de *armchair* en *zigzag* terminals, respectievelijk. De dichtheid van toestanden, met enkele vacaturedefecten, laat zien dat de aanwezigheid van in-gap-toestanden evenredig is met het aantal vacatures. Gekwantiseerde plateaus in de hal weerstanden worden alleen gevormd in een voldoend defect vrij systeem. De effecten van verschillende soorten vacatures in het regime waar de plateaus worden vernietigd en een diffuus regime verschijnt in de buig weerstand worden onderzocht. Vervolgens onderzoeken we effecten als gevolg van clustering van puntdefecten op de elektronische en transporteigenschappen van tweelagige graphene nanoribbons, voor AA- en AB-stapeling en *zigzag* en *armchair* randen, doormiddel van een *tight-binding* aanpak en het verstrooiingsmatrix formalisme. Evidentie van vacatureconcentratie effecten die een maximale amplitude en een universaliteit vertonen, ongeacht de grootte van het systeem, stapeling en randtypes, in de toestanden dichtheid rond het nul-energieniveau worden waargenomen. Onze resultaten worden verklaard via de coalescentie analyse van het sterke vacature clustering effect en het doorbreken van de inversiesymmetrie bij hoge clustersdichtheden, wat een vergelijkbare van toestands dichtheid voor twee equivalente graden van concentratiestoornis, onder en boven de maximale waarde.

Keywords: elektronische transporten; nano-materialen; vacaturedefecten effecten.

LIST OF FIGURES

1.1 Relation between the number of transistors in a processor against the device size throughout the years. Data retrived from: <https://en.wikipedia.org/wiki/Transistor_count> and <https://ourworldindata.org/grapher/transistors-per-microprocessor>. 22

1.2 (a) The schematic of a n-type AlGaAs and intrisic GaAs heterojunction before and (b) after the charge transfer. Figure adapt from *Datta, S.* (1995). *Electronic Transport in Mesoscopic Systems*. 23

1.3 Different carbon allotrope: (a) fullerenes, (b) carbon nanotubes, (c) graphene and (d) graphite. Figure modified from *Sensors and Actuators B* 173 (2012) 1-21. 24

1.4 (a) Perspective side view of few-layer phosphorene. (b) DFT-HSE06 results for the dependence of the energy gap in few-layer phosphorene on the number of layers. (c) Hall coefficient (blue curve) and conductance (red curve) as a function of gate voltage collected from a 8-nm-thick sample on Si substrate with 285 nm SiO_2. Images from *ACS Nano* 2014, 8, 4, 4033–4041 (a-b) and *Nature Nanotechnology* volume **9**, pages 372–377 (2014) (c). . . . 25

1.5 (a) Comparison between graphene and BLG band dispersion at Dirac point. Figure adept from Am. J. Phys, **77** (7), July 2009. (c) Schematics for biased AB-stack BLG and (d) band structure near the Dirac points for V = 0.15 eV (solid line) and V = 0 eV (dashed line) and. Figure adapted from Phys. Rev. Lett. **99**, 216802. (b) Moiré pattern as seen in twisted BLG and the mini Brillouin zone, which is the (e) reciprocal Moiré superlattice. Figure adapted from Nature volume **556**, pages 80–84 (2018) 27

1.6 Defects in highly oriented pyrolytic graphite samples. Scanning tunneling microscopy of the surface samples, with different intensities of ion bombardment with zero (a), 10^{11} (b), 10^{12} (c), 10^{13} (e) and 10^{14} (f). (d) First-order Raman spectra evolution measured after each ion bombardment. Figure adapted from CARBON *48* (2010) 1592-1597 28

2.1 Silicon (Si) and gallium arsenide band structure. Figure from *Physics of Semiconductor Devices. Wiley-Interscience*, 2006. 33

2.2 Representation of a particle being transmitted through a square potential. 36

2.3 General scattering process representation. 37

2.4 Longitudinal and transverses voltages for a modulation-doped GaAs film at $T = 1.2K(I = 25.5\mu A)$. The inset figure shows the Hall bridge with width $W = 0.38$ mm and length $L = 1$ mm used to do the measurements. . 40

2.5 Representation of a two terminal devices, with ideal leads connecting the scattering region to reservoirs on the left and right. 42

2.6 The phosphorene nanoribbon along the xy plane (a), and the representation in the zx plane (b). The different hoppings are shown in (a) and the rectangular shaded box gives the unit cell. The coloured dots refer to P atoms belonging to different sublattices (A, B, C and D). 47

2.7 Band structures relation calculated using *DFT-GW* approximation in comparison with four-bands tight-binding model. Figure removed from *Phys. Rev. B* 89, 201408 (2014) 48

2.8 Phosphorene nanoribbon band structure and density of states for armchair (a), and zigzag (b) edges. 51

2.9 The Fermi energy (magenta) as function of magnetic field for density $n_c = 1x10^{16}m^{-2}$. 52

2.10 Lattice structure of (a) AA-stacking BLG and (b) AB-stacking BLG. (c-f) Band structures of BLG nanoribbons for ribbon width of 50 nm and different stacking and edges: (c, d) AA-stack, (e, f) AB-stack, (c, e) zigzag, and (d, f) armchair. 53

3.1 The disorders in phosphorene Hall bar for single vacancies (SVs), double vacancy type I (DV1) and type II (DV2). Only half of the Hall bar is shown. 59

3.2 Schematic representation of the Hall bar. The modified vector field $\vec{A}'(x, y)$ is shown by the arrows. 60
3.3 (a) The phosphorene energy levels for nanoribbons as function of magnetic field. The nanoribbons with width $W_{ac} = 50$ nm and $W_{zz} = 50$ nm correspond to the semi-infinite leads in the Hall bar. The points in the figure indicate the intersection of the Fermi energy (E_F) with the Landau levels. (b) Hall ($R_{13,42}$) and bend ($R_{14,23}$) resistance dependency on the Fermi energy for two different values of the magnetic field. Longitudinal resistance, measured for the (c) armchair terminals ($R_{13,13}$) and for the (d) zigzag terminals ($R_{24,24}$), varying with the Fermi energy for two different values of the magnetic field. 62
3.4 Top row: Hall (black), bend (blue), bottom row: longitudinal resistances for a pristine phosphorene Hall bar for $E_F = 0.345$, 0.35 and 0.363 eV. The vertical dashed lines mark the points where the Fermi energy crosses the armchair Landau levels. 64
3.5 The transmission probability from the leads 1 (a) and 4 (b) to the other leads. The local current density is calculated for specific magnetic fields 8.0, 8.4, 8.7 and 10.0 T, respectively (c), (d), (e) and (f). Density values were normalized. The Fermi energy is $E_F = 0.345$ eV. 65
3.6 DOS of the phosphorene Hall bar for pristine and for three types of disorder with $n_x = 1\%$. 66
3.7 Hall and bend resistances for the phosphorene Hall bar with different densities of vacancies for $B = 10$ T. The bend resistances were multiplied by a defined factor to increase its visibility. The grey vertical lines mark the place where the Fermi energy crosses an armchair transverse mode. 66
3.8 The magnetic-field dependency of the Hall and bend resistances for the phosphorene Hall bar with vacancies at fixed Fermi energy $E_F = 0.35$ eV. . 68
3.9 The magnetic-field dependency of the longitudinal resistance for the phosphorene Hall bar with vacancies at fixed Fermi energy $E_F = 0.35$ eV. . . . 68
3.10 Current density for the phosphorene Hall bar with vacancy defects SV(a), DV1(b), and DV2(c) for $n_x = 0.01\%$ and SV(d), DV1(e) and DV2(f) for $n_x = 0.05\%$. We fixed $E_F = 0.35$ eV and $B = 10$ T. 69

4.1 Schematic illustration of (a) AA- and (b) AB-stacked BLG nanoribbons. Carbon atoms are removed from the top layer (orange). Two ballistic leads (red) are attached to the extremities at the two layers, being used to calculate the conductivity and resistance. (c-f) DoS of the scattering region that defines BLG nanoribbons around the Fermi energy for (left panels) AA- and (right panels) AB-stacked BLG nanoribbons for pristine (blue curve) and defective systems are presented for (c, d) zigzag and (e, f) armchair nanoribbons. Different vacancy densities are taken: 10% (yellow curve), 20% (green curve), and 30% (red curve). 72

4.2 Error bar analysis for the system shown in Fig. 4.1. As we can see the error bar (standard deviation) is considerable small, indicating small error fluctuation. 73

4.3 DoS at $E = 0$ of the scattering region that defines BLG nanoribbons as a function of the vacancies density N for three different ribbon widths (W): (blue) 40 nm, (yellow) 50 nm, and (green) 60 nm, where the ribbon length is defined as $L = 3W$. The total disordered area changes as $A = L \cdot W = 3W^2$. Left (right) panels correspond to AA-(AB-)stacked BLG nanoribbons with (top panels) zigzag and (bottom panels) armchair edges. Each density configuration was averaged by taking twenty samples. Only a small deviation is observed in comparison to the present average curves, that is caused by the random character of the disordered introduction into the BLG system. For a better visualization of the Gaussian-like DoS profile, we omitted here the error bars. The inset in panel (a) shows a linear fit in log-scale for the centered DoS peak ($\equiv$ 21%) for different zigzag AA-stacked nanoribbon widths W. Its slope is 2.012. 75

4.4 (a, b) Enlargements of Fig. 4.3 at low (left) and high (right) vacancy densities for (a) AA-stacked and (b) AB-stacked BLG nanoribbons with ribbon width of 50 nm to emphasize the BLG to MLG transition due to vacancy density increasing. Blue and orange curves are the BLG and MLG DoS values for the pristine cases and the different line types indicate the type of edge orientations. Solid and dashed curves correspond to the pristine DoS values for zigzag and armchair BLG nanoribbons. (c)-(f) Contour plots of the DoS in log scale on the energy-vacancy density plane (E, N) for AA (left panels) and AB (right panels) stacking with nanoribbons formed by (c, d) zigzag and (e, f) armchair edges. 77
4.5 Vacancy clustering analysis for (a) AA- and (b) AB-stacked BLG nanoribbons with ribbon size 150 nm $\times$ 50 nm. Results for single, double, and large clusters of vacancies proportional to the total number of vacancies are shown in blue, yellow, and green. Colored scatter-like plot of the spatial clustering for the systems with vacancies densities at 8%, 20%, 27.5% and 40%, as indicated by the vertical lines in (a), are depicted in the bottom panels (i), (ii), (iii) and (iv), respectively. Each density configuration was averaged by taking five samples. 79
4.6 (a) The ratio I_D/I_G as funciton of the average distance L_D between defects, induced by ion bombardment in mono-layer graphene. (b) shows the definition of the “actived” (green circle) and the “structurally-disordered” (red circle) regions. (b-e) represents a simulation on how those regions start to coaleses as the the number of defects grows. Figure adapted from *Carbon* 48 (2010) 1592-1597. 80
4.7 Resistance as a function of the vacancies density N for (top panels) zigzag and (bottom panels) armchair (left panels) AA-stacked and (right panels) AB-stacked BLG nanoribbons for different Fermi energies. Blue (red) color corresponds to low (high) Fermi energy. Each density configuration was averaged by taking twenty samples. 82

4.8 Current densities for different vacancy concentrations N for zigzag (top panels) AA-stacked and (bottom panels) AB-stacked BLG nanoribbons with ribbon size of 150 nm $\times$ 50 nm. Transport modes with energy $E = 0.1$ eV were injected by the left lead and collected in the right lead. Blue (red, black) color corresponds to low (high, very high) densities. Current densities for bottom and top layers are presented separately. 84

7.1 Finte difference representation of the scattering problem. To discretize the system a grid of equals size $\Delta = x_{i+1} - x_i$. The scattering potential is define inside the region $x_0 < x < x_N$. 99

LIST OF TABLES

2.1 Relevant length scales to quantum conductance. Table adapted from Datta, S. (1995). Electronic Transport in Mesoscopic Systems. 38

4.1 Parameters of the Gaussian-like function fitting, $f \equiv DoS(N) = a\exp\left[-(N-b)^2/c\right]$, for the DoS curves of Fig. 4.3. 78

LIST OF ABBREVIATIONS

2D	Two-dimensional
3D	Three-dimensional
2-DEG	Two-dimensiononal electron gas
AFM	Atomic force microscopy
FET	Field effect transistor
BLG	Bilayer graphene
DOS	Density of states
fcc lattice	Face-center-cubic lattice
FLG	Few-layer graphene
(G)QDs	(Graphene) quantum dots
LL(s)	Landau Level(s)
ML, MLG	Monolayer, monolayer graphene
BLG	Bilayer graphene
TB	Tight-binding (model)
SV, SVA(B)	Single vacancies, single vacancies considering sublattice A(B)
DV	Double vacancies
AC	Armchair edge orientation
ZZ	Zigzag edge orientation

LIST OF NOMENCLATURES

Symbol	Description
v_f	Fermi velocity
τ, γ_i	Hopping parameters
$\Psi_A(\Psi_B)$	The probability of finding the electron on sublattice A and B
e	Elementary electron charge
$\vec{A}$	Vector potential
$\vec{B}$	Magnetic field
l_B	Magnetic length
ϕ_{ij}	Peierls phase
$\vec{p}$	Momentum vector
T	Kinetic operator
V	Potential operator
$\vec{a}_i$	Real lattice vector i
$\vec{b}_i$	Reciprocal lattice vector i
H	Hamiltonian
$\mathbf{a}_i^\dagger$	Creation operator of electrons on the site i of the subllatice A
$\mathbf{a}_i$	Annihilation operator of electrons on the site i of the subllatice A
$\mathbf{b}_i^\dagger$	Creation operator of electrons on the site i of the subllatice B
$\mathbf{b}_i$	Annihilation operator of electrons on the site i of the subllatice B
I_D	Intensity of disorder-induced band
I_G	Intensity of ground-state band
H_{AB}	Hamiltonian for the AB-stacking bilayer graphene
H_{AA}	Hamiltonian for the AA-stacking bilayer graphene
H_M	Hamiltonian for the intra-hoppings and onsite energies for bilayer graphene
N	Probability of creating a vacancy
N_{vac}	Percentage of vacancies

$g(\vec{k})$	Structure factor of the crystal
$Y_l^m(\theta, \phi)$	Spherical harmonics
$J_m(\kappa\rho)$	The Bessel function of the first kind
$\widetilde{M}(A_{\pm}, B, \widetilde{\rho})$	The regularized confluent hypergeometric function
$\mathcal{H}_n(x)$	Hermite polynomials
h, $\hbar$	Plank's constant and Plank's constant divide by 2π
K	Dirac cone K
K'	Dirac cone K'
ϵ_i	Self-energy on site i
d	Width of initial gaussian wave packet
W	Scattering region width
L	Scattering region length
T_{ij}	The transmission probability of a transport mode
$R_{mn,kl}$	Resistance in a four-terminals Hall bar
$\vec{\sigma}_i$	Pauli matrix i
a	Lattice parameter
E	Energy
G_{sd}	Differential conductance between a terminals
S_{nm}	Scattering matrix

Contents

1 Introduction **22**

1.1 2D nanomaterials 22

1.1.1 Two-dimensional electron gas (2-DEG) 22

1.1.2 Graphene 23

1.1.3 Black-phosphorus sheet 25

1.1.4 Bilayer graphene 26

1.2 Defects in nanomaterials 26

1.3 Outline and thesis objectives 29

2 Electronic transport in 2-dimensional materials **31**

2.1 Theoretical description of crystal structure 31

2.2 Quantum transport 34

2.2.1 Transmission in quantum system 34

2.2.2 Scattering matrices 37

2.2.3 Characteristic lengths 38

2.2.4 Hall measurements 40

2.3 Landauer-Büttiker formalism 42

2.4 Tight-binding model 44

2.4.1 Defects in tight-binding systems 46

2.4.2 Tight-binding in second quantization 46

2.4.3 Phosphorene tight-binding model 47

2.4.4 Tight-binding model for BLG 52

2.5 Software and numerical methods 55

3 HALL AND BEND RESISTANCE OF A PHOSPHORENE HALL BAR **58**

3.1 Introduction 58

3.2 System and methods 58

3.2.1 Hall bar 59

3.3 Pristine phosphorene Hall bar 61

3.4 Effect of vacancies 65

3.5 Conclusions 70

4 VACANCY CLUSTERING EFFECT ON THE ELECTRONIC AND TRANSPORT PROPERTIES OF BILAYER GRAPHENE NANORIBBONS **71**

4.1 Introduction 71

4.1.1 Defects in BLG 71

4.2 Zero-modes density 75

4.3 Electronic transport 81

4.4 Conclusions 85

5 SUMMARY AND PERSPECTIVES **87**

6 BIBLIOGRAPHY **89**

APPENDIX A - WAVE FUNCTION MATCHING THECHNIQUE FOR QUAN-TUM TRANSPORT CALCULATIONS **99**

APPENDIX B - PUBLISHED ARTICLES **103**

APPENDIX C - ONGOING ARTICLES **104**

The 1965 Gordon E. Moore(MOORE, 2006) paper about the future of silicon based integrated electronics introduced what it came to be know as *Moores's law*. The Moore's law hypotheses that the number of transistors in a integrated circuit doubles every year (see Fig. 1.1). Over the years the continuous development of faster and better computers, with greater processing capacities, creates a demand for improved electronics technologies(MOORE, 2006; ITRS,). Several improvements have been made to boost the perfomance of conventional devices at nanometric scale(FIORI *et al.*, 2014), but it was showed that reducing past 7nm channel size does not offers much advantages(KASIOREK, 2021). Another problem that arises at nano scale is the emergency of quantum effects, which dictates the mechanics at atomic levels. Under these circumstances, there is a increasing demand for new materials and transistors geometries to continue the development of newer technologies(ITRS,).

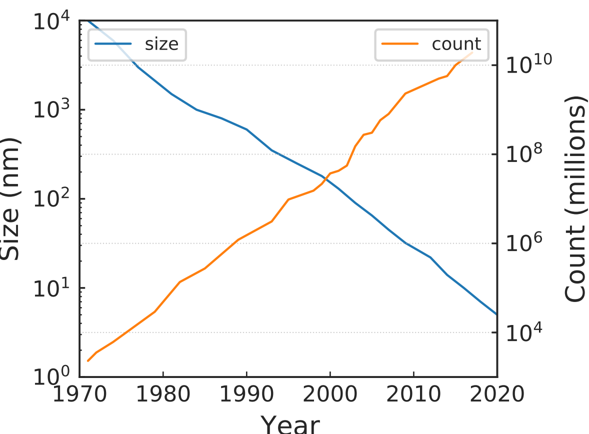

Figure 1.1: Relation between the number of transistors in a processor against the device size throughout the years. Data retrived from: <https://en.wikipedia.org/wiki/Transistor_count> and <https://ourworldindata.org/grapher/transistors-per-microprocessor>.

1.1 2D nanomaterials

1.1.1 Two-dimensional electron gas (2-DEG)

Most of the work around low dimensional system has largely been based on GaAs-AlGaAs heterojunctions. In this system a thin two-dimensional conducting layer is formed at the interface between GaAs and AlGaAs (see Fig. 1.2-(a)), which is formed considering the conduction and valence band line-up in the z-direction when the layers are put in contact. The energy gap in AlGaAs is wider than in GaAs layer, and consequently electrons spill over from the n-AlGaAs leaving behind positively charged donors. In Fig. 1.2 we can see that the space charge gives rise to an electrostatic potential that causes

the bands to bend. The thin conducting layer (referred to as two dimensional electron gas (2-DEG)) is formed near the interface GaAs-AlGaAs.

The 2-DEG as practical application as field effect transistor(DATTA, 1995). It has carrier concentration typically ranging from $2 \times 10^{11}/cm^2$ to $2 \times 10^{12}/cm^2$ and can be depleted by applying a negative voltage to a metallic gate deposited on the surface.

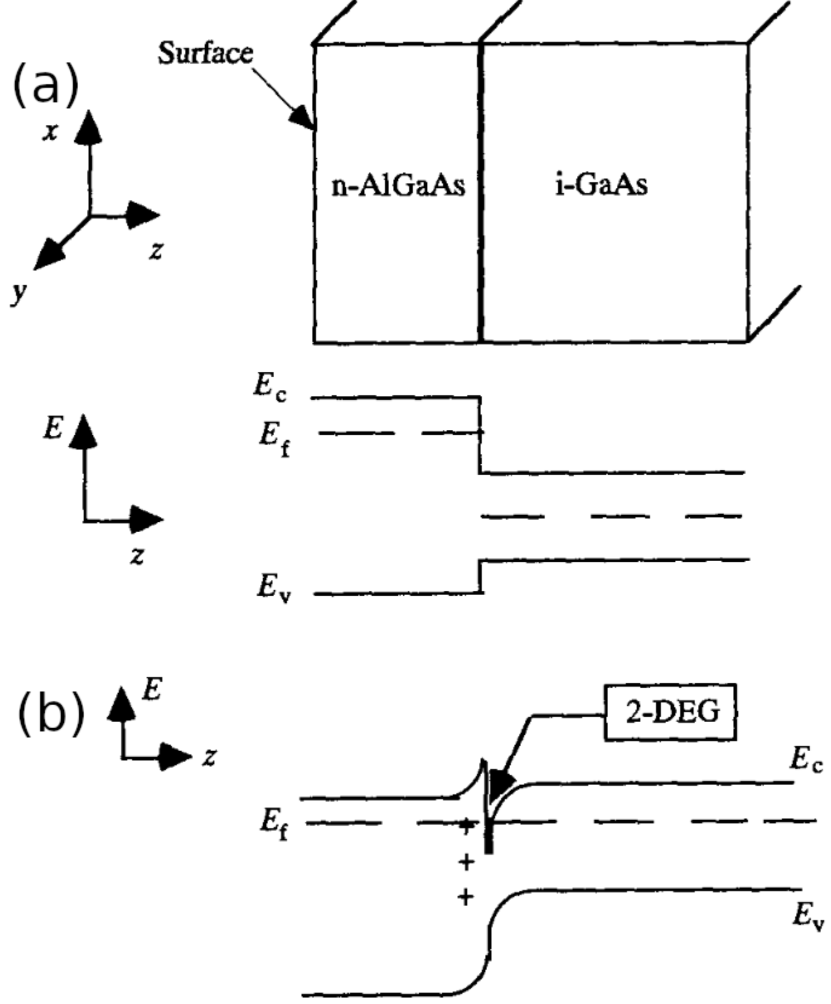

Figure 1.2: (a) The schematic of a n-type AlGaAs and intrisic GaAs heterojunction before and (b) after the charge transfer. Figure adapt from *Datta, S.* (1995). *Electronic Transport in Mesoscopic Systems.*

1.1.2 Graphene

The two-dimensional (2D) class of materials have started to draw a lot of attention due to their nano scale thickness(AKINWANDE *et al.*, 2019) and their unique physical and chemical characteristics. 2D materials has been prove to be an alternative as the new class electronic and optoelectronic devices, such as photodetectors, light-emitting

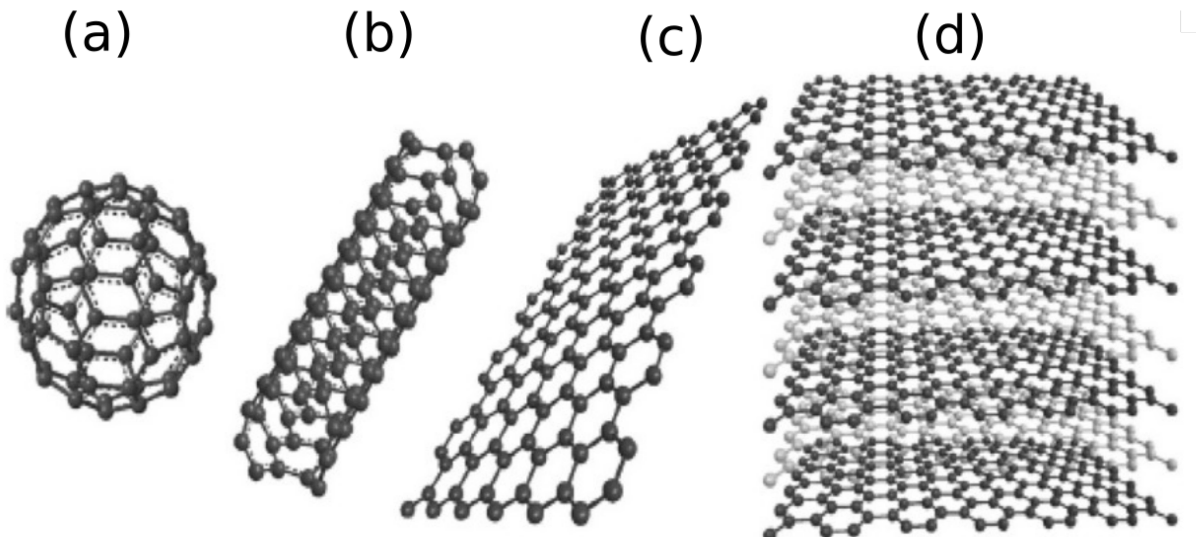

Figure 1.3: Different carbon allotrope: (a) fullerenes, (b) carbon nanotubes, (c) graphene and (d) graphite. Figure modified from *Sensors and Actuators B* 173 (2012) 1-21.

diodes (LEDs), field effect transistors (FETs) and solar cells. One of the most studied class 2D materials are the layered transition metal dichalcogenide (TMDC) compounds, with in general as a chemical formula MX_2 , where M is a transition metal (e.g., Mo, W, Re, or Ta) and X is a chalcogen (e.g., S, Se,or Te)(FIORI *et al.*, 2014; SANGWAN; HERSAM, 2018). But, it was with the experimental discovery of the graphite monolayer (graphene)(NOVOSELOV *et al.*, 2004) that 2D layered materials interest "explode" in the scientifical society.

Graphene consists of a single layer of graphite carbon allotrope(NOVOSELOV *et al.*, 2004; BASU; BHATTACHARYYA, 2012) (see Fig. 1.3-c). The carbon atoms are arranged in a honeycomb lattice and possess sp^2 hybridization, where each of them being connected by a σ-bond to other three carbon atoms forming a trigonal planar structure by a σ-bond(NETO *et al.*, 2009b). An p-orbital, perpendicular to the crystal plane, can connect to others carbon atoms leading a formation of a delocalized π-band(NETO *et al.*, 2009b). Due to this arrangement, two energy bands intersects at the K and K' points in the Brillouin zone. The electron energy $E(\boldsymbol{k})$ close to these crossing points has a linear dependency with the wave vector $\boldsymbol{k}$, forming what is called Dirac cones and exhibiting a *gapless* spectrum at low energies. The electrons at these regions behaves like a zero-mass relativistic particle and its motion can be describe by the *Dirac's* equation. As result, many interesting phenomena appears in graphene, such as an anomalous integer quantum Hall effect at room temperature(NOVOSELOV *et al.*, 2006), high charge carrier mobility

($< 10^5 cmV^{-1}s^{-1}$), insensitivity to external electrostatic potentials (Klein paradox(**??**)), and the peculiar phenomena known as *zitterbewegung*(ZAWADZKI; RUSIN, 2010).

1.1.3 Black-phosphorus sheet

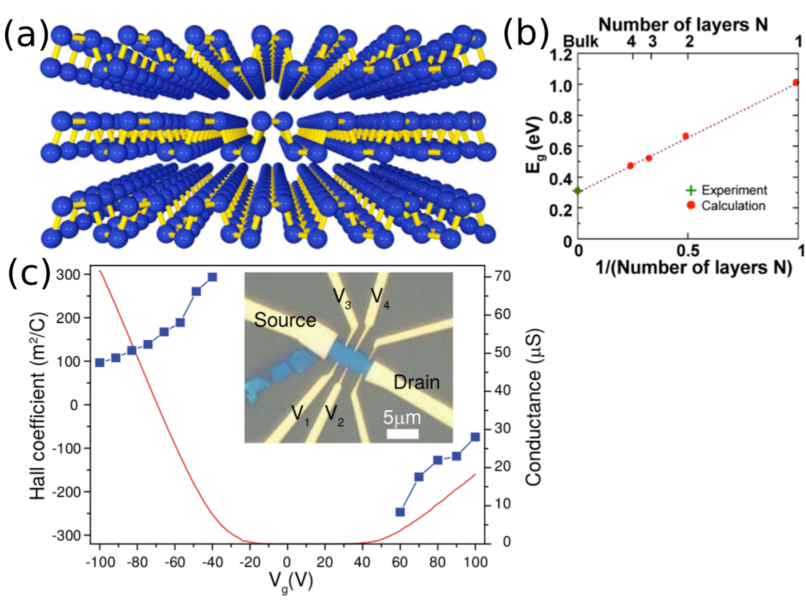

Figure 1.4: (a) Perspective side view of few-layer phosphorene. (b) DFT-HSE06 results for the dependence of the energy gap in few-layer phosphorene on the number of layers. (c) Hall coefficient (blue curve) and conductance (red curve) as a function of gate voltage collected from a 8-nm-thick sample on Si substrate with 285 nm SiO_2. Images from *ACS Nano* 2014, 8, 4, 4033–4041 (a-b) and *Nature Nanotechnology* volume **9**, pages 372–377 (2014) (c).

Black phosphorus (BP), which is the most stable phosphorus crystal at room temperature and pressure, has recently drawn a lot of attention due to its unique electronic properties (CASTELLANOS-GOMEZ *et al.*, 2014; QIAO *et al.*, 2014). BP is a layered material where each individual atomic layer is held together by van der Waals interactions (CARVALHO *et al.*, 2016; CHEN *et al.*, 2017; AKHTAR *et al.*, 2017). This allows the construction of devices with an arbitrary number of phosphorene layers(AKHTAR *et al.*, 2017; DHANABALAN *et al.*, 2017). Figure 1.4-(a) shows the crystal structure of few-layer black phosphorus, each phosphorus atom in a monolayer phosphorene is bounded via sp^3 hybridization forming a puckered lattice structure. Unlike other 2D layered materials, black phosphorus shows interesting properties such as high carrier mobility (AKHTAR *et al.*, 2017; QIAO *et al.*, 2014), anisotropic optical-conductance (ZHOU *et al.*, 2014; ÇAKıR *et al.*, 2015), and a band gap dependence on the number of layers (LIU *et al.*, 2014; ÇAKıR *et al.*, 2015), ranging from 0.3 eV for bulk and 1.5 eV for ML phosphorene

(see Fig.1.4-(b-c)). This material also has a good on/off switch, which makes it a good candidate for field effect transistor (FET) devices (LI *et al.*, 2014b; LI *et al.*, 2014a).

1.1.4 Bilayer graphene

Bilayer graphene(NETO *et al.*, 2009a; MCCANN; KOSHINO, 2013; ROZHKOV *et al.*, 2016) (BLG), two coupled monolayers of graphite, has attracted along the last two decades a lot of attention in the field of low-dimensional science and nanotechnology, mostly due to the fact that it shares many of the advantages of graphene's unique properties, such as high electrical mobility (MOROZOV *et al.*, 2008), as well others not so desired for standard logic applications, as for example, a minimum conductivity at the neutrality point of the order of the conductance quantum (NOVOSELOV *et al.*, 2006; CASTRO *et al.*, 2008). But, in contrast to graphene, BLG has an electric field tunable band gap(ALLEN *et al.*, 2012; MCCANN; KOSHINO, 2013; ZHANG *et al.*, 2009, 2009; MAK *et al.*, 2009; MCCANN, 2006), which can be induced by electrostatic gating or chemical doping (see Fig. 1.5-(d)), being of paramount importance for producing high on-off current ratios(XIA *et al.*, 2010). This additional electronic feature makes BLG a promising material for applications in optoelectronics and sensors, as for instance to be used to design the next-generation of field effect transistors (OOSTINGA *et al.*, 2008; CHEN *et al.*, 2015; SZAFRANEK *et al.*, 2011; CHELI *et al.*, 2009; OUYANG *et al.*, 2008) and electrostatic defined BLG quantum dots based devices (GE *et al.*, 2020; PEREIRA *et al.*, 2007). Another interesting property is the possibility to rotate the layers in relation to each other, as seen in Fig 1.5-(b), which is responsible to the appearance of new properties in BLG(CAO *et al.*, 2018).

1.2 Defects in nanomaterials

Structural defects in a crystallographic lattice are defined as any region where the microscopic arrangement of ions differ from the perfect crystal structure(ASHCROFT, 1976), by means of distortion, reconstruction or displacement(NASCIMENTO *et al.*, 2017; BANDEIRA *et al.*, 2020). They can be characterized in different manners, such as in-plane defects that are symmetry-breaking and can include point defects, as for example vacancies(KOTAKOSKI *et al.*, 2011; LEE *et al.*, 2005; PALACIOS *et al.*, 2008; KISHIMOTO; OKADA, 2016; HAHN; KANG, 1999; XU *et al.*, 2009; EL-BARBARY *et al.*,

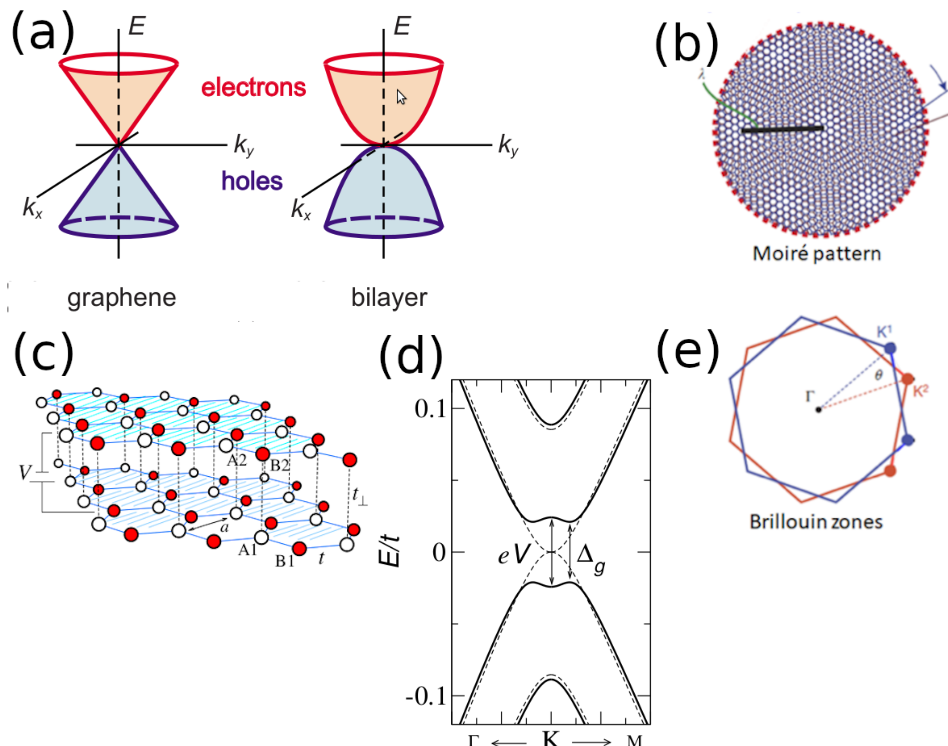

Figure 1.5: (a) Comparison between graphene and BLG band dispersion at Dirac point. Figure adept from Am. J. Phys, **77** (7), July 2009. (c) Schematics for biased AB-stack BLG and (d) band structure near the Dirac points for V = 0.15 eV (solid line) and V = 0 eV (dashed line) and. Figure adapted from Phys. Rev. Lett. **99**, 216802. (b) Moiré pattern as seen in twisted BLG and the mini Brillouin zone, which is the (e) reciprocal Moiré superlattice. Figure adapted from Nature volume **556**, pages 80–84 (2018)

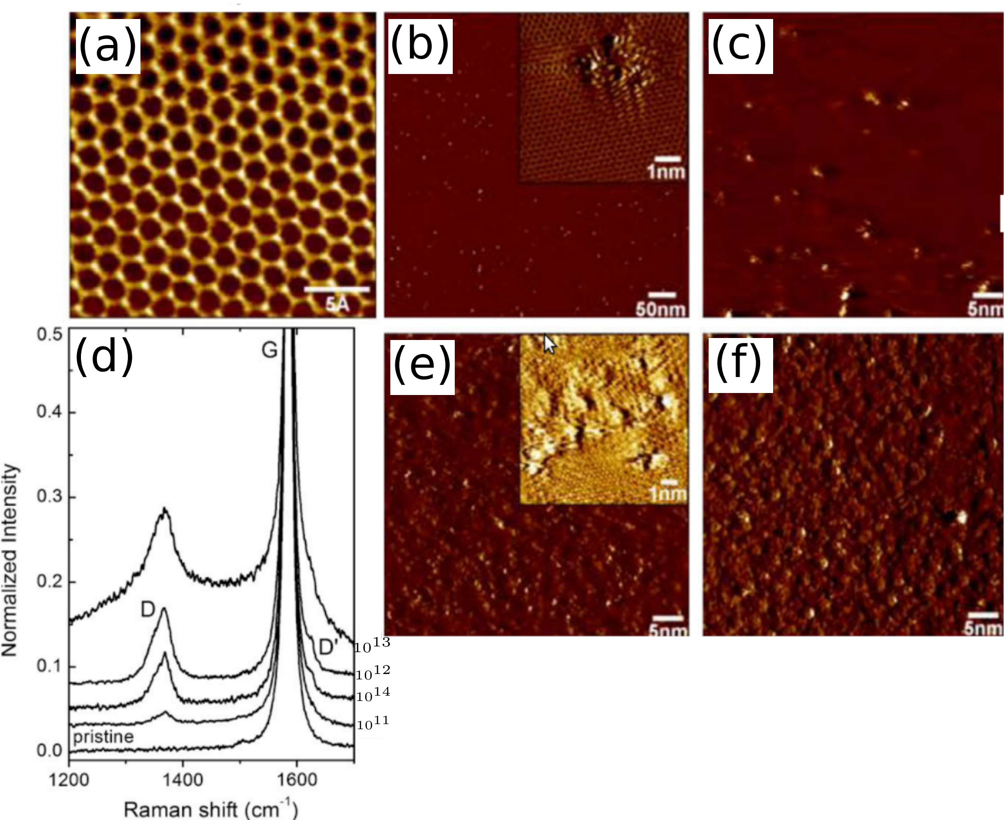

Figure 1.6: Defects in highly oriented pyrolytic graphite samples. Scanning tunneling microscopy of the surface samples, with different intensities of ion bombardment with zero (a), 10^{11} (b), 10^{12} (c), 10^{13} (e) and 10^{14} (f). (d) First-order Raman spectra evolution measured after each ion bombardment. Figure adapted from CARBON *48* (2010) 1592-1597

2003a; OVDAT *et al.*, 2020), substitutional impurities, interstitial impurities (HAHN; KANG, 1999), and interplanar defects, as for instance stacking faults within interlayer stackings(BANHART *et al.*, 2011; TELLING *et al.*, 2003; VUONG *et al.*, 2017).

Atomic vacancies occurs whenever a site in the Bravais lattice is missing, where it would be occupied otherwise. Since the presence of disorder in a system increases its entropy, even in thermal equilibrium there is always a certain number of disorder(C., 1953). Considering this, the number n of vacant sites can be found by the Boltzmann factor(C., 1953; ASHCROFT, 1976)

$$\frac{n}{N-n} = e^{(\frac{-E_V}{k_B T})}, \tag{1.1}$$

where N represents the total number of atoms, E_V is the energy required to remove a atom from a crystal lattice site, k_B is the Boltzmann constant and T is the temperature.

One of the main challenges in order to make 2D based devices reliable for large scale production, is the control and understanding of defects in 2D materials. Although being unwanted, the presence of defects and impurities in experimental realizations of two-dimensional materials are, in general, almost impossible to be avoided and they alter the electronic and transport properties of these systems,(ARAUJO *et al.*, 2012) by reducing the electronic mobility(ADAM *et al.*, 2007; BANHART *et al.*, 2011) and changing its electronic band structure(FILHO *et al.*, 2007).

Figure 1.6 shows the scanning tunneling microscopy (STM) image of the bulk highly oriented pyrolytic graphite (HOPG) before and after the Ar^+ ion bombardment. The effects of the bombardments induced defects is shown in the Fig. 1.6-(d), where the Raman spectra shows the evolution of the spectrum related to different ion doses(LUCCHESE *et al.*, 2010).

1.3 Outline and thesis objectives

The unavoidable presence of defects in 2D materials can significantly affects the electronic properties of the systems, which depending on the circumstances, is highly undesirable for applications. In order to expand the theoretical knowledge on how defects affects 2D materials, this thesis has as main objective study the effects of structural disorder (i.e. point defects) in 2D materials, specifically the bilayer graphene and the phosphorene. To

do so, the electronic and transport properties of multi-terminals defective materials in the presence of external fields. This theses is organized as follows.

Most of the theoretical background and models description will be presented in Chapter 2. First a general discussion about the electronic properties of crystal is presented. Second, the tight-binding approximation, which will be use to describe the materials, is introduced by using a general model, followed by the tight-binding description of phospherene and BLG. Next the quantum transport and the scattering theory, based on the wave function formulation, are discussed. This formulation, combined with the Landauer-Büttiker formalism will provided the numerical tools to study the quantum transport in the 2D materials.

In Chapter 3, different types of vacancies, based on the sublattice symmetry, are analysed by studying the magnetotransport in multiterminal phosphorene mono layer (ML). This will be done by studying the Hall and bend resistance of a four-terminal Hall bar system in the presence of a perpendicular magnetic field. In order to understand the effects of the vacancies, we will first present the results for a pristine (defect free) system, where a discussion of the presence of both armchair and zigzag terminals and the magnetic field is made. Following the effect of vacancies on the DOS and the transport properties are investigated.

In Chapter 4, the transition from a BLG to a MLG nanoribbon is studied by analysing the presence of zero modes in the density of states due to point defects. To mimic the lack of control in the position of vacancies, one focuses here on the effects of randomly distributed vacancies in the electronic structure of BLG nanoribbons with armchair and zigzag orientations, which allows the formation of vacancy clustering. A "coalescence" between the defects will be studied by the clustering of neighbours vacancies. Both AA and AB BLG stacks will be investigated for nanoribbons with different sizes and edges. Our electronic and transport results for the energy spectrum, density of states (DOS), resistance, and current density for different vacancy concentration are obtained by using the first nearest neighbour hoppings tight-binding (TB) model, and the latter by using the Landauer–Büttiker formalism.

In Chapter 5 a summary and some perspectives are presented.

2 ELECTRONIC TRANSPORT IN 2-DIMENSIONAL MATERIALS

In this chapter we discuss the numerical methods and physical concepts used in this thesis. First we will discuss about basics properties of crystal structure. Then, in order to study the electronic transport properties of materials, a brief description of quantum transport is presented, followed by the Landauer-Büttiker formalism for multi-terminals electronic transport. Next, a general tigh-binding model is presented to introduce the formalism used to describe the materials in study. The tight-binding models for the phosphorene and BLG are then presented.

2.1 Theoretical description of crystal structure

Crystals are characterized by having a well structured periodic arrangement of atoms, where the smallest assembly of atoms, called *primitive cell*, can be repeated to form the entire crystal. The primitive cell is characterized by the *lattice constants*, which defines its dimensions, and the *basis vectors* $\boldsymbol{a}$, $\boldsymbol{b}$ and $\boldsymbol{c}$. As mentioned a crystal is formed by repetition of the primitive cell, which is archived by translating these bases vectors. So, we can define the set direct lattice sites as,

$$\boldsymbol{R} = m\boldsymbol{a} + n\boldsymbol{b} + p\boldsymbol{c}, \tag{2.1}$$

m, n and p are integers.

The orientation and properties of the surface crystal planes are important features to be understood since semiconductor devices are built on or near the semiconductor surfaces. A simple way to define the planes in crystal are the Miller(C., 1953; SZE, 2006) indices. They are determined by finding the intercepts of the plane with the three basis axes in terms of the lattice constants, and them taking the reciprocal of these numbers and reducing them to the smallest three integers with the same ratio. For a set of parallel planes, they are represent by hkl. They provide a useful way to represent crystal's surface orientation, which is important to understand the electronic properties of the crystal but also during the process of fabrication(PIERRET, 1989)

The behavior of electron's wavefunction ψ in a material can be describe by the Schrödinger equation,

$$\frac{-\hbar^2}{2m}\nabla^2\psi(\boldsymbol{k},\boldsymbol{r}) + V(\boldsymbol{r})\psi(\boldsymbol{k},\boldsymbol{r}) = E\psi(\boldsymbol{k},\boldsymbol{r}). \tag{2.2}$$

Considering that the electron potential $V(\boldsymbol{r})$ in a crystal structure is periodic in the direct lattice space, the wavefunction $\psi(\boldsymbol{k},\boldsymbol{r})$ as form of a *Bloch* function(SZE, 2006; SAKURAI, 1994)

$$\psi(\boldsymbol{k},\boldsymbol{r}) = e^{i\boldsymbol{k}\cdot\boldsymbol{r}}u(\boldsymbol{k},\boldsymbol{r}), \tag{2.3}$$

where $u_m(\boldsymbol{k},\boldsymbol{r})$ are periodic with R, leading to,

$$\begin{aligned} \psi(\boldsymbol{k},\boldsymbol{r}+\boldsymbol{R}) &= e^{i\boldsymbol{k}\cdot(\boldsymbol{r}+\boldsymbol{R})}u(\boldsymbol{k},\boldsymbol{r}+\boldsymbol{R}), \\ &= e^{i\boldsymbol{k}\cdot\boldsymbol{r}}e^{i\boldsymbol{k}\cdot\boldsymbol{R}}u(\boldsymbol{k},\boldsymbol{r}), \\ &= e^{i\boldsymbol{k}\cdot\boldsymbol{r}}u(\boldsymbol{k},\boldsymbol{r}). \end{aligned} \tag{2.4}$$

$\boldsymbol{k}\cdot\boldsymbol{R}$ being multiple to 2π.

By solving Eq. 2.2 one can obtain the electron's band structure, that is, the energy-momentum relation. The energy-momentum relation $E-k$ is periodic in the reciprocal lattice, that is, $E(\boldsymbol{k}) = E(\boldsymbol{k}+\boldsymbol{G})$, where $\boldsymbol{G} = h\boldsymbol{a}^* + k\boldsymbol{b}^* + l\boldsymbol{c}^*$ is the reciprocal lattice vector[1]. Figure 2.1 shows the band structure for the silicon and gallium arsenide materials. From Fig. 2.1 we can see important features from semiconductor devices, such as the energy gap (E_g) and the allowed energy states. The energies above and below the energy gap are called *conduction* (E_C) and *valence* (E_V) band. The energy gap of GaAs is called *direct* because the minimal energy state in the conduction band has the same k-vector of the maximal energy state in the valence band.

The $E(k)$ can be approximated by a quadratic equation, near the band edges (see Fig. 2.1),

$$E(k) = \frac{\hbar^2 k^2}{2m^*}, \tag{2.5}$$

where m^* is the associated electron effective mass, which can be in general tensorial form m^*_{ij},

$$\frac{1}{m^*_{ij}} \equiv \frac{1}{\hbar^2}\frac{\partial^2}{\partial k_i \partial k_j}E(k). \tag{2.6}$$

From the $E-k$ relation one can also calculate the group velocity of the carriers in

[1]The reciprocal lattice basis vectors are defined as $\boldsymbol{a}^* \equiv 2\pi\frac{\boldsymbol{b}\times\boldsymbol{c}}{\boldsymbol{a}\cdot\boldsymbol{b}\times\boldsymbol{c}}$, $\boldsymbol{b}^* \equiv 2\pi\frac{\boldsymbol{c}\times\boldsymbol{a}}{\boldsymbol{a}\cdot\boldsymbol{b}\times\boldsymbol{c}}$ and $\boldsymbol{c}^* \equiv 2\pi\frac{\boldsymbol{a}\times\boldsymbol{b}}{\boldsymbol{a}\cdot\boldsymbol{b}\times\boldsymbol{c}}$.

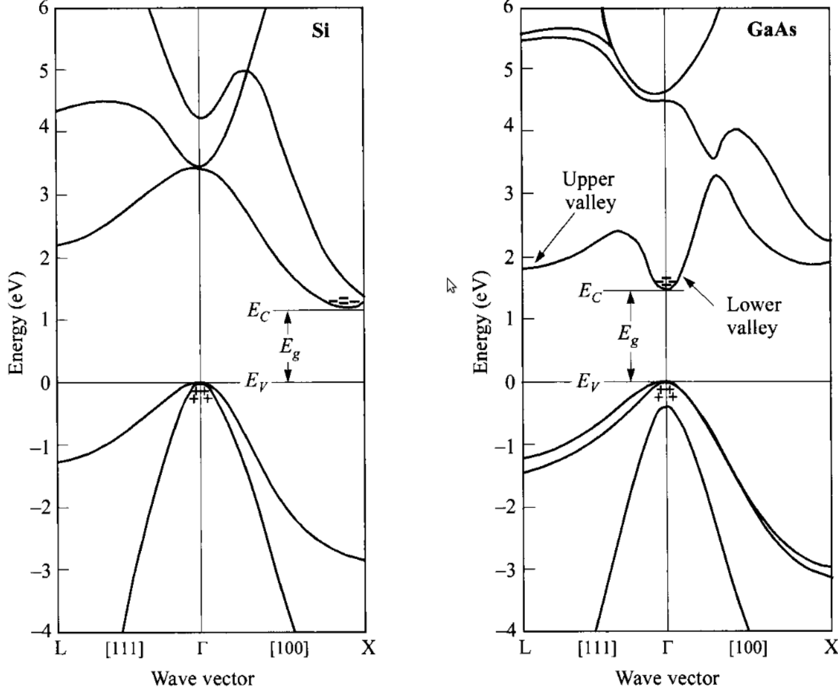

Figure 2.1: Silicon (Si) and gallium arsenide band structure. Figure from *Physics of Semiconductor Devices. Wiley-Interscience*, 2006.

motion,

$$v_g = \frac{1}{\hbar}\frac{d}{dk}E \tag{2.7}$$

with momentum $p = \hbar k$. One can also find number of electrons (occupied conduction-band levels) by integrating the total number of states, i.e., density of states (DOS), over the conduction band,

$$n_e = \int_{E_C}^{\infty} D(E)F(E)dE. \tag{2.8}$$

The *occupancy* is represented by the *Fermi-Dirac* distribution function,

$$F(E) = \frac{1}{1 + e^{(E-E_F)/kT}}. \tag{2.9}$$

E_F is the Fermi energy level. The DOS relate the number energy states levels in a volume of the k space,

$$D(E) = \frac{1}{V}\sum_{i=1}^{N} \delta(E - E(\boldsymbol{k})_i). \tag{2.10}$$

The volume V is calculated for the first Brillouin zone.

In some cases it is interesting to look how electron's wavefunction is arranged in the

system. The local density of states (LDOS) spatial dependency of the DOS, and it is described as

$$L_D(E,\boldsymbol{r}) = \sum_{i=1}^{N} |\psi(\boldsymbol{k}_i,\boldsymbol{r})|^2 \delta(E - E(\boldsymbol{k})_i). \tag{2.11}$$

The LDOS is also useful to analyse and interpret the scanning tunneling microscope(PASSONI *et al.*, 2009).

2.2 Quantum transport

Now we are going to introduce concepts of quantum transport in one-dimensional. Due to its simplicity, one-dimensional systems allows to understand the physics and mathematical concepts of quantum transport.

2.2.1 Transmission in quantum system

First, let's consider the one dimensional time-dependent version of the Schrödinger equation 2.2,

$$-\frac{\hbar^2}{2m}\frac{\partial^2}{\partial x^2}\Psi(x,t) + V(x)\Psi(x,t) = i\hbar\frac{\partial}{\partial t}\Psi(x,t). \tag{2.12}$$

The wavefunction $\Psi(x,t)$ is interpreted by its square modulus $|\Psi(x,t)|^2$ as the probability density of a measurement of particle's position. Considering that the particle has to be found *somewhere* in space(FITZPATRICK, 2010; GRIFFTHS, 2004), the probability,

$$P_{-\infty,\infty}(t) = \int_{-\infty}^{\infty} |\Psi(x,t)|^2 dx. \tag{2.13}$$

must be equals to 1. Which leads to the normalization condition $\int_{-\infty}^{\infty} |\Psi(x,t)|^2 dx = 1$.

An important property from the probability interpretation is that a initially normalized wavefunction stays normalized as it evolves in time(FITZPATRICK, 2010), which means $\frac{d}{dt}\int_{-\infty}^{\infty} |\Psi(x,t)|^2 dx = 0$. This can be prove as follows,

$$\frac{d}{dt}\int_{-\infty}^{\infty} |\Psi(x,t)|^2 dx = \int_{-\infty}^{\infty} \left(\frac{\partial}{\partial t}\Psi^*(x,t)\Psi(x,t) + \Psi^*(x,t)\frac{\partial}{\partial t}\Psi^*(x,t)\right) dx. \tag{2.14}$$

By multiplying the Eq. 2.12 by $\Psi(x,t)^*/i\hbar$,

$$\frac{i\hbar}{2m}\Psi^*(x,t)\frac{\partial^2}{\partial x^2}\Psi(x,t) - \frac{i}{\hbar}V(x)|\Psi(x,t)|^2 = \Psi(x,t)^*\frac{\partial}{\partial t}\Psi(x,t). \tag{2.15}$$

And the complex conjugate of Eq. 2.15 is given by,

$$-\frac{i\hbar}{2m}\Psi(x,t)\frac{\partial^2}{\partial x^2}\Psi^*(x,t) + \frac{i}{\hbar}V(x)|\Psi(x,t)|^2 = \Psi(x,t)\frac{\partial}{\partial t}\Psi^*(x,t). \tag{2.16}$$

Summing the Eqs. 2.15 and 2.16,

$$\begin{aligned}\frac{i\hbar}{2m}\left(\Psi^*(x,t)\frac{\partial^2}{\partial x^2}\Psi(x,t) - \Psi(x,t)\frac{\partial^2}{\partial x^2}\Psi^*(x,t)\right) &= \frac{i\hbar}{2m}\frac{\partial}{\partial x}\Bigg(\Psi^*(x,t)\frac{\partial}{\partial x}\Psi(x,t) \\ &\quad - \Psi(x,t)\frac{\partial}{\partial x}\Psi(x,t)^*\Bigg) \\ &= \Psi^*(x,t)\frac{\partial}{\partial t}\Psi(x,t) + \Psi(x,t)\frac{\partial}{\partial t}\Psi^*(x,t).\end{aligned} \tag{2.17}$$

So, Eq. 2.14 becomes,

$$\frac{d}{dt}\int_{-\infty}^{\infty}|\Psi(x,t)|^2 dx = \frac{i\hbar}{2m}\frac{\partial}{\partial x}\left(\Psi^*(x,t)\frac{\partial}{\partial x}\Psi(x,t) - \Psi(x,t)\frac{\partial}{\partial x}\Psi^*(x,t)\right) = 0. \tag{2.18}$$

Due to $|\Psi(x,t)|^2 \to 0$ as $|x| \to \infty$.

If instead consider the whole space $(-\infty, \infty)$ we take only a range $[a, b]$, one can define the *probability conservation equation*,

$$\frac{d}{dt}P_{a,b}(t) + j(b,t) - j(a,t) = 0, \tag{2.19}$$

where,

$$j(x,t) = \frac{i\hbar}{2m}\left(\Psi(x,t)\frac{\partial}{\partial x}\Psi^*(x,t) - \frac{\partial}{\partial x}\Psi(x,t)\Psi^*(x,t)\right), \tag{2.20}$$

is the *probability current.* If we consider a particle with charge q, then the expected charge found in a region $[a, b]$ at time time t is $Q_{a,b}(t) = qP_{a,b}(t)$, which leads to,

$$\frac{d(t)}{dt}Q_{a,b} = I(a,t) - I(b,t). \tag{2.21}$$

$I(x,t) = qj(x,t)$ is the *electrical current.*

Transmission through a barrier

Let's consider that the wave function is time independent. So the solution of Eq. 2.12 has the form(GRIFFTHS, 2004)

$$\Psi(x,t) = \psi(x)e^{-\frac{i}{\hbar}Et}. \tag{2.22}$$

Then, one can find that,

$$\frac{d}{dt}P_{a,b}(t) = 0, \tag{2.23}$$

and,

$$j(x,t) = constant. \tag{2.24}$$

Using Eq. 2.22 in Eq. 2.12,

$$\frac{d^2}{dx}\psi(x) = k\psi(x), \tag{2.25}$$

$k = \frac{\sqrt{2m(V(x)-E)}}{\hbar^2}$. Equation 2.25 is the *time independent* Schrödinger equation.

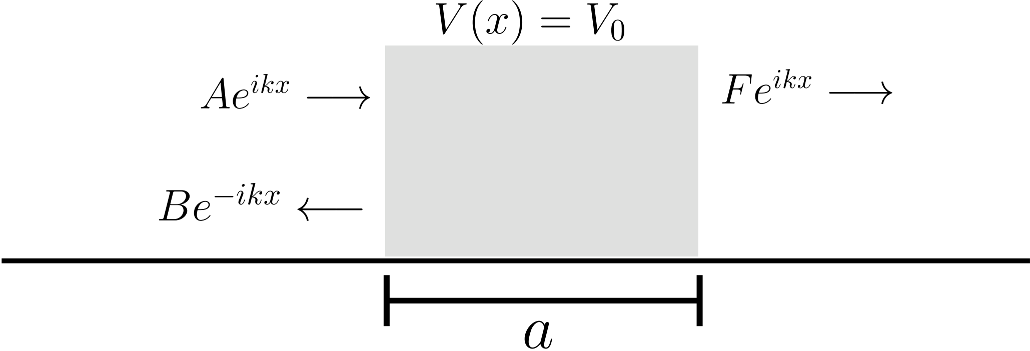

Figure 2.2: Representation of a particle being transmitted through a square potential.

Now, let's consider a particle being transmitted through square potential barrier,

$$V(x) = \begin{cases} V_0, & 0 \leq x \leq a \\ 0, & \text{otherwise} \end{cases}, \tag{2.26}$$

for $V_0 > 0$ and a being the square potential size. The solution on the left of the barrier $(x < 0)$

$$\psi(x) = Ae^{ikx} + Be^{-ikx}, \tag{2.27}$$

consist of two plane plane waves: one traveling to the right side with amplitude A and another traveling to the left side with amplitude B. The first plane wave is interpreted as

an *incident wave* and the second is the *reflected wave* by the square potential. One can find the associated reflection probability $|R|$ by considering the probability current 2.20,

$$j = \frac{\hbar k}{m}|A|^2 - \frac{\hbar k}{m}|B|^2. \tag{2.28}$$

which we can interpreted as the difference between the incident and reflected currents $j = j_I - j_R$. So, the reflection coefficient R is defined by the ratio between the reflected and incident currents.

$$R = \frac{j_R}{j_I} = \frac{|B|^2}{|A|^2}. \tag{2.29}$$

The solution on the right side of the barrier consist of one plane wave with amplitude F traveling to the right side. We can interpret this as the *transmitted wave* with the *transmission* probability given by the ratio between the transmitted and incident currents,

$$T = \frac{j_T}{j_I} = \frac{|F|^2}{|A|^2}, \tag{2.30}$$

for $j_T = \frac{\hbar k}{m}|F|^2$.

2.2.2 Scattering matrices

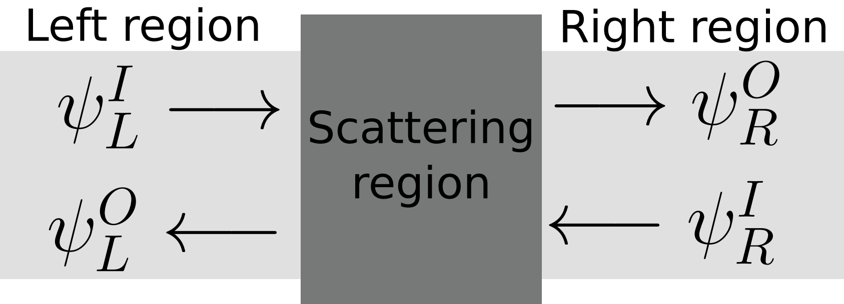

Figure 2.3: General scattering process representation.

As one can see the transmission in 2.30 depends only on the incoming and the outgoing amplitudes. Figure 2.3 shows a representation of a general scattering process for a single mode one dimensional system, where

$$\psi_L = \psi_L^I e^{ikx} + \psi_L^O e^{-ikx} \tag{2.31}$$

$$\psi_R = \psi_R^I e^{-ikx} + \psi_R^O e^{ikx} \tag{2.32}$$

ψ_L and ψ_R are the total wavefunction in the left and the right regions, respectively. The

wavefunctions 2.31 and 2.32 can be related by

$$\begin{pmatrix} \psi_L^O \\ \psi_R^O \end{pmatrix} = S \begin{pmatrix} \psi_L^I \\ \psi_R^I \end{pmatrix} \text{ with } S = \begin{pmatrix} r & t' \\ t & r' \end{pmatrix}. \tag{2.33}$$

The reflection (r) and transmission (t) coefficients links the incoming and outgoing amplitudes,

$$\psi_L^O = r\psi_L^I + t'\psi_R^I \tag{2.34}$$

$$\psi_R^O = t\psi_L^I + r'\psi_R^I. \tag{2.35}$$

The transmission and reflection probabilities are then expressed as $T = |t|^2$ and $R = |r|^2$. For a multi-mode scattering system, with equals N modes (channels) on the left and right side, the transmission and reflection coefficients are then represented by a $N \times N$ matrices. So, one can find the probability of an incoming wave in mode i on the left to be transmitted into a mode j is give as $T_{ji} = |t_{ji}|^2$, and $R_{ji} = |r_{ji}^2|$ to be reflected (FERRY *et al.*, 2009a).

2.2.3 Characteristic lengths

Table 2.1: Relevant length scales to quantum conductance. Table adapted from Datta, S. (1995). Electronic Transport in Mesoscopic Systems.

Length	Description
$1mm$	
	Mean free path in quantum Hall regime
$100\mu m$	
	Mean free path/Phase-relaxation length in high mobility semiconductor at $T < 4K$
$10\mu m$	
$1\mu m$	
	Commercial semiconductor devices (1990)
$100nm$	
	de Broglie wavelength in semiconductors Mean free path in polycrestalline metal films
$10nm$	
$1nm$	
	de Broglie wavelength in metals Distance between atoms
1Å	

Before continuing our study we will discuss about some quantities that must be mentioned when studying quantum transport phenomena at nano scale: *characteristic lengths*. Table 2.1 show some relevant length scales with some remarks about specifics range lengths. If any of the three dimensions of a conductor is smaller than one of the three characteristic length scales: (1) de Broglie wavelength of electrons; (2) the mean free path of electrons; and (3) the phase-relaxation length of electrons, the conductor will show conductance quantization behavior(DATTA, 1995; STEGMAN, 2014; GUSEV, 2005). The meaning of these characteristic lengths are described as follows,

- **Wavelength (λ)** The de Broglie wavelength is defined as

$$\lambda = \frac{2\pi\hbar}{p} = \frac{2\pi}{k}. \tag{2.36}$$

Considering the *Fermi wavenumber* $k_F = \sqrt{2\pi n_e}$, the Fermi wavelength is given as $\lambda_F = \sqrt{2\pi/n_e}$ and determines the wavelength of the electrons at Fermi energy.

- **Mean free path (L_m)** Describes the distance that the electron travels between collisions that can happen with impurities, phonons (lattice vibrations) or any other deviation from the perfect crystalline structure. The L_m is give as,

$$L_m = v_F \tau_m, \tag{2.37}$$

for v_f being the Fermi velocity and τ_m the momentum relaxation time.

- **Phase relaxation length (L_ϕ)** In quantum mechanics a particle is described in terms of a wavefunction, which has a *phase*. The phase relaxation length is the average distance after with the electron phase is randomized. This phase randomization happens when the electron "collides" with *fluctuating scatteres*, such as inelastic scattering by phonos, electron-electron collisions, magnetic impurities. L_ϕ is given as follows,

$$L_\phi^2 = D\tau_\phi, \tag{2.38}$$

where $D = v_F^2 \tau_m/2$, and τ_ϕ is the phase relaxation time. τ_ϕ describe the relaxation of a phase memory(GUSEV, 2005).

2.2.4 Hall measurements

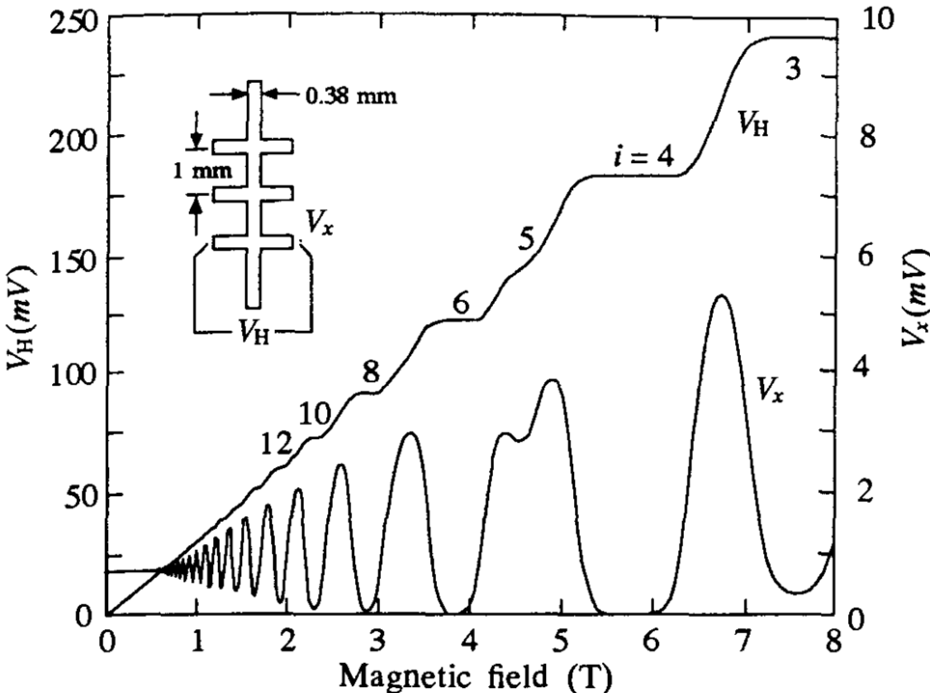

Figure 2.4: Longitudinal and transverses voltages for a modulation-doped GaAs film at $T = 1.2K(I = 25.5\mu A)$. The inset figure shows the Hall bridge with width $W = 0.38$ mm and length $L = 1$ mm used to do the measurements.

A basic tool used to characterize semiconductors is the Hall measurement. It consist of conductivity measurements in a weak magnetic field and allows to find the *carrier density* and *mobility* individually.

Considering the relation,

$$\left[\frac{d}{dt}\boldsymbol{p}\right]_{scattering} = \left[\frac{d}{dt}\boldsymbol{p}\right]_{field}, \tag{2.39}$$

which states that the rate which the electrons receive momentum from the total external field is equals to the rate at which they lose momentum due to scattering. In a system with non-zero electromagnetic field the Eq. 2.39 is given by,

$$m\frac{\boldsymbol{v}_d}{\tau_m} = e[\boldsymbol{E} + \boldsymbol{v}_d \times \boldsymbol{B}], \tag{2.40}$$

where $\boldsymbol{v}_d$ is the electron's drift velocity, and $\boldsymbol{B} = B\hat{z}$. Defining the *current density* as a

relation of the drift velocity and the electronic density,

$$\boldsymbol{j} = e\boldsymbol{v}_d n_e, \tag{2.41}$$

we can rewrite Eq. 2.39 in terms of its $x-$ and $y-$ components,

$$\begin{bmatrix} m/e\tau_m & -B \\ B & m/e\tau_m \end{bmatrix} \begin{pmatrix} J_x/en_e \\ J_y/en_e \end{pmatrix} = \begin{pmatrix} E_x \\ E_y \end{pmatrix}. \tag{2.42}$$

Taking $\mu \equiv |e|\tau_m/m$ and $\sigma \equiv |e|n_s\mu$, Eq. 2.42 becomes,

$$\frac{1}{\sigma}\begin{bmatrix} 1 & -B\mu \\ B\mu & 1 \end{bmatrix} \begin{pmatrix} J_x \\ J_y \end{pmatrix} = \begin{pmatrix} E_x \\ E_y \end{pmatrix}. \tag{2.43}$$

If we compare Eq. 2.44 with the resistivity tensor,

$$\begin{bmatrix} \rho_{xx} & \rho_{xy} \\ \rho_{yx} & \rho_{yy} \end{bmatrix} \begin{pmatrix} J_x \\ J_y \end{pmatrix} = \begin{pmatrix} E_x \\ E_y \end{pmatrix}, \tag{2.44}$$

we can find that the longitudinal resistance $\rho_{xx} = \frac{1}{\sigma}$ and the transverse equation $\rho_{yx} = -\rho_{xy} = B/|e|n_e$. This is the semiclassical prediction from the *Drude model* which predicts that longitudinal resistance is constant and the Hall (transverse) resistance increases linearly.

Figure 2.4 shows the experimentally measured longitudinal (V_x) and transverse (V_H) voltage drop, from which we can find the longitudinal and transverse resistivities respectively as $\rho_{xx} = \frac{V_x}{I}\frac{W}{L}$ and $\rho_{yx} = \frac{V_H}{I}$ (W is the device width and L its length). As we can see the semiclassical Drude model works for low magnetic fields, but it breaks for higher the longitudinal resistance show oscillations and there is the formation of plateaus in Hall resistance. These behaviors appears due to the formation of the Landau levels (DATTA, 1995; FERRY *et al.*, 2009b) which are associated with the discrete energy levels (see Eq. 2.88).

2.3 Landauer-Büttiker formalism

In Sec. 2.2.1 we introduced quantum transport by studying the transmission in one dimensional system. In this section we introduce the *Landauer formalism*, from which is possible to find the quantum conductance of quantum systems(DATTA, 1995; FERRY *et al.*, 2009b).

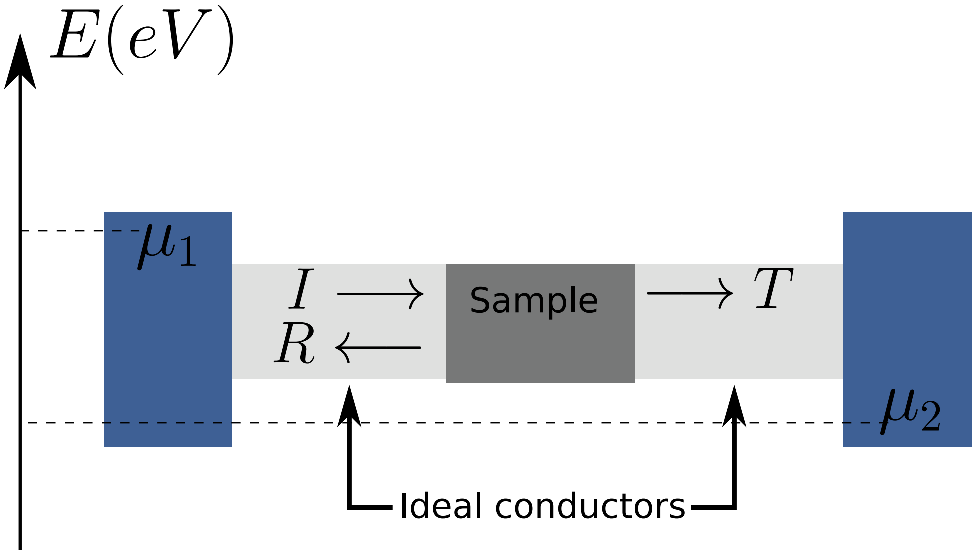

Figure 2.5: Representation of a two terminal devices, with ideal leads connecting the scattering region to reservoirs on the left and right.

Figure 2.5 shows the representation of a simple two terminal device. The ideal leads (do not cause scattering) connects the scattering region (sample material) to reservoirs on the left and right, respectively characterized by quasi-Fermi energies μ_1 and μ_2. For the current flow through the system there must be a potential difference, i.e., $\mu_1 \neq \mu_2$. Assuming low temperatures, the electrons are injected through the left lead up energy μ_L and injected through the right lead up to energy μ_1. The transmitted current can be calculated(FERRY *et al.*, 2009a)

$$I = 2e \int_{\mu_1}^{\mu_2} dEv(k)D(E)T(E), \tag{2.45}$$

where $v(k)$ is the velocity, $T(E)$ is the transmission coefficient, and $D(E)$ is the density of states. In the linear response regime, one can neglect the energy dependency of $T(E)$. So, considering the expression Eq. 2.7, and $D(E) = \frac{1}{2\pi \frac{dE}{dk}}$,

$$I = \frac{e}{\pi} \int_{\mu_L}^{\mu_R} dET(E) = \frac{e}{\pi\hbar} T(\mu_1 - \mu_2). \tag{2.46}$$

The factor $eV = \mu_1 - \mu_2$ is the voltage drop V across the scattering structure. From the differential conductance $G = \frac{dI}{dV}$ one can find the conductance from the transmission probability,

$$G = \frac{2e}{h}T. \tag{2.47}$$

The expression Eq.2.47 is the *Landauer* formula.

Multi-terminal case

Now, we are going to consider a system with multi-terminals (leads). Let's consider a system with several leads labeled $n = 1, 2, \cdots, N$, each with a corresponding chemical potential μ_n. Then, a scattering matrix that connects the states in lead n to the states in lead m can be defined (see Sec. 2.2.2). The total current transmitted to a lead m from a lead n is given by summing over all modes in the two leads,

$$I_{mn} = -\frac{2e^2}{h}V_n \sum_i^{N_i}\sum_j^{N_j} |t_{mi,nj}|^2. \tag{2.48}$$

V_n is the applied voltage, and N_i and N_j are the total modes in leads m and n, respectively.

The conservation of the current requires that the total current injected in a lead n must be transmitted to all the other leads. So,

$$N_n = R_n + \sum_{m,m\neq n} T_{mn}. \tag{2.49}$$

$$I_n = \frac{2e^2}{h}\left[(N_n - R_n)V_n - \sum_{m,m\neq n} T_{mn}V_m\right]. \tag{2.50}$$

Equation 2.50 is the *Landauer-Büttiker* formula for the multi-terminal systems(BÜTTIKER, 1986).

2.4 Tight-binding model

For large systems, with around 10^4 atoms or more, it becomes impracticable use most of self-consistence methods, such as the *density functional theory* (DFT) method(ROY, 2015). Instead we can use a semi-empirical method to calculate the band structure, where the interactions parameters are adjusted to match the experiment (or *ab-initio* calculations).

Considering a crystal with M atomic orbital ϕ_m per unit cell, labelled by index $m = 1, \cdots, M$, the Bloch states $\boldsymbol{\Phi_m}(\boldsymbol{k}, \boldsymbol{r})$ for a given position vector $\boldsymbol{r}$ and wave vector $\boldsymbol{k}$ can be written as

$$\boldsymbol{\Phi}_m(\boldsymbol{k}, \boldsymbol{r}) = \frac{1}{\sqrt{N}} \sum_{i=1}^{N} e^{i\boldsymbol{k}\cdot\boldsymbol{R}_{m,i}} \phi_m(\boldsymbol{r} - \boldsymbol{R}_{m,i}), \tag{2.51}$$

where N is the number of unit cells, $i = 1 \cdots N$ labels the unit cell, and $\boldsymbol{R}_{m,i}$ is the position vector of the m-th orbital in the ith unit cell. The electronic wave function $\boldsymbol{\Phi}_j(\boldsymbol{k}, \boldsymbol{r})$ may be expressed as a linear superposition of Bloch states

$$\boldsymbol{\Psi}_j(\boldsymbol{k}, \boldsymbol{r}) = \sum_{m=1}^{M} \boldsymbol{\psi}_j(\boldsymbol{k}, \boldsymbol{r}) \boldsymbol{\Phi}_m(\boldsymbol{k}, \boldsymbol{r}), \tag{2.52}$$

where $\boldsymbol{\psi}_j$ are expansion coefficients. There are M different energy bands, and the energy $E_j(\boldsymbol{k})$ of the j-th band is given by $E_j(\boldsymbol{k}) = \langle \psi_j | H | \psi_j \rangle / \langle \psi_j | \psi_j \rangle$ where

$$H = \frac{-\hbar^2}{2m} \nabla^2 + V(\boldsymbol{r}), \tag{2.53}$$

is the system Halmitonian. Minimising the energy E_j with respect to the expansion coefficients $\psi_{j,m}$ leads to

$$H\psi_j = E_j S \psi_j, \tag{2.54}$$

where ψ_j is a column vector, $\psi_j^T = (\psi_{j1}, \psi_{j2}, \cdots, \psi_{jM})$. The transfer integral matrix H and overlap integral matrix S are $M \times M$ matrices with matrix elements defined by

$$H_{m,m'} = \langle \phi_m | H | \phi_{m'} \rangle \tag{2.55}$$

$$S_{m,m'} = \langle \phi_m | \phi_{m'} \rangle. \tag{2.56}$$

The band energies E_j may be determined from the generalised eigenvalue equation

(2.54) by solving the secular equation

$$det(H - E_j S) = 0, \tag{2.57}$$

where "det" stands for the determinant of the matrix. In order to model a given system in terms of the generalised eigenvalue problem (2.54), it is necessary to determine the matrices H and S. Due to lattice periodicity, only the difference of position between two atoms matters. So, expanding the equations 2.55 and 2.56 in integral form,

$$H_{m,m'} = \sum_{\boldsymbol{R}} e^{-i\boldsymbol{k}\cdot\boldsymbol{R}} \int \phi^*_m(\boldsymbol{r}-\boldsymbol{R}) H \phi_{m'}(\boldsymbol{r}-\boldsymbol{R}) d\boldsymbol{r}, \tag{2.58}$$

$$S_{m,m'} = \sum_{\boldsymbol{R}} e^{-i\boldsymbol{k}\cdot\boldsymbol{R}} \int \phi^*_m(\boldsymbol{r}-\boldsymbol{R}) \phi_{m'}(\boldsymbol{r}-\boldsymbol{R}) d\boldsymbol{r}. \tag{2.59}$$

where $\boldsymbol{R} = \boldsymbol{R}_{m'} - \boldsymbol{R}_m$. In equations 2.58 and 2.59, the terms,are respectively the *hopping* parameter and *overlap* integral. These are the Slater-Koster(SLATER; KOSTER, 1954) and gives the energy difference that occurs when bonding atoms m and m'.

$$\gamma_{m,m'} = t_{m,m'} = \int \phi^*_m(\boldsymbol{r}-\boldsymbol{R}) H \phi_{m'}(\boldsymbol{r}-\boldsymbol{R}) d\boldsymbol{r}, \tag{2.60}$$

$$s_{m,m'} = \int \phi^*_m(\boldsymbol{r}-\boldsymbol{R}) \phi_{m'}(\boldsymbol{r}-\boldsymbol{R}) d\boldsymbol{r}. \tag{2.61}$$

Magnetic field on tight-binding models

The magnetic field is introduce in the TB system by applying the substitution

$$\boldsymbol{p} := \boldsymbol{p} + e\boldsymbol{A}(\boldsymbol{r}), \tag{2.62}$$

$\boldsymbol{p} = -i\hbar\nabla^2$ and $\boldsymbol{A}(\boldsymbol{r})$ is the vector potential associated with the magnetic field $\boldsymbol{B} = \nabla \times \boldsymbol{A}(\boldsymbol{r})$. The definition 2.62 is the Peierls substitution(Peierls, 1933).

One can define a *translation operator*(SAKURAI, 1994)

$$T(\boldsymbol{R}) = e^{\left(\frac{i}{\hbar}\boldsymbol{p}\cdot\boldsymbol{R}\right)}, \tag{2.63}$$

such that $T(\boldsymbol{R})\phi(\boldsymbol{r}) = \phi(\boldsymbol{r}+\boldsymbol{R})$. The operator 2.63 obeys the properties $T(\boldsymbol{R})^* = T(-\boldsymbol{R})$

and $T(\boldsymbol{R})T^*(\boldsymbol{R}) = \mathbb{1}$. So, the operator 2.63 with the substitution2.62 becomes(MOREAU, 2017),

$$T(\boldsymbol{R})(\phi(\boldsymbol{r})) = e^{\left(\frac{ie}{\hbar}\int_{\boldsymbol{R}_{m'}}^{\boldsymbol{R}_m} \boldsymbol{A}\cdot d\boldsymbol{r}\right)}. \tag{2.64}$$

As one can see from Eq. 2.64, the presence of magnetic adds phase to the wavefunction, called the Peierls phase. From Eq. 2.64, the hoopings parameter, defined by 2.60, becomes,

$$\gamma_{m,m'} = \int T(\boldsymbol{R})_m \phi^*_m(\boldsymbol{r} - \boldsymbol{R}) H T(-\boldsymbol{R})_{m'} \phi_{m'}(\boldsymbol{r} - \boldsymbol{R}) d\boldsymbol{r} \tag{2.65}$$

from we can derive(MOREAU, 2017)

$$\begin{aligned} \gamma_{m,m'}(\boldsymbol{A}) &= e^{\left(\frac{ie}{\hbar}\int_{\boldsymbol{R}_{m'}}^{\boldsymbol{R}_m} \boldsymbol{A}\cdot d\boldsymbol{r}\right)} \int \phi^*_m(\boldsymbol{r} - \boldsymbol{R}) H \phi_{m'}(\boldsymbol{r} - \boldsymbol{R}) d\boldsymbol{r}, \\ &= e^{\left(\frac{ie}{\hbar}\int_{\boldsymbol{R}_{m'}}^{\boldsymbol{R}_m} \boldsymbol{A}\cdot d\boldsymbol{r}\right)} \gamma_{m,m'}. \end{aligned} \tag{2.66}$$

2.4.1 Defects in tight-binding systems

In the tight-binding systems atomic vacancies are implemented in the Hamiltonian 2.59 by removing all the Hamiltonian matrix elements related to the removed atom: the orbitals localized about the central atom with all basis states describing the system. The remaining atoms are assumed to have their positions unaltered.

This procedure is referred as the *orbital-removal* method(KRIEGER; LAUFER, 1981) since the resulting Hamiltonian matrix, from which the eigenvalues and eigenvectors of the vacancy state are derived, is identical to the Hamiltonian matrix that would be obtained if the orbitals on the central atom were removed from the basis set and no other changes were made in the Hamiltonian matrix. This procedure is based on Koster and Slater (KOSTER; SLATER, 1954) previously work, who showed that the electronic energy levels introduced in the band gaps by a localized perturbation could be calculated from a knowledge of the Green's function for the perfect crystal and the matrix elements of the potential, both calculated in the Wannier representation.

2.4.2 Tight-binding in second quantization

The Hamiltonian 2.59 is defined in the frame of the first quantization, in which each particle is described by a wave function and the physical system is described in term of operators acting on the wave functions(SAKURAI, 1994; GRIFFTHS, 2004). A more

practical way to describe a quantum system is by using the second quantization formalism. This formalism is based on the *occupation number representation*, where the wavefunction is described by counting the number of particles n_i in each quantum state(SAKURAI, 1994). The Hamiltonian in this formalism is define as,

$$\hat{\boldsymbol{H}} = \sum_{m,m'} H_{mm} c^{\dagger}_{m'} c_m, \tag{2.67}$$

where $c^{\dagger}_{m'}$ and c_m are the fermionic creation and annihilation operators.

2.4.3 Phosphorene tight-binding model

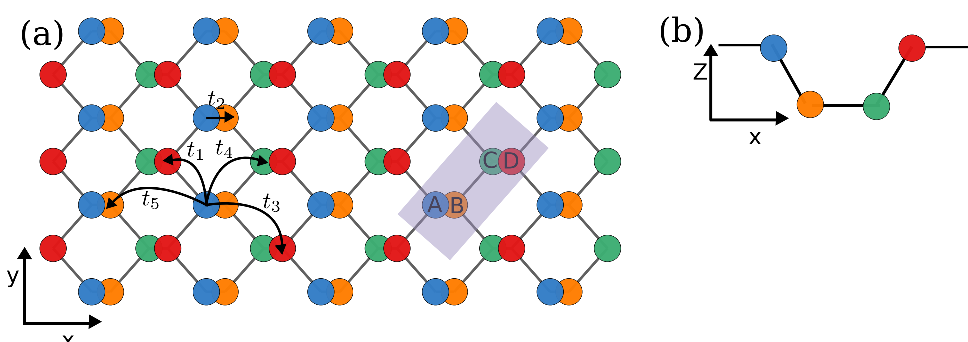

Figure 2.6: The phosphorene nanoribbon along the xy plane (a), and the representation in the zx plane (b). The different hoppings are shown in (a) and the rectangular shaded box gives the unit cell. The coloured dots refer to P atoms belonging to different sublattices (A, B, C and D).

The unit cell of phosphorene contains four atoms, with a_1 = 3.32Å and a_2 = 4.38Å being the primitive vectors and a = 2.22Å and θ = 96.79° are the in-plane bond length and bond angle, see Fig. 2.6. For our numerical simulations, we use the tight-binding model with five-hoppings as introduced in Ref. (RUDENKO; KATSNELSON, 2014). The tight-binding Hamiltonian is given by

$$H = \sum_{i} \epsilon_i n_i + \sum_{i \neq j} t_{ij} c^{\dagger}_i c_j, \tag{2.68}$$

where the sums run over the lattices sites, $c^{\dagger}_i(c_j)$ is the creation (annihilation) operator, ϵ_i is the electron on-site energy, t_{ij} are the elements of the hopping matrix. Because all phosphorene atoms are equivalent, we may set the on-site energy to zero. The five hopping parameters are given by t_1 = -1.220 eV, t_2 = 3.665 eV, t_3 = -0.205 eV, t_4 = -0.105

eV, and t_5 = -0.055 eV. They describe the band structure of phosphorene in the low-energy regime and agree with the one obtained from *DFT-GW* calculations (RUDENKO; KATSNELSON, 2014) (see Fig. 2.7).

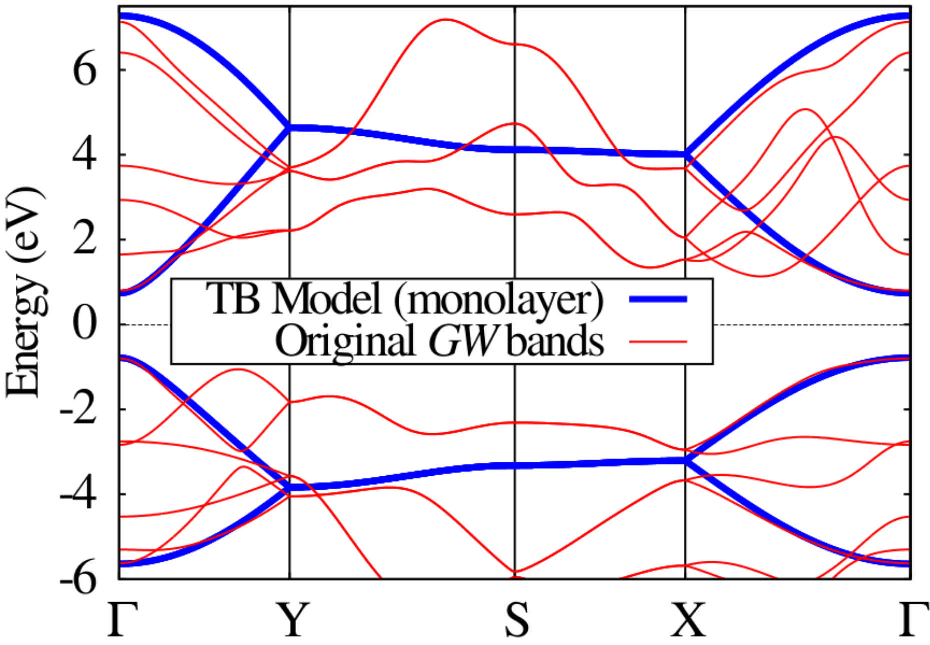

Figure 2.7: Band structures relation calculated using *DFT-GW* approximation in comparison with four-bands tight-binding model. Figure removed from *Phys. Rev. B* 89, 201408 (2014)

Rewriting the Hamiltioan Eq. 2.68 in terms of the hoppings, considering the sublattice A as the origin of the system, we have,

$$H = \sum_{i} \epsilon_i n_i + \sum_{i \neq j} \left(t^b_{ij} b^\dagger_i a_j + t^c_{ij} c^\dagger_i a_j + t^d_{ij} d^\dagger_i a_j \right) + h.c \tag{2.69}$$

a_j is the annihilation operator for the A sublattice, whereas b_i, c_i and d_i are the creation operators for the B, C and D sublattices. The creation and annihilation operators can be written in terms of each site as a Fourier transform,

$$a_i = \frac{1}{\sqrt{N}} \sum_k e^{i\boldsymbol{k}\cdot\boldsymbol{r}_i} a_k, \tag{2.70}$$

$$b_i^\dagger = \frac{1}{\sqrt{N}} \sum_k e^{i\boldsymbol{k}'\cdot\boldsymbol{r}_i} b_{k'}^\dagger, \tag{2.71}$$

$$c_i^\dagger = \frac{1}{\sqrt{N}} \sum_k e^{i\boldsymbol{k}''\cdot\boldsymbol{r}_i} c_{k''}^\dagger, \tag{2.72}$$

$$d_i^\dagger = \frac{1}{\sqrt{N}} \sum_k e^{i\boldsymbol{k}'''\cdot\boldsymbol{r}_i} d_{k'''}^\dagger. \tag{2.73}$$

Considering the relation $\delta(k - k') = \frac{1}{n}\sum_j e^{-i(\boldsymbol{k}-\boldsymbol{k}'')\cdot\boldsymbol{r}_i}$, the Hamiltonian Eq. 2.69 becomes,

$$H = \sum_i \epsilon_i n_i + \sum_k \sum_i \left(t_i^b e^{i\boldsymbol{k}\cdot\delta_i^b} b_k^\dagger a_k + t_i^c e^{i\boldsymbol{k}\cdot\delta_i^c} c_k^\dagger a_k + t_i^d e^{i\boldsymbol{k}\cdot\delta_i^d} d_k^\dagger a_k \right). \tag{2.74}$$

The parameters δ_i^w ($w = A, B, C$ or D) are the hoppings vector components projected in xy plane (SOUSA, 2018). Considering that each vector component is associated the hopping integral in as follows $t_1 \rightarrow \delta_1^b; \delta_2^b$, $t_2 \rightarrow \delta_1^c$, $t_3 \rightarrow \delta_3^b; \delta_4^b$, $t_4 \rightarrow \delta_1^d; \delta_2^d; \delta_3^d; \delta_4^d$ and $t_5 \rightarrow \delta_2^c$(CUNHA, 2022). We can then write,

$$t_{AB}(k) = \sum_i t_i^b e^{\boldsymbol{k}\cdot\delta_i^b} = t_1(e^{i\boldsymbol{k}\cdot\delta_1^b} + e^{i\boldsymbol{k}\cdot\delta_2^b}) + t_3(e^{i\boldsymbol{k}\cdot\delta_3^b} + e^{i\boldsymbol{k}\cdot\delta_4^b}), \tag{2.75}$$

$$t_{AC}(k) = \sum_i t_i^C e^{\boldsymbol{k}\cdot\delta_i^C} = t_2 e^{i\boldsymbol{k}\cdot\delta_1^c} + t_5 e^{i\boldsymbol{k}\cdot\delta_2^c}, \tag{2.76}$$

$$t_{AD}(k) = \sum_i t_i^d e^{\boldsymbol{k}\cdot\delta_i^d} = t_4(e^{i\boldsymbol{k}\cdot\delta_1^d} + e^{i\boldsymbol{k}\cdot\delta_2^d} + e^{i\boldsymbol{k}\cdot\delta_2^d} + e^{i\boldsymbol{k}\cdot\delta_2^d}). \tag{2.77}$$

So, we have the following Hamiltonian in the matrix form,

$$H = \begin{pmatrix} \epsilon_A & t_{AB}^*(k) & t_{AD}(k) & t_{AC}^*(k) \\ t_{AB}(k) & \epsilon_B & t_{AC}(k) & t_{AD}^*(k) \\ t_{AD}(k) & t_{AC}^*(k) & \epsilon_D & t_{AB}^*(k) \\ t_{AC}(k) & t_{AD}(k) & t_{AB}(k) & \epsilon_C \end{pmatrix}. \tag{2.78}$$

Due to the DH_2 point group invariance, we can reduce the four-band model two a two-band model(EZAWA, 2014). To do so, we consider the eigenstate equation,

$$\begin{pmatrix} \epsilon_A & t^*_{AB}(k) & t_{AD}(k) & t^*_{AC}(k) \\ t_{AB}(k) & \epsilon_B & t_{AC}(k) & t^*_{AD}(k) \\ t_{AD}(k) & t^*_{AC}(k) & \epsilon_D & t^*_{AB}(k) \\ t_{AC}(k) & t_{AD}(k) & t_{AB}(k) & \epsilon_C \end{pmatrix} \begin{pmatrix} \phi_A \\ \phi_B \\ \phi_C \\ \phi_d \end{pmatrix} = E \begin{pmatrix} \phi_A \\ \phi_B \\ \phi_D \\ \phi_C \end{pmatrix}, \tag{2.79}$$

which leads equations system,

$$\epsilon_A \phi_A + t^*_{AB}\phi_B + t_{AD}\phi_D + t^*_{AC}\phi_C = E\phi_A \tag{2.80}$$

$$t^*_{AB}\phi_A + \epsilon_B \phi_B + t_{AC}\phi_D + t^*_{AD}\phi_C = E\phi_B \tag{2.81}$$

$$t^*_{AD}\phi_A + t_{AC}\phi_B + \epsilon_C \phi_D + t^*_{AB}\phi_C = E\phi_D \tag{2.82}$$

$$t^*_{AC}\phi_A + t_{AD}\phi_B + t^*_{AB}\phi_D \epsilon_D \phi_C = E\phi_C \tag{2.83}$$

By subtracting Eq. 2.82 from Eq. 2.80 and Eq. 2.83 from Eq. 2.81, and adding Eqs. 2.80 and 2.82 and Eqs. 2.81 and 2.83, and considering $\epsilon_i = \epsilon$, the matrix system becomes,

$$\begin{pmatrix} \epsilon + t_{AD} & t^*_{AB} + t^*_{AC} & 0 & 0 \\ t_{AB} + t_{AC} & \epsilon + t_{AD} & 0 & 0 \\ 0 & 0 & \epsilon - t_{AD} & t^*_{AB} - t^*_{AC} \\ 0 & 0 & t_{AB} - t_{AC} & \epsilon - t_{AD} \end{pmatrix} \begin{pmatrix} \phi_A + \phi_D \\ \phi_B + \phi_C \\ \phi_A - \phi_D \\ \phi_B - \phi_C \end{pmatrix} = E \begin{pmatrix} \phi_A + \phi_D \\ \phi_B + \phi_C \\ \phi_A - \phi_D \\ \phi_B - \phi_C \end{pmatrix} \tag{2.84}$$

In this way, the Hamiltonian 2.78 can be written as,

$$H = \begin{pmatrix} H^+ & 0 \\ 0 & H^- \end{pmatrix}, \tag{2.85}$$

where,

$$H^\pm = \begin{pmatrix} \epsilon \pm t_{AD} & t^*_{AB} \pm t^*_{AC} \\ t_{AB} \pm t_{AC} & \epsilon \pm t_{AD} \end{pmatrix} \tag{2.86}$$

The peculiar electronic properties of the phosphorene band structure is shown in Fig. 2.8 (a) for the armchair edge and Fig. 2.8(b) for the zigzag edge, both with width $W = 50$ nm. The main difference between the two orientations is the presence of a quasi flat band within the band gap in the nanoribbon with zigzag edges resulting in metallic behavior (CARVALHO *et al.*, 2014; EZAWA, 2015), while the band structure for the armchair

terminal is semiconducting. The corresponding DOS are also shown.

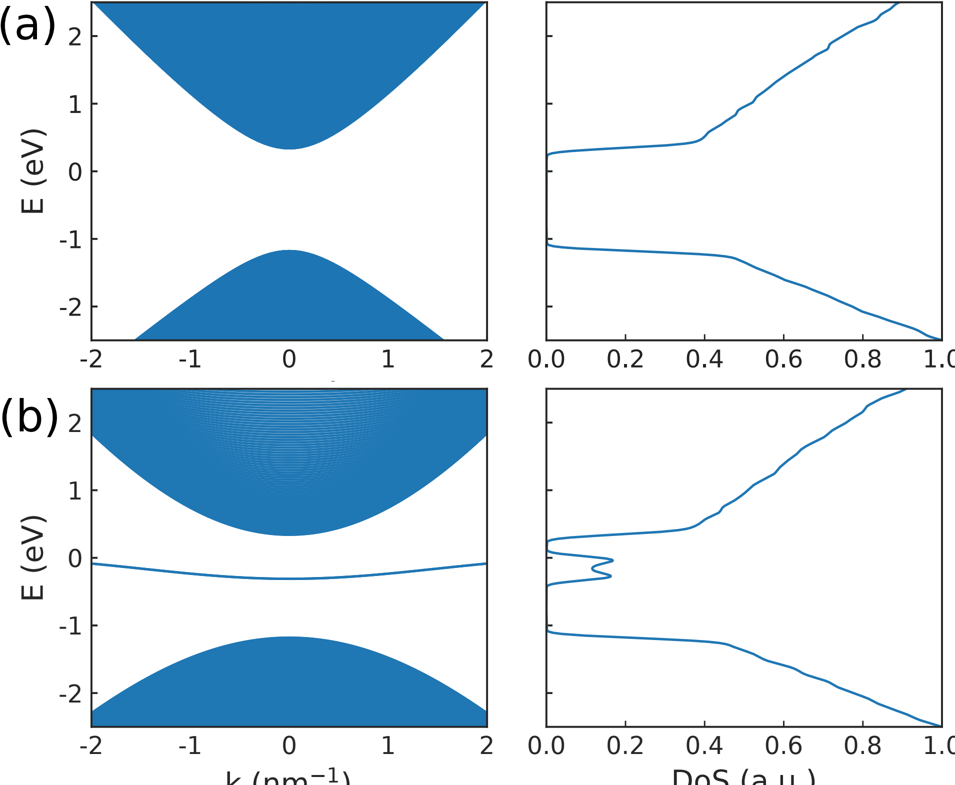

Figure 2.8: Phosphorene nanoribbon band structure and density of states for armchair (a), and zigzag (b) edges.

Landau levels in phosphorene sheet

The two band Hamiltonian for phosphorene 2.86 can be expressed in the low-energy approximation(ZHOU *et al.*, 2014; RUDENKO; KATSNELSON, 2014; TAHIR *et al.*, 2015)

$$H = \begin{pmatrix} E_c + \alpha^{'} k_x^2 + \beta k_y^2 & 0 \\ 0 & E_v - \lambda^{'} k_x^2 - \eta k_y^2 \end{pmatrix}, \tag{2.87}$$

for $E_c = 0.34$ eV ($E_v = -1.18$ eV) is the conduction (valence) band edge, $\alpha^{'} = \alpha + \gamma^2/E_g$, $\lambda^{'} = \lambda + \gamma^2/E_g$, $\gamma = -5.23$eV (which describe the interband coupling between the conduction band and valence band). The parameters related to the effective masses $\alpha = \hbar^2/2m_{cx}, \beta = \hbar^2/2m_{cy}, \lambda = \hbar^2/2m_{vx}, \eta = \hbar^2/m_{vy}$, where $m_{cx} = 0.793m_e, m_{cy} = 0.848m_e, m_{vx} = 1.363m_e, m_{vy} = 1.142m_e$ and m_e is the free electron mass. The energy gap is given by $E_g = E_c - E_v = 1.52$ eV.

Considering the Landau gauge $\boldsymbol{A} = Bx\hat{y}$ applied by the Peierls substitution(JIANG *et al.*, 2015) (see Eq.2.62), we obtain the eigenvalues from the Hamiltonian 2.87,

$$E_{n,s} = E_s + s\hbar\omega_s \left(n + \frac{1}{2}\right), n = 0, 1, 2, 3, ..., \tag{2.88}$$

$s = \pm 1$ relates the $(+)$conduction and (-)valence band, n represents the Landau index(ZHOU *et al.*, 2014; JIANG *et al.*, 2015), $E_{+,-} = E_{c,v}, \omega_{+,-} = \omega^{'}_{c,v}$ with $\omega^{'}_{c} = eB/(m^{'}_{cx}m_{cy})^{1/2} = 2.657\omega_e$ and $\omega^{'}_{v} = eB/(m^{'}_{vx}m_{vy})^{1/2} = 2.182\omega_e$, with $\omega_e = eB/m_e$.

Figure 2.9 shows the Landau spectra calculated by Eq. 2.88. As one can see dispersion is typical of 2D electron gas system, exhibiting linear dependence with B. The Fermi energy E_F can be found by,

$$n_c = \sum_{-\infty}^{\infty} D(E)f(E) = \frac{g_s}{D_0}\sum_{n,s} f(E^s_n) \tag{2.89}$$

$D(E)$ is the density of states,$g_s = 2$ is the spin degeneracy, $D_0 = 2\pi l^2$, $l = \sqrt{\hbar/eB}$, and the Fermi-Dirac distribution function is written as $f(E - n^s) = (1 + \exp\beta(E^s_n - E_f))^{-1}$. The magenta curve in Fig. 2.9 is numeric calculated from Eq. 2.89. It shows that as the magnetic field increases the Landau levels leaks out of the Fermi level.

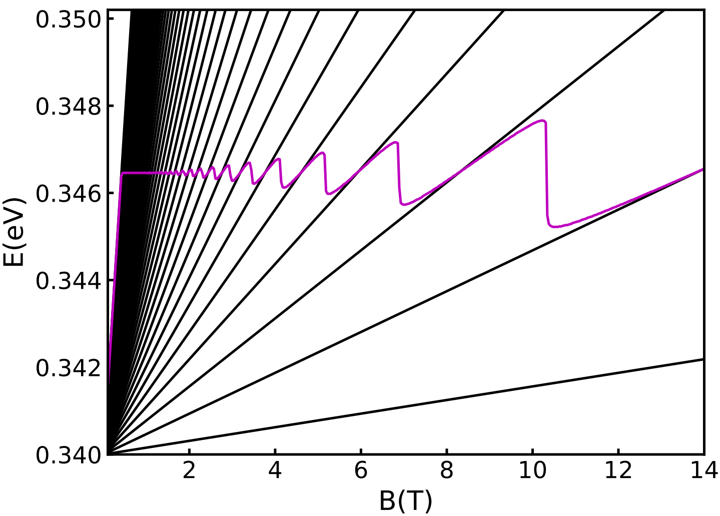

Figure 2.9: The Fermi energy (magenta) as function of magnetic field for density $n_c = 1x10^{16}m^{-2}$.

2.4.4 Tight-binding model for BLG

BLG is formed by two MLG stacked over each other(NETO *et al.*, 2009a; MCCANN; KOSHINO, 2013; ROZHKOV *et al.*, 2016). Its unit cell is composed by four sublattices,

labeled as A_1 and B_1 for layer 1 and A_2 and B_2 for layer 2. The two most common stacks investigated in the literature (NETO *et al.*, 2009a; MCCANN; KOSHINO, 2013; MCCANN, 2006) are the AB-stacking (named also as Bernal stacking), where atoms in the A_1 sublattice in the bottom layer are linked with B_2 atoms in the top layer, forming a dimer(MCCANN, 2006), and the AA-stacking, where the atoms in the upper and lower layers are located directly on top of each other. Their crystal structures are sketched in Figs. 2.10(a) for the AA-stack and 2.10(b) for the AB-stack. We included only the most significant interlayer hopping term, which is the perpendicular one between the dimer sublattices, γ_1. The other interlayer hopping parameters γ_3 and γ_4 describe interlayer skew couplings between nondimer atoms A_2 and B_1, and between dimer and nondimer atoms A_1 and A_2 or B_1 and B_2, respectively. They are related to the trigonal warping effect leading to an anisotropic band and the electron-hole band asymmetry, respectively, which is beyond the main scope of our discussions since the most significant physics investigated here is happening around the Fermi energy and is associated with the zero-modes induced by the vacancies.

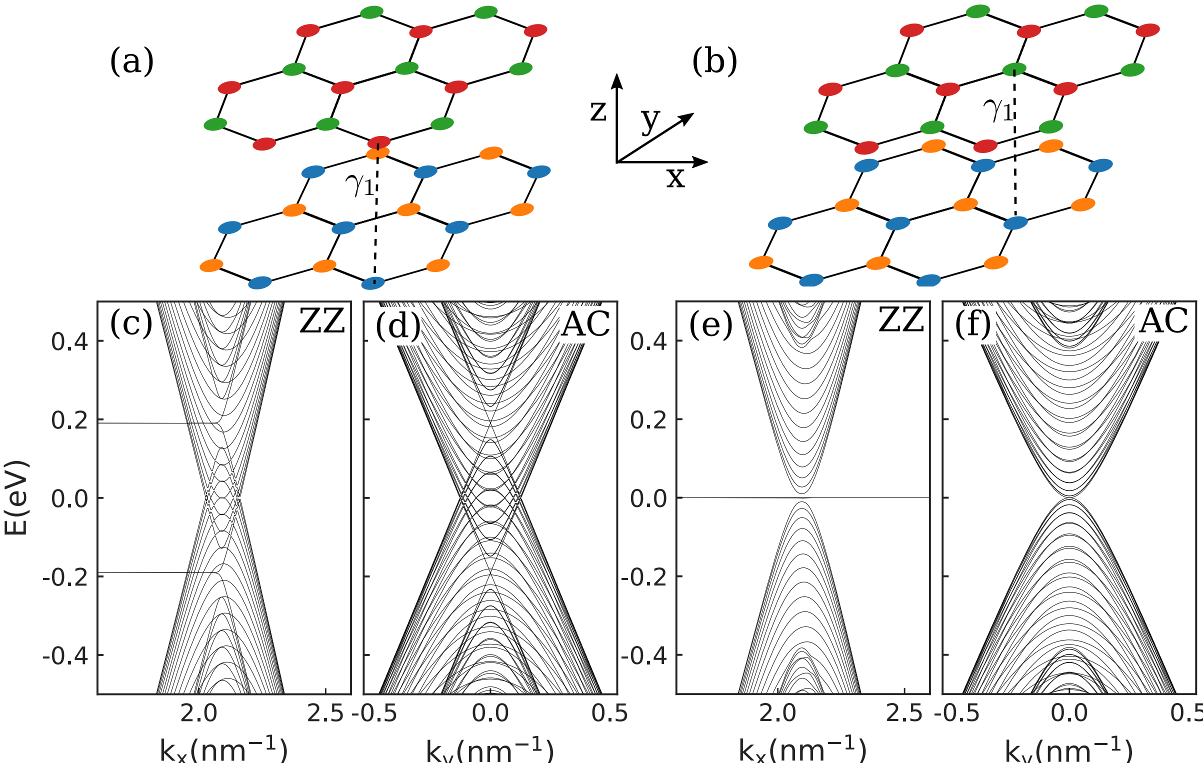

Figure 2.10: Lattice structure of (a) AA-stacking BLG and (b) AB-stacking BLG. (c-f) Band structures of BLG nanoribbons for ribbon width of 50 nm and different stacking and edges: (c, d) AA-stack, (e, f) AB-stack, (c, e) zigzag, and (d, f) armchair.

The electronic properties of charge carriers in BLG are described here by employing

the TB approach within the nearest-neighbor approximation. The TB Hamiltonian for BLG nanoribbons reads explicitly for AB and AA stacking respectively as

$$H_{AB} = H_M - \gamma_1^{AB} \sum_i (a_{1,i}^\dagger b_{2,i} + h.c.), \tag{2.90a}$$

$$H_{AA} = H_M - \gamma_1^{AA} \sum_{i,j} (a_{1,i}^\dagger a_{2,i} + b_{1,j}^\dagger b_{2,j} + h.c.), \tag{2.90b}$$

where

$$H_M = -\gamma_0 \sum_{m,i\neq j} (a_{m,i}^\dagger b_{m,j} + h.c.), \tag{2.90c}$$

where $a_{m,i}^\dagger$ ($a_{m,i}$) creates (annihilates) an electron in site i of sublattice A_m and the operators $b_{m,j}^\dagger$ ($b_{m,j}$) act on the sublattice B_m with $m = 1, 2$ being the layer index. $\gamma_0 = 3.16$ eV is the intralayer hopping between nearest neighbour $A_m - B_m$ sublattices, and $\gamma_1^{AB} = 2\gamma_1^{AA} \approx 0.38$ eV is the interlayer hopping value in AB and AA BLG stack type. We assume that the on-site energy is null, resulting in an electron–hole symmetry for the nanoribbons energy spectra, i.e., it is symmetric with respect to zero energy (RAKHMANOV *et al.*, 2012; MCCANN, 2006). In all calculations discussed here, we neglected the electron-electron interaction. Recent experimental measurements of the confinement properties in BLG-based nanostructures using scanning tunneling microscope (GE *et al.*, 2020; KALADZHYAN *et al.*, 2021b; KALADZHYAN *et al.*, 2021a; GE *et al.*, 2021; JOUCKEN *et al.*, 2021b; JOUCKEN *et al.*, 2021a) have been confirmed by single-particle tight-binding calculations, even in the presence of charge defects, impurities, dopants and adatoms (KALADZHYAN *et al.*, 2021a; JOUCKEN *et al.*, 2021b; JOUCKEN *et al.*, 2021a), showing that the theoretical framework used here is valid within certain regimes and allows us to have physical insights in the effects of disorder on the electronic and transport properties of BLG nanostructures.

Figures 2.10(c)-2.10(f) show the band structures for the AA (Figs. 2.10(c, d)) and AB (Figs. 2.10(e, f)) stacked BLG nanoribbons with ribbon width $W = 50$ nm. Two different nanoribbon boundary terminations are considered: zigzag edge (Figs. 2.10(c, e)), and armchair edge (Figs. 2.10(d, f)). It is well-known in the literature(BREY; FERTIG, 2006; WAKABAYASHI *et al.*, 2009; WAKABAYASHI *et al.*, 2010; ROZHKOV *et al.*, 2011; STAMPFER *et al.*, 2011; WEISS *et al.*, 2012; YAGMURCUKARDES *et al.*, 2016;

DUTTA; PATI, 2010; SON *et al.*, 2006a; YANG *et al.*, 2007; ROZHKOV *et al.*, 2009; SON *et al.*, 2006b; BANDEIRA *et al.*, 2020) that armchair MLG nanoribbons present a width-dependent physics, exhibiting either metallic or semiconducting behavior depending on its width, whereas zigzag MLG nanoribbons exhibit a metallic behavior with non-dispersive states in the middle gap, corresponding to surface states strongly localized near the edges. Such general features of edge state physics for zigzag nanoribbons and width-dependent physics for armchair nanoribbons hold true for AB-stacked BLG nanoribbons, as depicted in Figs. 2.10(e)-2.10(f). Note that for the chosen width, the armchair AB-stacked BLG nanoribbon is metallic, such that the lowest parabolic bands touching each other at $E = 0$. On the other hand, the lowest energy states of AA-stacked BLG nanoribbons are composed by linear energy spectra consisting by two Dirac cones shifted by $2\gamma_1^{AA}$ (see Figs. 2.10(c)-2.10(d)). In addition, for zigzag AA-stacked BLG nanoribbons, the flat states become split (see Fig. 2.10(c)), exhibiting energies either above or below the Fermi level by a value of γ_1^{AA}. Unlike the AB-stacked BLG case, both zigzag and armchair AA-stacked BLG nanoribbon are metallic regardless of the number of carbon lines.

2.5 Software and numerical methods

For our numerical calculations, we will make use of KWANT(GROTH *et al.*, 2014), an open source *Python* package for numerical simulation of TB systems with emphasis on quantum transport. It has built-in functions to easily calculate system's transport electronic properties such as band structure, DOS, conductivity, and probability current density. It is able to solve the scattering problem based on a matching wavefunction (see Appendix 7) approach (ZWIERZYCKI *et al.*, 2008) to calculate the transmission of a n-propagating mode in a contact terminal to a m-th mode in another contact. This formulation is mathematically equivalent to the non-equilibrium Green's function with the advantage to be numerically more stable (GROTH *et al.*, 2014).

Considering a system with a single lead attached to a scattering region, we can define the Hamiltonian of such a system has the tridiagonal block form

$$H = \begin{pmatrix} \ddots & V_L & & & \\ V_L^\dagger & H_L & V_L & & \\ & V_L^\dagger & H_L & V_{LS} \\ & & V_{LS}^\dagger & H_S \end{pmatrix} \tag{2.91}$$

where H_S is the (typically large) Hamiltonian matrix of the scattering region S. H_L is the (typically much smaller) Hamiltonian of one unit cell of the lead, while the block submatrix is the Hamiltonian V_L connecting one unit cell of the lead to the next. Finally, V_{LS} is the hopping from the system to the leads.

We define the wave function of an infinite system as $(\cdots, \boldsymbol{\psi}^L(2), \boldsymbol{\psi}^L(1), \boldsymbol{\psi}^S)$, where $\boldsymbol{\psi}^S$ is the wave function in the scattering region, and $\boldsymbol{\psi}^L(i)$ the wave function in the i-th unit cell away from the scattering region in the lead. Due to the translational invariance of the leads, the general form of the wave function in them is a superposition of plane waves. The eigenstates of the translation operator in the lead take the form

$$\phi_n(j) = (\lambda_n)^j \chi_n, \tag{2.92}$$

where χ_j is the n-th eigenvector of a lead j and λ_n the n-th eigenvalue of the Schrödinger equation

$$(H_L + V_L \lambda_n^{-1} + V_L^\dagger \lambda_n)\chi_n = E\chi_b. \tag{2.93}$$

The eigenstates of Eq. 2.93 can describes evanescent modes, if $|\lambda_n| < 1$, or propagating modes, if $\lambda_n = e^{ik_n}$, where k_n is the longitudinal momentum of the mode n. The scattering states in the leads takes the form

$$\psi_n(i) = \phi_n^{in}(i) + \sum_m S_{mn}\phi_m^{out}(i) + \sum_p \tilde{S}_{pn}\phi_p^{ev}(i) \tag{2.94}$$

$\phi_n^{in}(i)$, $\phi_n^{out}(i)$ and $\phi_n^{ev}(i)$ are the incoming, outgoing and evanescent modes. The scattering matrix S_{mn} and wavefunction inside the scattering region $\phi_n(0) = \phi_n^S$ are the main raw outputs of KWANT.

To calculate the DOS, KWANT makes use of the Kernel Polynomial Method (WEIßE *et al.*, 2006) which is an efficient way to calculate spectral quantities of large systems in condensed matter physics. With the energy spectrum in hand, the mathematical concept of the DOS calculation is simply a superposition of individual energy states which one

broadens using a Gaussian function $f(E) = \exp[-(E - E_0)^2/\Gamma^2]$, with a broadening factor usually chosen smaller than the energy levels separations. A broadening factor of $\Gamma = 0.01$ eV will be assumed for all of our calculations, unless otherwise stated.

3 HALL AND BEND RESISTANCE OF A PHOSPHORENE HALL BAR

3.1 Introduction

Vacancies in phosphorene were reported to exhibit a highly anisotropic and delocalized charge density, with intrinsic vacancies resulting in in-gap resonance states (KIRALY *et al.*, 2017; LIU *et al.*, 2014; LIU *et al.*, 2016). In the absence of a magnetic field, the effects of different types of vacancies in phosphorene ML were theoretically investigated in multi-terminal systems showing that the presence of atomic defects decrease (an increase) the longitudinal (transverse) conductance (LI; PEETERS, 2018; SHAH *et al.*, 2019). Studies on graphene showed that vacancy disorder can cause the appearance of new states in the Landau spectrum, which depend on the type and density of vacancies, which can be observed in the bend resistance and the density of states (DOS) (PETROVIĆ; PEETERS, 2016). To provide insights on how vacancies affect the transport properties of phosphorene, we analyze the different resistances in a Hall bar configuration.

It is important to mention that Hall measurements can accurately determine the carrier density, electrical resistivity, and the mobility of carriers in semiconductors (DATTA, 1995). It is well known that 2D electron gas submitted to a perpendicular magnetic field leads to the formation of Landau levels, and as a consequence it leads to the formation of quantized levels and oscillations in the Hall and longitudinal conductivity/resistance (DATTA, 1995; PEREIRA; KATSNELSON, 2015; TAHIR *et al.*, 2015). With the application of a perpendicular magnetic field it is also possible to focus electrons injected from a narrow injector allowing the study of different properties of a material (MILOVANOVIC *et al.*, 2014) in such a magnetic focusing experiment.

3.2 System and methods

As described in Sec. 2.4.3, the phosphorene ML is modelled using a four band tight-binding model, but can be reduced to a two-band model due to the symmetry between the sublattices A and D (SOUSA *et al.*, 2017) [see Fig. 2.6]. In this reduced form the number of atoms in sublattices, labeled A and B for convenience, are N_A and N_B. For pristine ML phosphorene (without defects), $N_A = N_B$ (sublattice symmetry). In this system, vacancies are introduced by randomly removing atoms from the phosphorene lattice, eliminating the on-site energy and the hopping of the removed atom. Figure 3.1 shows sections of the defective phosphorene Hall bar with three types of atomic vacancies:

A single vacancy (SV) where a single sublattice atom is removed, a type-I double vacancy (DV1) where an atom and its neighbor sublattice atom on a different z-plane are removed, and a type-II double vacancy (DV2) where the neighbor sublattice atom is removed on the same z-plane.

In the SV case, where only one of the sublattice atoms is removed, the sublattice symmetry is broken ($N_A \neq N_B$). For the type-I DV, where two sublattice atoms are removed, being two A (or two B), the sublattice symmetry is also broken ($N_A \neq N_B$). However for type-II, where one A and one B are removed, the symmetry is preserved ($N_A = N_B$).

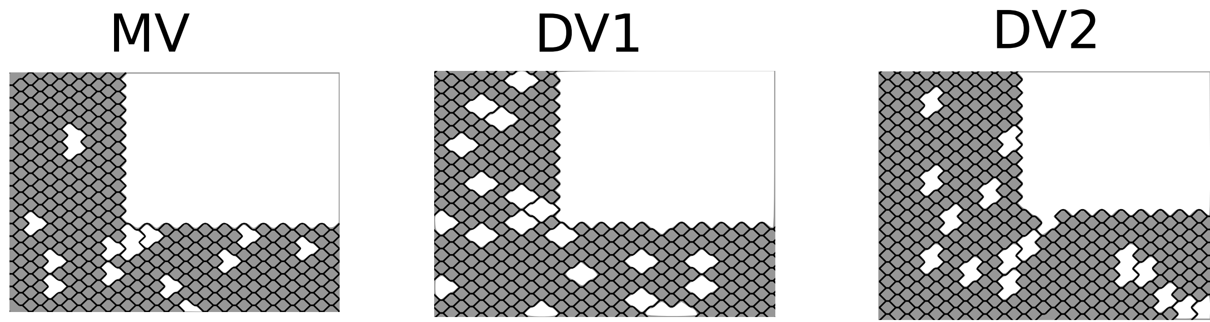

Figure 3.1: The disorders in phosphorene Hall bar for single vacancies (SVs), double vacancy type I (DV1) and type II (DV2). Only half of the Hall bar is shown.

3.2.1 Hall bar

The Hall device is schematically presented in Fig. 3.2. It is a four-terminal Hall bar system with an applied magnetic field in the z-direction, where the magnetic field is introduced through the vector potential.

The Landau gauge $\vec{A}_H = -By\vec{e}_x$ is one of the standard gauges which works only for leads with translational symmetry in x-direction. For y-translational symmetry we need to change it to the gauge $\vec{A}_V = Bx\vec{e}_y$, as for these leads the system goes to infinite in the y-direction. In the scattering region we need to implement a way to change from the gauge $\vec{A}_H$ to $\vec{A}_V$. The change from one gauge to the other is done smoothly by implementing the scalar function $f(x, y)$ which rotates the vector potential $\vec{A'} = \vec{A} + \vec{\partial} f$, where f is defined as (SHEVTSOV *et al.*, 2012; PETROVIĆ; PEETERS, 2016),

$$f(x, y) = Bxy \sin^2 \theta + \frac{1}{4} B(x^2 - y^2) \sin 2\theta, \tag{3.1}$$

here θ is the angle between the two leads (in our system $\theta = \pi/2$). In order to apply

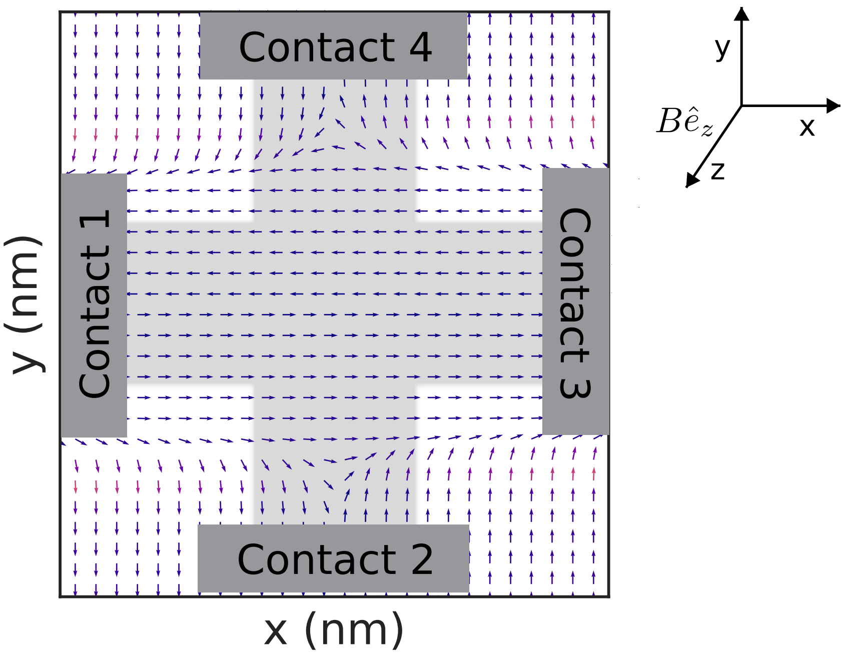

Figure 3.2: Schematic representation of the Hall bar. The modified vector field $\vec{A}'(x, y)$ is shown by the arrows.

$f(x, y)$ only in the main region we multiply it by a smooth step function $\epsilon_i(y) = \frac{1}{2}(1 + \tanh(2(y - y_0)/d))$, which is non-zero only close to the lead i. y_0 is the crossover position and d is the width of the crossover region. For our numerical calculations we took $y_0 = W$ and $d = W/5$, where $W = 50nm$ (PETROVIĆ; PEETERS, 2016). The modified magnetic field is then implemented on the tight-binding Hamiltonian (2.68) by making use of the Peierls substitution $t_{ij} = t_{ij}e^{i\phi_{ij}}$. The Peierls phase is then described as,

$$\phi_{ij} = \int_{\vec{r_j}}^{\vec{r_i}} \vec{A} \cdot d\vec{r}. \tag{3.2}$$

The resistances are calculated using Landauer-Büttiker formula (BÜTTIKER, 1986). The four-terminal resistance in a cross shaped structure is given by

$$R_{mn,kl} = \frac{h}{2e^2}\left(\frac{T_{km}T_{ln} - T_{kn}T_{lm}}{D}\right), \tag{3.3}$$

where h is the Planck constant. $R_{mn,kl}$ is the resistance with the voltage being measured between the leads k and l when the current is driven into contact m and taken out from

contact n. In Eq. (3.3) $D = (\alpha_{11}\alpha_{22} - \alpha_{12}\alpha_{21})S$, with

$$\begin{aligned}
\alpha_{11} &= [(T_{21} + T_{31} + T_{41})S - (T_{14} + T_{12})(T_{41} + T_{21})]/S \\
\alpha_{12} &= (T_{12}T_{34} - T_{14}T_{32})/S \\
\alpha_{21} &= (T_{21}T_{43} - T_{41}T_{23})/S \\
\alpha_{22} &= [(T_{12} + T_{32} + T_{42})S - (T_{21} + T_{23})(T_{32} + T_{12})]/S,
\end{aligned}$$

where $S = T_{12} + T_{14} + T_{32} + T_{34}$, and T_{ij} is the transmission probability from lead j to lead i. The resistances given by Eq. (3.3) satisfy the relation $R_{mn,lk} = R_{nm,kl}$ and the reciprocity relation $R_{mn,kl}(B) = R_{kl,mn}(-B)$ (BÜTTIKER, 1986). In this work we are also going to analyse the longitudinal resistance defined as $R_{13,13}$ ($R_{24,24}$) which represents the resistance between the two opposites armchair (zigzag) terminals. This schematic can also be calculated, in a first approximation (FERRY *et al.*, 2009b), by the analogous two-terminals systems, where the resistance is simply proportional to the transmission between the terminals (FERRY *et al.*, 2009b; DATTA, 1995).

3.3 Pristine phosphorene Hall bar

Due to the anisotropy of the lattice, the Landau level splitting depends strongly the orientation and on the edge type of the phosphorene nanoribbon (EZAWA, 2015; ZHOU *et al.*, 2014). This dependency is shown in Fig. 3.3-(a), where the electron energy spectrum for the armchair (ac) and zigzag (zz) nanoribon is plotted against the magnetic field, for nanoribbons with width $W = 50$ nm. For the zigzag orientation the effective electron mass is much smaller than the one for the armchair nanoribbon. That is the origin of the different spacing and magnetic field dependency of the Landau levels (EZAWA, 2015; ZHOU *et al.*, 2014).

Next, we analyze the resistances for Fermi energy near the intersecting points depicted in Fig. 3.3-(a). The Hall ($R_{13,42}$) and bend ($R_{14,23}$) resistances were calculated for a Hall bar with terminals size 50 nm (with a total of 342,384 atoms in the system). Figure 3.3-(b) shows the resistance dependence on the Fermi energy ($E_F > 0$ for electrons and $E_F < 0$ for holes) for two different values of the applied magnetic field (5T and 10T). As the energy approaches the edges of the band, one can see the Hall resistance goes to infinity while the bend resistance goes to zero. The transition between two plateaus in

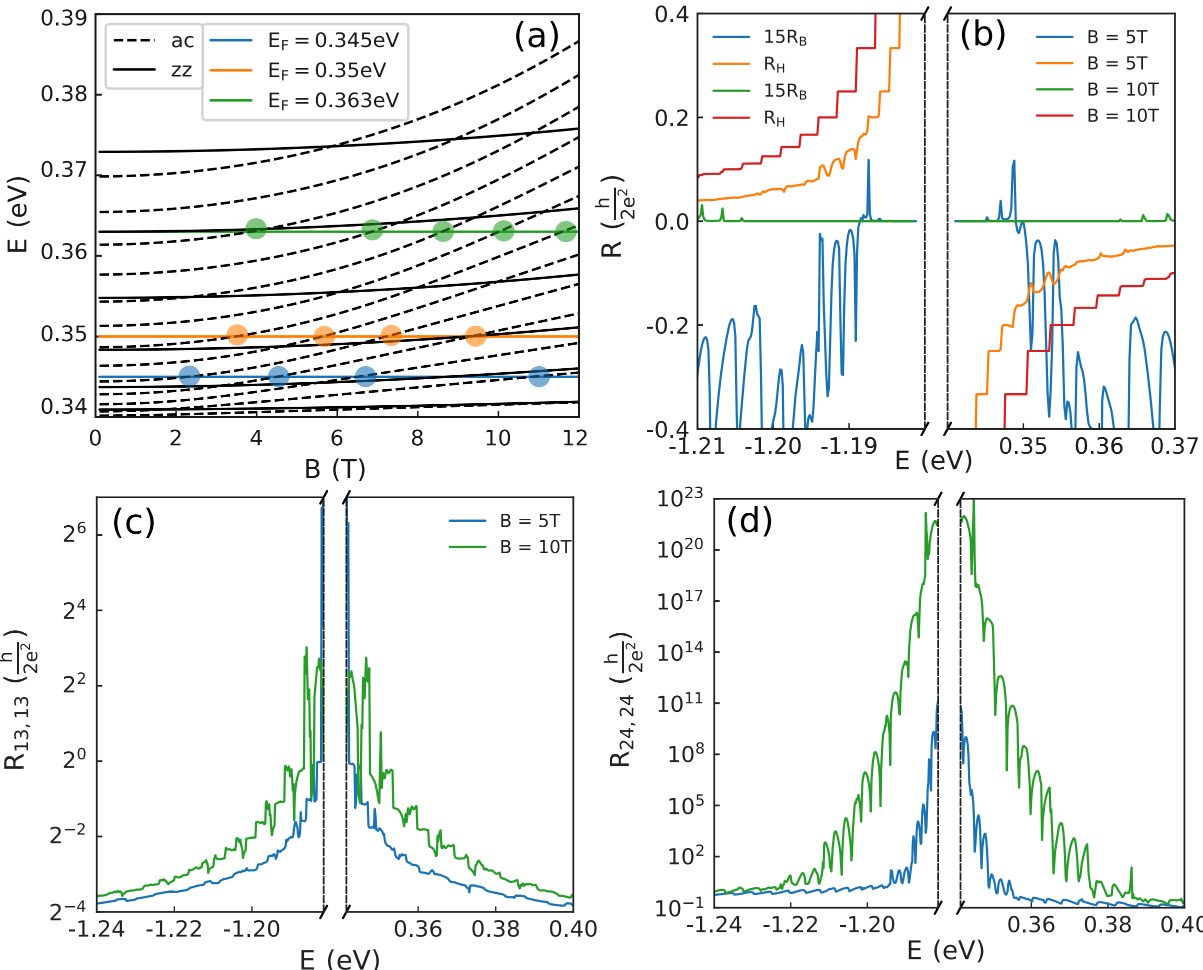

Figure 3.3: (a) The phosphorene energy levels for nanoribbons as function of magnetic field. The nanoribbons with width $W_{ac} = 50$ nm and $W_{zz} = 50$ nm correspond to the semi-infinite leads in the Hall bar. The points in the figure indicate the intersection of the Fermi energy (E_F) with the Landau levels. (b) Hall ($R_{13,42}$) and bend ($R_{14,23}$) resistance dependency on the Fermi energy for two different values of the magnetic field. Longitudinal resistance, measured for the (c) armchair terminals ($R_{13,13}$) and for the (d) zigzag terminals ($R_{24,24}$), varying with the Fermi energy for two different values of the magnetic field.

the Hall resistance indicate the points where the Fermi energy crosses a semiconductor transverse mode (see Fig. 3.3-(a)) formed due the presence of magnetic field. Notice that at such points the bend resistance exhibits a negative dip. Another interesting phenomena is the presence of negative values in the bend resistance, indicating a ballistic regime (the ballistic regime will be discussed further when analyzing the resistances as a function of magnetic field).

To study the effect of the ribbon orientation the longitudinal resistances $R_{13,13}$ and $R_{24,24}$ are shown in Fig. 3.3-(c-d). These resistances were calculated using the two-terminal relation for the resistances, which is just the inverse of the transmission between the two opposite terminals. Due to the anisotropic spectrum in phosphorene, one would expect that $\sigma_{xx} < \sigma_{yy}$, leading to $R_{13,13} > R_{24,24}$, but for Hall bar, the opposite happens. This is due to the presence of a scattering region in the Hall bar, that affects the conductivity making $\sigma_{xx} > \sigma_{yy}$ and also $R_{13,13} < R_{24,24}$, as explained in Ref. (SHAH *et al.*, 2019) for a cross-shaped phosphorene nanoribbon.

Next, we investigate the different resistances as a function of the magnetic field for a fixed Fermi energy. It is well known that as the magnetic field increases, the Fermi energy crosses the semiconductor (armchair) transverse modes, resulting in well defined plateaus in the Hall resistance (ZHOU *et al.*, 2014). In the system studied here, this behavior is clear for $E_F = 0.345$ eV and 0.34 eV (Figs. **??**-(a) and **??**-(b)). However, for $E_F = 0.363$ eV (Fig. **??**-(c)) the plateaus in the Hall resistance are almost absent for a weak magnetic field. This can be explained by looking at Fig. 3.3-(a). The Fermi energy $E_F = 0.363$ eV is matches a zigzag transverse mode (for most of the spectrum), which is almost magnetic-field independent (ZHOU *et al.*, 2014). Due to the metallic character, zigzag terminals induce scattering between the transport modes, not allowing the formation of quantized plateaus in the Hall resistance (SHAH *et al.*, 2019). However, as the magnetic field increases, the energy of the zigzag Landau level differs from the Fermi energy, and the plateaus on the Hall bar are recovered.

The ballistic regime observed in Fig. 3.3-(b) becomes more evident when analyzing the magnetic-field dependency reported in Figs. 3.4. The bend resistances in Figs. 3.4 are plotted in panel (a) (blue curve) which goes to zero as the magnetic field increases. A negative bend resistance indicates that the electron trajectory does not bend to the closer non-axial terminal (TAKAGAKI *et al.*, 1989; WEINGART *et al.*, 2009). We can

understand this negative value by considering the definition of the four terminal resistance as $R_{ij,km} = V_{km}/I_{ij}$ (BÜTTIKER, 1986). For $R_{14,23}$, we have $V_{23} = V_2 - V_3$, indicating that $V_{23} < 0$, as V_2 is a zigzag (lower energy) terminal and V_3 is an armchair (high energy) terminal. Even though the bend resistance approaches zero, one can still see peaks in the resistances, indicating an increase in the transmission between axial terminals. These peaks happens whenever the Fermi energy cross an armchair transverse mode indicating an increase in the xx conductivity.

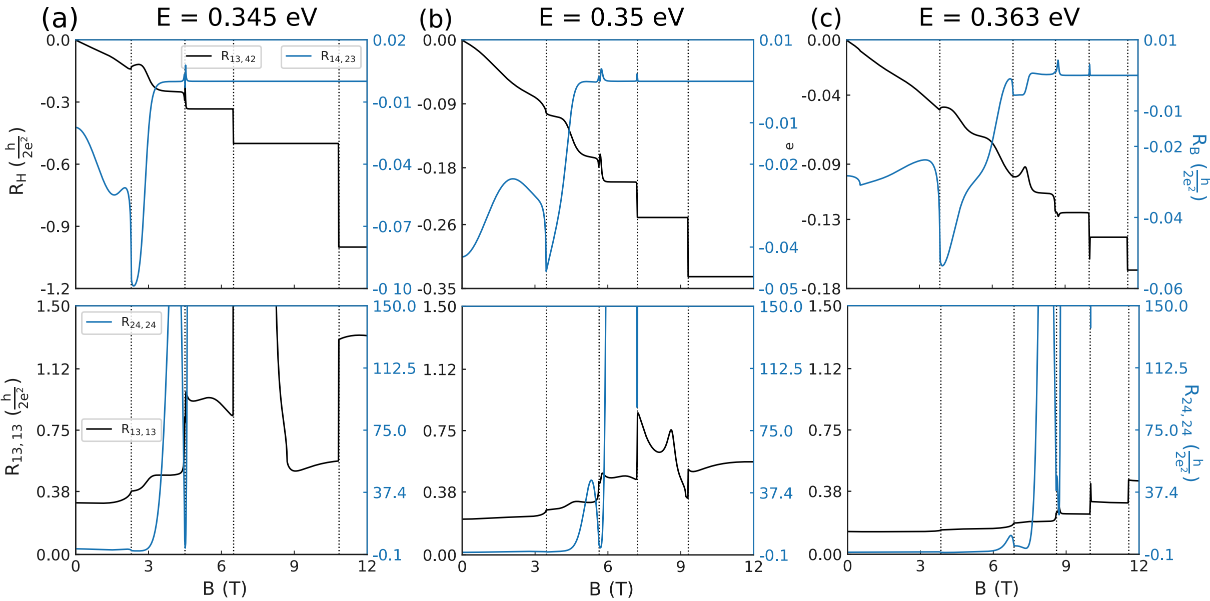

Figure 3.4: Top row: Hall (black), bend (blue), bottom row: longitudinal resistances for a pristine phosphorene Hall bar for $E_F = 0.345$, 0.35 and 0.363 eV. The vertical dashed lines mark the points where the Fermi energy crosses the armchair Landau levels.

As stated before the $R_{24,24}$ is larger than $R_{13,13}$, and they increase with different rates as the magnetic field increases. Figure 3.4 also show that for strong magnetic fields, the bend resistances go to zero while $R_{24,24}$ takes larger values. Another peculiar behavior for $R_{13,13}$ is noticed when the Fermi energies 0.345 eV and 0.35 eV cross the zigzag transverse mode (respectively at $\sim 8.0T$ and $\sim 8.60T$). When that happens, a peak appears in $R_{13,13}$.

To understand the appearance of these peaks, Fig. 3.5 shows the magnetic-field dependency of the different transmissions probabilities between the leads for $E_F = 0.345$ eV. An expected behavior is the decrease of T_{ij} between two counterclockwise terminals as the magnetic field increases. The transmission between the two armchair terminals suddenly increases as the transmission with the next counterclockwise zigzag transmission decreases. This behavior is an indication of the induced transport-mode scattering by the

zigzag terminals. Also, the reflection probability of the zigzag transport modes increase with magnetic field.

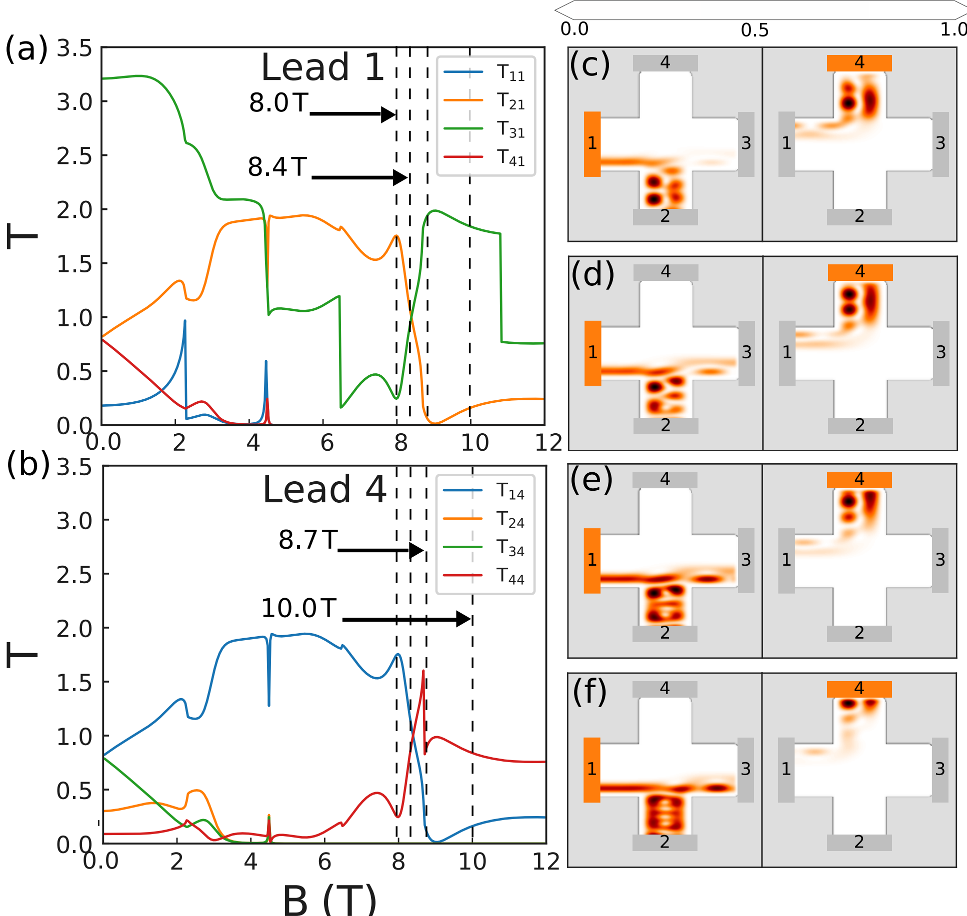

Figure 3.5: The transmission probability from the leads 1 (a) and 4 (b) to the other leads. The local current density is calculated for specific magnetic fields 8.0, 8.4, 8.7 and 10.0 T, respectively (c), (d), (e) and (f). Density values were normalized. The Fermi energy is $E_F = 0.345$ eV.

3.4 Effect of vacancies

Figure 3.6 shows the DOS for a phosphorene Hall bar with SVs and DVs type I and II (see Sec. 3.2). To get reasonable statistics the DOS was averaged over ten samples where the vacancies are randomly distributed. The number of vacancies is related to the quantity n_x, which is defined as the ratio between the atoms removed from the lattice and the total number of atoms. The peaks shown in Fig. 3.6 for the SV and DV2 systems are due to in-gap states. The intensity of the DOS is proportional to the number of defects (YUAN *et al.*, 2015; LIU *et al.*, 2014).

Although there are no transport modes inside the gap, the in-gap defect states can

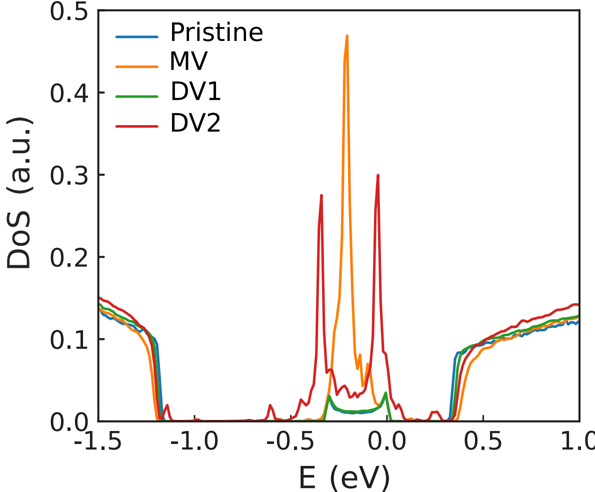

Figure 3.6: DOS of the phosphorene Hall bar for pristine and for three types of disorder with $n_x = 1\%$.

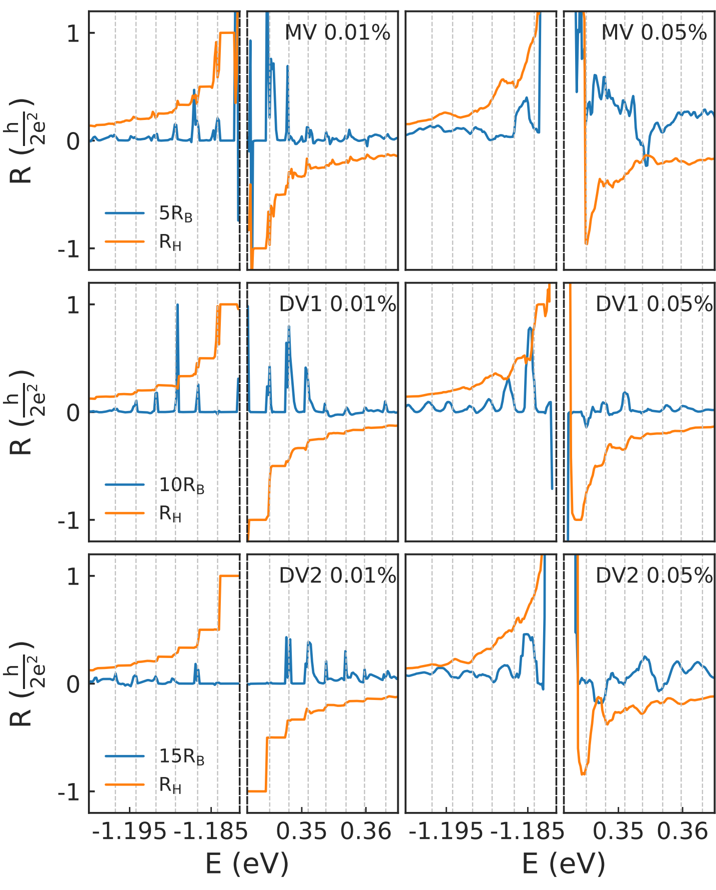

Figure 3.7: Hall and bend resistances for the phosphorene Hall bar with different densities of vacancies for $B = 10$ T. The bend resistances were multiplied by a defined factor to increase its visibility. The grey vertical lines mark the place where the Fermi energy crosses an armchair transverse mode.

affect the system's conductivity via vacancy scattering (LI; PEETERS, 2018; AMINI *et al.*, 2019). This is shown in Figs. 3.7, where the Hall and bend resistances are plotted against the Fermi energy for two different values of vacancy density with an applied magnetic field $B = 10$ T. Each resistance was obtained as an average $R = \sum_i^N R_i/N$, for $N = 10$ random samples[1,2]. For $n_x = 0.01\%$, we can still see the presence of plateaus in the Hall resistance, but it vanishes for $n_x = 0.05\%$ due to scattering.

Another interesting result is the presence of well-defined peaks in the bend resistance, peaks that were not present in the pristine case (see Fig. 3.4). This indicates that already for small vacancy density the system is in the diffusive regime. These peaks, unlike in the case in graphene (PETROVIĆ; PEETERS, 2016), are not due to localization states. They occur when the Fermi energy cross an armchair transverse mode and are related to the increase of diffusion due to the vacancy scattering. Also, this effect is more evident for SV disorder, as for the same vacancy density the SV are more spread in the system than DV1 and DV2.

The DV1 does not create in-gap defect states and the resistances change slightly when compared with the pristine case. This behavior becomes more evident in Figs. 3.8. The Landau plateaus are more resilient in DV1 and the range of the bend resistance is of the same order of magnitude as in the pristine case, while for SV and DV2 the bend resistances are higher. Further, one can see that the presence of the defects with broken symmetry actually suppress the scattering effect provoked by the zigzag transport modes.

Analyzing Fig. 3.9, one notices that the increase in the longitudinal resistance $R_{24,24}$ at ~ 9.3 T is smaller for SV and DV2, and also with the increase of density in DV1. Thus, one can infer that the presence of resonant states reduces the scattering provoked by the zigzag terminals. Apart from these specific effects, the general behavior is that the SV and DV2 enhances the resistances between two axial terminals. This behavior is in agreement with Ref. (SHAH *et al.*, 2019). To better understand this effect we show in Fig. 3.10 the local density of the transport modes for a system with SV, DV1, and DV2 defects for $n_x = 0.01\%$ and 0.05% and magnetic field $B = 10$ T. As the density is increased the modes are scattered to non-axial terminals, which is reflected by the enhancement of the longitudinal resistance.

[1] The Numpy random library was used to generate the random numbers. It returns random floats in the half-open interval [0.0, 1.0), with a "continuous uniform" distribution.

[2] Considering the size of the system, and the density of vacancies considered, 10 samples was enough to reach consistent results with fluctuation.

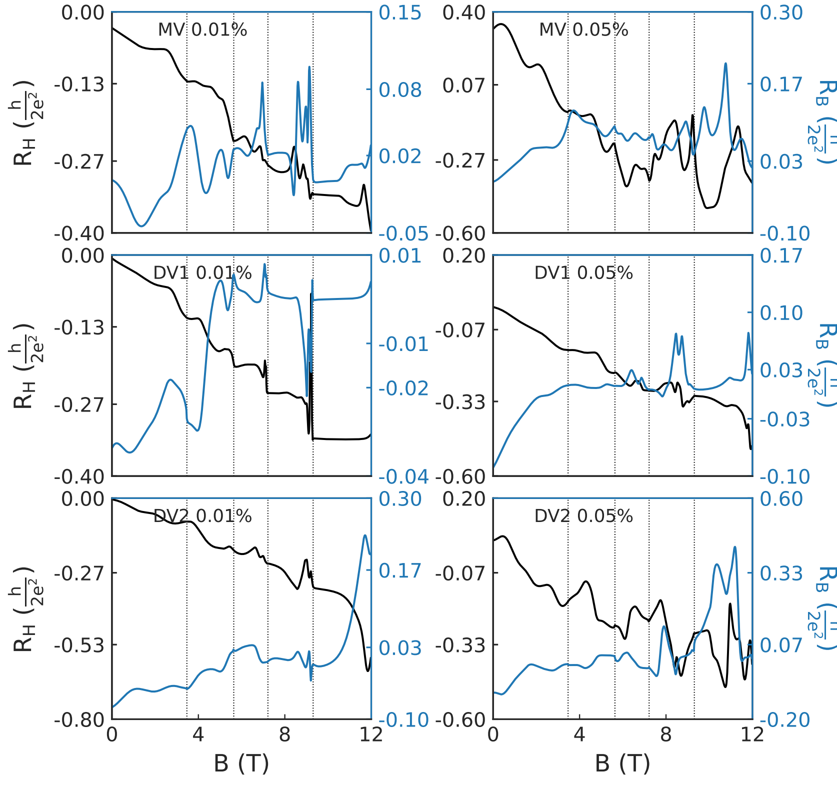

Figure 3.8: The magnetic-field dependency of the Hall and bend resistances for the phosphorene Hall bar with vacancies at fixed Fermi energy $E_F = 0.35$ eV.

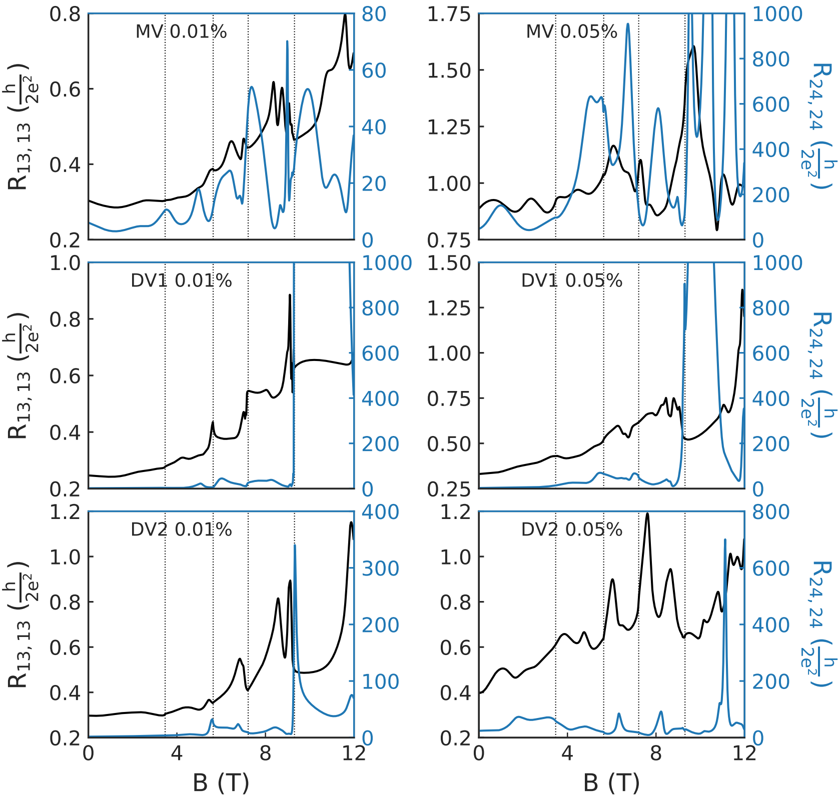

Figure 3.9: The magnetic-field dependency of the longitudinal resistance for the phosphorene Hall bar with vacancies at fixed Fermi energy $E_F = 0.35$ eV.

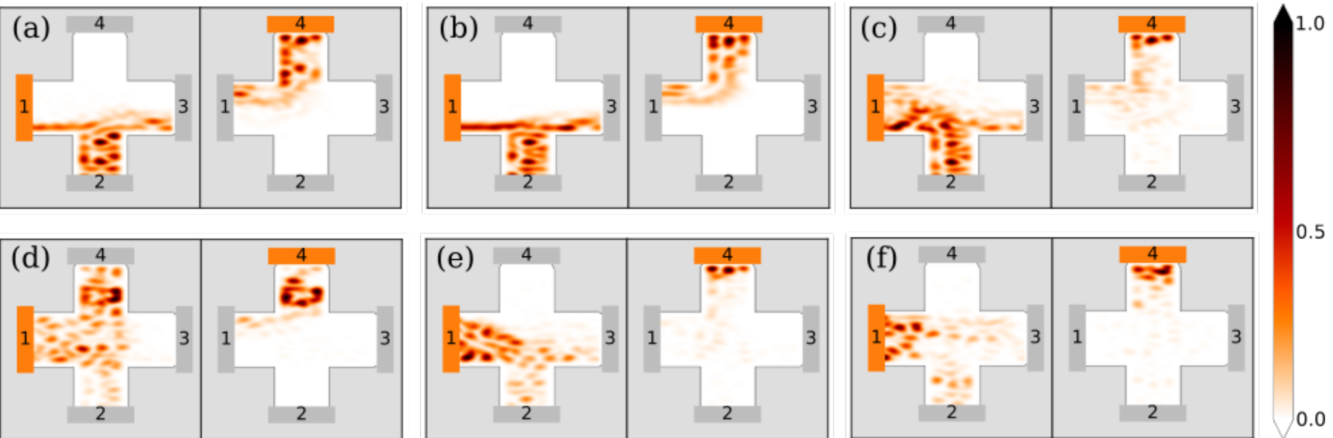

Figure 3.10: Current density for the phosphorene Hall bar with vacancy defects SV(a), DV1(b), and DV2(c) for $n_x = 0.01\%$ and SV(d), DV1(e) and DV2(f) for $n_x = 0.05\%$. We fixed $E_F = 0.35$ eV and $B = 10$ T.

3.5 Conclusions

In summary we analyzed the electrical transport properties of a phosphorene Hall bar in the presence of a magnetic field and vacancy defects. The presence of axial and non axial terminals, with different characteristics, allowed us to study different transport properties of phosphorene material (SHAH *et al.*, 2019; OSTAHIE; ALDEA, 2016) (in this case, the Hall and longitudinal resistances). In Sec. 3.3, we studied the pristine system where a ballistic regime was identified by the bend resistance to certain regimes of Fermi energy and magnetic field, and Landau plateaus show up in the Hall resistance mainly due the semiconductor features of the armchair terminals (ZHOU *et al.*, 2014; SHAH *et al.*, 2019). This can be seen for magnetoresistance for $E_F = 0.363$ eV which matches a zigzag transport mode (see Fig. 3.3-(a)) and shows no Landau plateaus for the Hall resistance (see Fig. 3.4). Also, as stated in Ref. (SHAH *et al.*, 2019), the presence of zigzag transport modes provokes scattering of the transport modes, resulting in a larger peak in the resistance as the Fermi energy crosses the zigzag Landau level, see Fig. 3.5.

The presence of vacancies changes the magneto transport properties, depending on the sublattice symmetry and on the vacancy density, as shown in Sec. 3.4. The effects on the resistance are most noticeable for vacancy types with broken sublattice symmetry, with the SV being the one that most affects the resistance. Although DV1 does not create in-gap states (as shown in Fig. 3.6) the defects still affect the phosphorene transport properties. When analyzing the magnetoresistance, a change in the sign of the bend resistance appears, which indicates a diffusive regime induced by scattering from the defects. The present paper clearly indicates the much richer transport features that can be observed in phosphorene as compared to graphene. The anisotropy of the phosphorene lattice and the presence of a gap are responsible for the increased complexity of its electrical response.

4 VACANCY CLUSTERING EFFECT ON THE ELECTRONIC AND TRANSPORT PROPERTIES OF BILAYER GRAPHENE NANORIBBONS

4.1 Introduction

Transition from a BLG to a MLG nanoribbon is studied by analysing the presence of zero modes in the density of states due to point defects. To mimic the lack of control in the position of vacancies, one focuses here on the effects of randomly distributed vacancies in the electronic structure of BLG nanoribbons with armchair and zigzag orientations, which allows the formation of vacancy clustering. The number of states at $E = 0$ eV grows with the number of vacancies and we show that by removing atoms from only one of the layers there is a maximum density of states at $E = 0$ eV followed by a decrease on its value until the MLG behaviour is recovered. Both AA and AB BLG stacks will be investigated for nanoribbons with different sizes and edges. Our electronic and transport results for the energy spectrum, density of states (DoS), resistance, and current density for different vacancy concentration are obtained by using the first nearest neighbour hoppings tight-binding (TB) model, and the latter by using the Landauer–Büttiker formalism.

4.1.1 Defects in BLG

In TB model, vacancies are implemented by removing atom sites and its connections with neighbouring atoms, making hoppings to the vacancy sites forbidden. There are different types of vacancies defects based on the sublattice symmetry and the number of removed neighbors sites(VUONG *et al.*, 2017; PEREIRA *et al.*, 2008). They are named single (SV), double, triple, and so on, vacancy disorders accounting for the number of removed carbon atoms. Related to the imbalance of sublattice atoms, either multiples SVs can be removed without any respect to the sublattice type or all of SVs belonging the same sublattice (e.g. from sublattice A (SVA) and from B (SVB)). The presence of a SV breaks the sublattice symmetry, whereas it can be recovered by a double SV composed by one SVA and one SVB, as well as in double vacancy disorder.(PETROVIĆ; PEETERS, 2016; LEE *et al.*, 2005; PALACIOS *et al.*, 2008; HAHN; KANG, 1999; EL-BARBARY *et al.*, 2003a; OVDAT *et al.*, 2020) Ref. [Petrović e Peeters (2016)] demonstrated an interesting feature related to different behaviors of these two single vacancy distribution types. They reported that a random vacancy distribution (i.e. only SVA or only SVB disorders), although inducing an approximately equal number of states as SV disorder for low vacancy

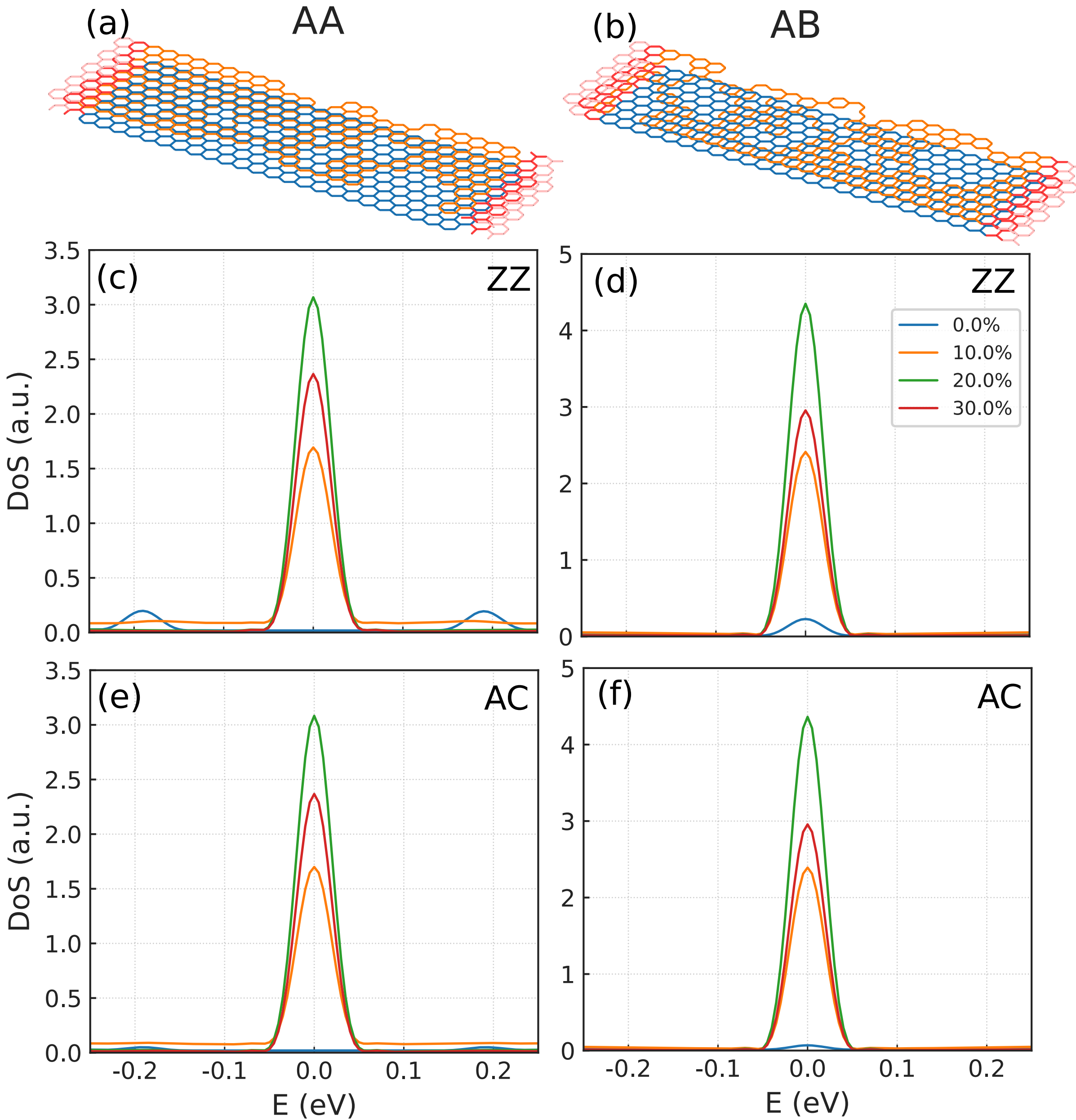

Figure 4.1: Schematic illustration of (a) AA- and (b) AB-stacked BLG nanoribbons. Carbon atoms are removed from the top layer (orange). Two ballistic leads (red) are attached to the extremities at the two layers, being used to calculate the conductivity and resistance. (c-f) DoS of the scattering region that defines BLG nanoribbons around the Fermi energy for (left panels) AA- and (right panels) AB-stacked BLG nanoribbons for pristine (blue curve) and defective systems are presented for (c, d) zigzag and (e, f) armchair nanoribbons. Different vacancy densities are taken: 10% (yellow curve), 20% (green curve), and 30% (red curve).

concentration, creates considerably different results in the bend resistance. Moreover, the experimental verification of the vacancy type and impurities (dopants or adatom) in BLG system can be achieved by scanning tunnelling microscopy and spectroscopy measurements, as for instance as reported in Refs. [Kaladzhyan *et al.* (2021a), Kaladzhyan *et al.* (2021b), Joucken *et al.* (2021b), Joucken *et al.* (2021a)]. In particular, Refs. [Joucken *et al.* (2021b)] and [Joucken *et al.* (2021a)] have experimentally shown, by using atomic-scale resolution with scanning tunneling microscopy and spectroscopy, the consequences of points defects on the BLG spectrum with a real space characterization.

Here, we focus only on ordinary SVs, being created by randomly removing a single site from one of the layers of the system, regardless its sublattice. In this work every analysis was averaged for 20 samples. Through error analysis (see Fig. 4.2) analysis it was shown that 20 samples was enough to archive small error fluctuation. In the case of MLG, this randomly carbon atoms removal should preserve the sublattice symmetry on average.(PETROVIĆ; PEETERS, 2016) The investigated defective BLG nanoribbons are here characterized by the vacancy concentration N with respect to the total number of carbon atoms in the scattering region. The higher the value of N, the larger vacancy clusters can be formed and more edge defects are expected, leading to imperfect edges formed by not just one type of edge, but rather a mix of zigzag and armchair ones. An additional degree of freedom in creating vacancies in bilayer systems is associated with the location of the defect per layer, with the possibility to be created in only one of the layers or in both layers.(XU *et al.*, 2009; KISHIMOTO; OKADA, 2016; LEE *et al.*, 2005; XU *et al.*, 2009; TELLING *et al.*, 2003; VUONG *et al.*, 2017; ANINDYA *et al.*, 2020; MAPASHA *et al.*, 2019; SAFARI *et al.*, 2017; PALACIOS; YNDURÁIN, 2012) In order to investigate the coalescence due to the transition between

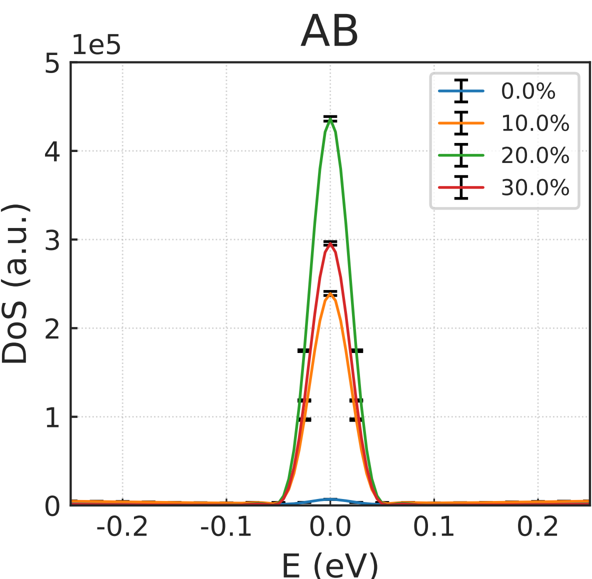

Figure 4.2: Error bar analysis for the system shown in Fig. 4.1. As we can see the error bar (standard deviation) is considerable small, indicating small error fluctuation.

BLG and MLG nanoribbons by increasing the vacancy concentration, the electronic and transport properties are studied here by considering multiple randomly distributed SV implemented only on the top-layer, as sketched in Figs. 4.1(a) and 4.1(b) for AA-stacked and AB-stacked disordered zigzag BLG nanoribbons, respectively. The sublattice symmetry and inversion symmetry aspects in the investigated BLG nanoribbons shall be very important in understanding the transport results further on here (see discussion in Sec. 4.3). The examples in Figs. 4.1(a) and 4.1(b) have a vacancy concentration of $N = 10\%$. It is important to highlight that the system considered is formed by a scattering (finite system) region that defines the BLG nanoribbon with sample dimension $L \times W$, and consequently small peaks in the DoS associated with the energy states beyond $E = 0$ are not present and, in addition, are not relevant for the electronic aspects investigated here around the Fermi energy. This finite region is generated using KWANT's subroutines(GROTH *et al.*, 2014) by populating a rectangular shaped region (for a specific size) following the BLG unit cell and then the vacancies in a certain concentration are randomly created. However, for a distance $d_r = a_x = 0.24595$ nm (with a_x being the unit cell size in the x-direction) close to the leads, the atoms are not removed. This restriction is set so it will be possible to attach the leads for the transmission calculation. Moreover, the scattering region that defines the BLG nanoribbon is characterized by its width W and then we assumed its length as $L = 3W$, such that the total disordered area is $A = L \cdot W = 3W^2$. This assumption is chosen in order (i) to systematically investigate different vacancy densities associated with the removal large of a number of carbon of atoms and easily compare the results for the different studied situations (edges and stacking); (ii) to deal with BLG nanoribbons dimensions feasible to be experimentally realized; and (iii) to avoid low conductance (high resistance) values due to geometric aspects, such as the small dimensions of the scattering channel, and also skipping-orbit-like trajectories in the density currents in narrow BLG nanoribbons, which could lead to a misunderstanding of the transport properties regarding the presence of vacancies in the system. It is worth mentioning that changes in L size of the scattering region to a fixed width W do not change the nanoribbon band structure since the length L is along the translation symmetry direction, and consequently, one expects not to affect the transport results for the vacancy-free case within the ballistic transport regime.

4.2 Zero-modes density

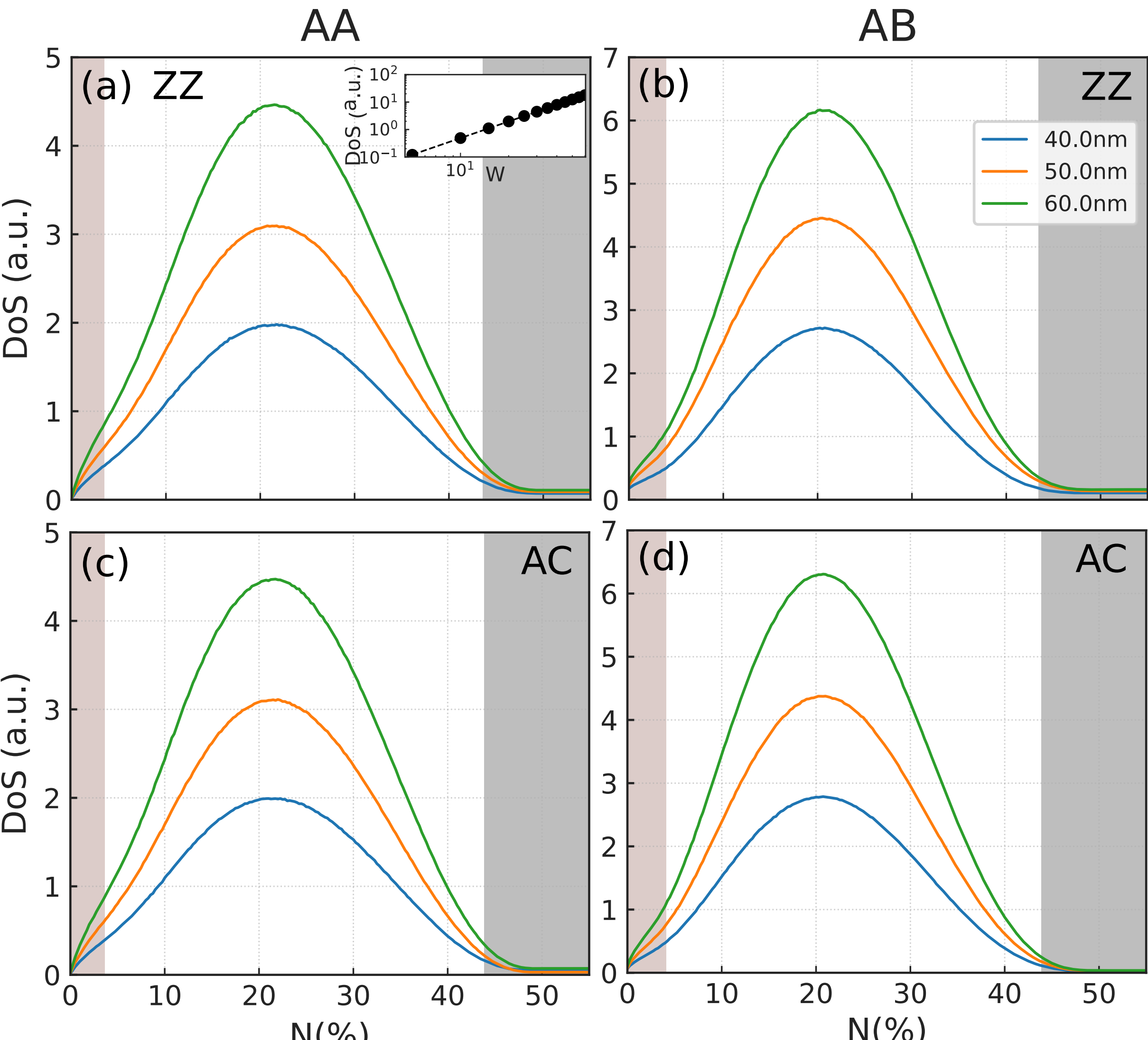

Figure 4.3: DoS at $E = 0$ of the scattering region that defines BLG nanoribbons as a function of the vacancies density N for three different ribbon widths (W): (blue) 40 nm, (yellow) 50 nm, and (green) 60 nm, where the ribbon length is defined as $L = 3W$. The total disordered area changes as $A = L \cdot W = 3W^2$. Left (right) panels correspond to AA- (AB-)stacked BLG nanoribbons with (top panels) zigzag and (bottom panels) armchair edges. Each density configuration was averaged by taking twenty samples. Only a small deviation is observed in comparison to the present average curves, that is caused by the random character of the disordered introduction into the BLG system. For a better visualization of the Gaussian-like DoS profile, we omitted here the error bars. The inset in panel (a) shows a linear fit in log-scale for the centered DoS peak ($\equiv 21\%$) for different zigzag AA-stacked nanoribbon widths W. Its slope is 2.012.

Let us now investigate the effects of vacancies on the DoS of the scattering region that defines the BLG nanoribbons. Figures 4.1(c)-4.1(f) show the DoS for (c, e) AA- and (d, f) AB-stacked BLG nanoribbons with (c, d) zigzag and (e, f) armchair edges.

Analyzing the pristine AA-stacked case ($N = 0\%$, blue curve), one finds two peaks around $E = \pm\gamma_1^{AA}$ which are related to the interlayer hoppings, being more pronounced for zigzag case [Fig. 4.1(c)] due to the degeneracy of the edge states, as shown by the flat states in Fig. 2.10(c), while for armchair AA-stacked BLG nanoribbons [Fig. 4.1(e)] they are less evident but non-zero being linked to the corners of the shifted Dirac cones in AA-BLG spectrum. For AB-stacking, one notices a peak at the Fermi energy ($E = 0$), which is related to the edge states present in the zigzag nanoribbon, as depicted by the flat band at $E = 0$ in Fig. 2.10(e). For armchair BLG nanoribbons with AB-stacking, the presence or the absence of a central peak at $E = 0$ depends on the ribbon width, since it dictates the semiconductor or metallic nature of the ribbon. For the chosen ribbon width, as already discussed for Fig. 2.10(f), this BLG nanoribbon is metallic, exhibiting, in turn, a less pronounced peak in its DoS [Fig. 4.1(f)] in comparison to the zigzag case [Fig. 4.1(d)], that is due to the low degeneracy coming from the conduction-valence band-touching. Results of the DoS at $E = 0$ for semiconductor BLG nanoribbons with armchair edges would present a less pronounced peak but qualitatively similar results to the obtained metallic ones.

The presence of vacancies induces scattering states that are identified by DoS showing a peak at $E = 0$, whose surface area is proportional to the vacancies density (PEREIRA *et al.*, 2008). For low vacancy densities, it is expected that zero-modes degeneracy increases and, consequently, the magnitude of the peak at $E = 0$, as observed for $N = 10\%$ (yellow curve) and $N = 20\%$ (green curve) in Figs. 4.1(c)-4.1(f). However, for high vacancy concentration the $E = 0 -$ DoS peak decreases, as one can see in red curves for $N = 30\%$, where the peak at $E = 0$ for 30% vacancy density is smaller than for 20% for both types of stackings and edges. This behaviour of the DoS at $E = 0$ suggests us the existence of a threshold value for the vacancy concentration, where after this up limit the peak of the DoS decreases. For MLG, most of the studies have been focused on vacancy densities below the percolation threshold ($\lesssim 30\%$) (HÄFNER *et al.*, 2014).

In order to investigate the universality of the DoS tendency at $E = 0$ for BLG nanoribbons and its link with the coalescence by removing carbon atoms from the top layer of the BLG system into the MLG one, we show in Fig. 4.3 the DoS value at $E = 0$ varying with the vacancies densities. Results for AA-(AB-)stacked BLG nanoribbons are shown in Figs. 4.3(a, c) [Figs. 4.3(b, d)] by taking BLG nanoribbons with different widths and

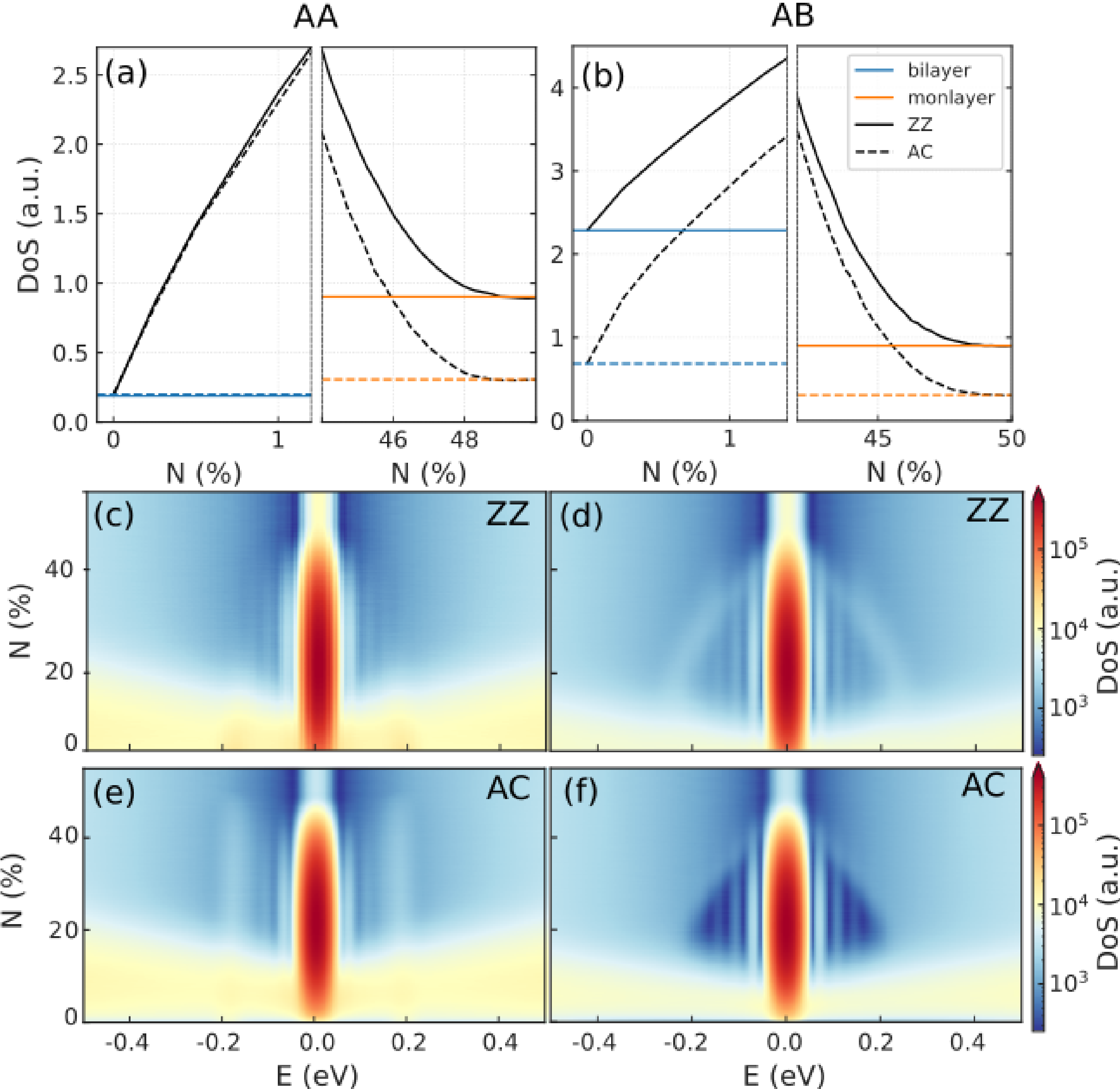

Figure 4.4: (a, b) Enlargements of Fig. 4.3 at low (left) and high (right) vacancy densities for (a) AA-stacked and (b) AB-stacked BLG nanoribbons with ribbon width of 50 nm to emphasize the BLG to MLG transition due to vacancy density increasing. Blue and orange curves are the BLG and MLG DoS values for the pristine cases and the different line types indicate the type of edge orientations. Solid and dashed curves correspond to the pristine DoS values for zigzag and armchair BLG nanoribbons. (c)-(f) Contour plots of the DoS in log scale on the energy-vacancy density plane (E, N) for AA (left panels) and AB (right panels) stacking with nanoribbons formed by (c, d) zigzag and (e, f) armchair edges.

edge types: zigzag (Figs. 4.3(a, d)) and armchair (Figs. 4.3(c, d)). Surprisingly, regardless the edge type and the BLG stacking, the evolution of the number of zero-modes in the DoS by increasing the vacancy density for all investigated configurations demonstrates the existence of a saturation point (i.e. an amorphization threshold) observed at $N \approx 21\%$, with a width-independent behavior that resembles a "Gaussian-like" function. To numerically check this result we fit the curves in Fig. 4.3 with a Gaussian function, defined as $f \equiv DoS(N) = a \exp\left[-(N-b)^2/c\right]$, where a gives insights about the scaling phenomena properties related to the Gaussian function amplitude, b is related to Gaussian distribution's mean point, i.e. the center position of the peak, and c is the standard deviation. The fitting parameters are depicted in Table 4.1. Analyzing b–values in Table 4.1, one notes that, in fact, all curves are approximately centered around $\approx 21\%$, and that the a–values show the scalable behavior of the $E = 0$ – DoS with the nanoribbon size, increasing the larger the BLG nanoribbon. This is demonstrated in the inset of Fig. 4.3(a) with a power-law scaling with a linear fit with slope of ≈ 2.012. After the threshold value $N \approx 21\%$, the DoS for all curves in Fig. 4.3 decreases until they reach a fixed value corresponding to the DoS of the MLG system. The recovered MLG value is achieved to a vacancy concentration around $\approx 50\%$. This can be seen in Figs. 4.4(a) and 4.4(b) where enlargements of Fig. 4.3 (shaded regions) for low (left panels) and high (right panels) vacancy densities for AA-BLG and AB-BLG, respectively, are shown, emphasizing the transition from pristine BLG nanoribbon to pristine MLG nanoribbon by varying the vacancy density. Dashed and solid curves correspond to armchair and zigzag cases, and blue and orange curves are, respectively, the DoS value for pristine BLG and pristine MLG system.

Table 4.1: Parameters of the Gaussian-like function fitting, $f \equiv DoS(N) = a \exp\left[-(N-b)^2/c\right]$, for the DoS curves of Fig. 4.3.

width		AA-ZZ	AA-AC	AB-ZZ	AB-AC
40 nm	a	2.02	2.04	2.75	2.84
	b	21.98	21.9	20.98	21.07
	c	221.3	215.44	189.05	183.58
50 nm	a	3.16	3.18	4.52	4.47
	b	21.94	21.86	20.99	21.10
	c	217.93	212.58	191.78	183.73
60 nm	a	4.56	4.58	6.27	6.44
	b	21.97	21.91	21.06	21.1
	c	217.55	214.47	186.13	183.59

Owing to verify if such width-, stacking-, and boundary-independent behavior observed in Fig. 4.3 for the DoS at $E = 0$ holds true for different energies of the investigated BLG nanoribbons, we show in Figs. 4.4(c)-4.4(f) contour plots of the DoS in the (E, N)–plane. For a short energy range around $E = 0$, the DoS exhibits a similar behavior as the one discussed for $E = 0$ in Fig. 4.3 and reaches its higher value (red color) also around $N \approx 21\%$. This is not the case for higher energies that goes to low values (blue color) as N increases, as it should be, since the increase in the number of vacancies mainly affects the degeneracy of the zero-mode states.

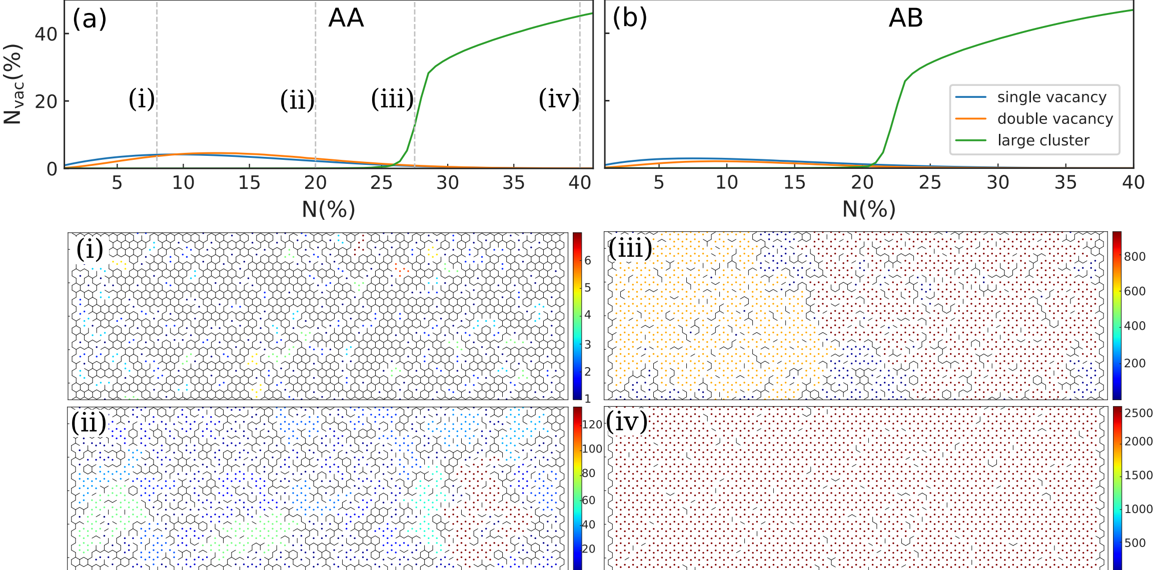

Figure 4.5: Vacancy clustering analysis for (a) AA- and (b) AB-stacked BLG nanoribbons with ribbon size 150 nm × 50 nm. Results for single, double, and large clusters of vacancies proportional to the total number of vacancies are shown in blue, yellow, and green. Colored scatter-like plot of the spatial clustering for the systems with vacancies densities at 8%, 20%, 27.5% and 40%, as indicated by the vertical lines in (a), are depicted in the bottom panels (i), (ii), (iii) and (iv), respectively. Each density configuration was averaged by taking five samples.

To attain a more comprehensive understanding of the Gaussian-like DoS behavior for the electronic states around $E = 0$, we explored the cluster formation and the ratio of single and double vacancies randomly distributed in the top layer of BLG nanoribbons due to the increase of vacancy density N. Without loss of generality, the results for SV (blue curve), double vacancy (yellow curve), and large clusters (green curve) are shown in Fig. 4.5 just for zigzag AA-stacked (Fig. 4.5(a)) and AB-stacked (Fig. 4.5(b)) BLG nanoribbons. We considered that two vacancies belong to the same cluster if they are inside a circle of radius r_c. We choose $r_c = a_x = 0.2459$ nm, which is the unit cell size

in the x-direction. Figures 4.5(a) and 4.5(b) show that for low vacancy densities (bellow to the observed threshold value, i.e. $N \lessapprox 21\%$) the disordered BLG system is mainly dominated by single and double vacancies. This is confirmed by the spatial clustering analysis depicted in panel (i) for $N = 8\%$ at the bottom of Fig. 4.5. For higher vacancy densities, the vacancies coalesce and the ratio of single and double vacancies starts to decrease. The formation of the large clusters can be viewed in panel (ii) for $N = 20\%$, in which the spatial clustering analysis exhibits clusters with sizes in the order of ≈ 40 to ≈ 80 removed sites. By increasing even more the dilution on the system's top layer, the N_{vac} percentage of single and double vacancies tends to zero and a sudden growth of the clusters sizes is observed. Interestingly, this happens approximately around the threshold value found in the DoS plots for energies around $E = 0$. The spatial distributions of the vacancies shown in panels (iii) and (iv) for $N = 27.5\%$ and $N = 40\%$, respectively, confirm this statement. As discussed so far for the AA-BLG case, a similar clustering analysis is observed for disordered AB-stacked BLG nanoribbons, with the difference that the structural transition of the vacancy clustering happens for a slightly smaller vacancy density, as noticed in Fig. 4.5(b).

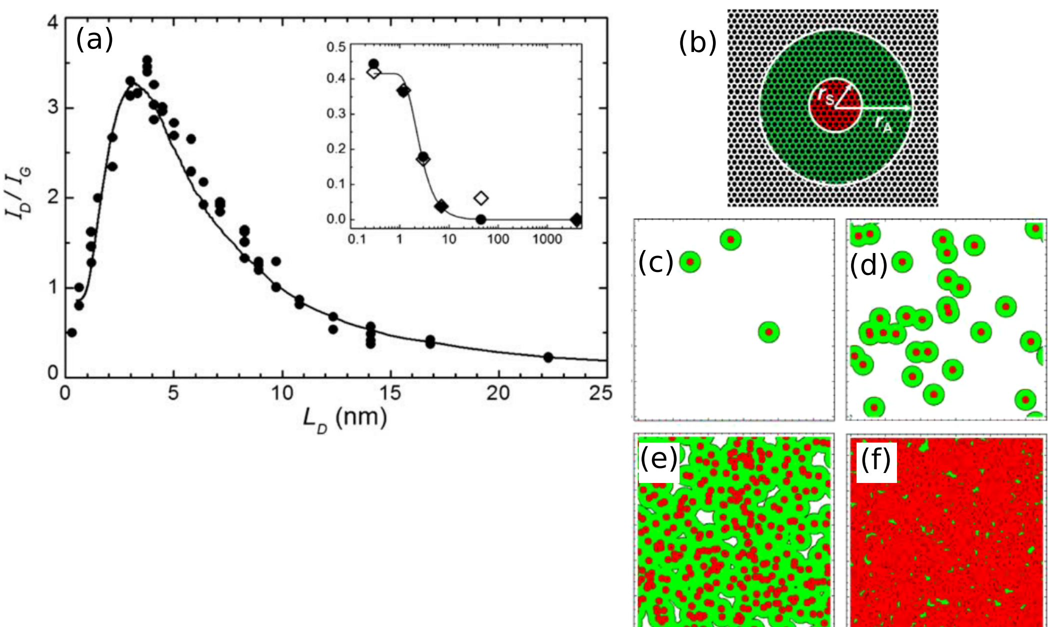

Figure 4.6: (a) The ratio I_D/I_G as funciton of the average distance L_D between defects, induced by ion bombardment in mono-layer graphene. (b) shows the definition of the "actived" (green circle) and the "structurally-disordered" (red circle) regions. (b-e) represents a simulation on how those regions start to coaleses as the the number of defects grows. Figure adapted from *Carbon* 48 (2010) 1592-1597.

A similar analysis of the structural formation of vacancy clusters was performed in

Ref. [Lucchese *et al.* (2010)]. By Raman Spectroscopy measurements, they showed that the I_D/I_G ratio demonstrated a saturation point where two disorder mechanisms started to compete between themselves (see Fig. 4.6(a)). These disorder mechanisms are related with the "activated" and "structurally-disordered" regions. The structurally-disordered is the structural disorder that occur from the impact with a radius r_s. In a radius larger than r_s, but shorter than r_a, the lattice structure is preserved but thereis a mixing of the Bloch states near the K and $K^{'}$ of graphene Brillouin zone, causing break of selection rules and leading to an enhancement of the D band. This region inside r_a is the activated region. They stated that this competing mechanism is attributed to the coalescence of these two regions and it is followed by a full amorphization or partial sputtering of the graphene layer.

Regarding the skewed interlayer hoppings, it is known that the incorporation of γ_3 leads to the emergence of three-fold mini-valleys around K and K' Dirac cones and consequently to anisotropic low-energy bands for the infinite pristine BLG sheet. Thus, one can easily see that this must lead to an increase in the degeneracy of the DoS at $E = 0$, even in the absence of vacancies, for both the infinite pristine BLG sheet and BLG nanoribbons cases, where in the later one also expects to verify a broadening of the DoS($E = 0$)-peak due to the breaking of the degeneracy of the bands, especially for the zigzag BLG nanoribbons where its quasi-flat states become more dispersive by assuming $\gamma_3 \neq 0$.(KNOTHE; FAL'KO, 2018) Therefore, the obtained DoS($E = 0$) results discussed here are expected to be qualitatively similar if one takes into account $\gamma_3 \neq 0$, except for an increase in the peak magnitude of DoS($E = 0$).

4.3 Electronic transport

In order to have a connection between the DoS behavior and experimental measurements on the electronic transport properties of the system studied here, we calculate the two-terminal resistance, for both the AA and AB-stacked BLG nanoribbons, as function of the vacancy density. The results are shown in Fig. 4.7 in a semi-log scale with the resistance for energies varying from 0.0 (dark blue color) to 0.2 eV (dark red color). Although the DoS behavior shown in Fig. 4.3 is basically independent of the stacking and the ribbon orientation, the vacancies affect the transport properties in different ways, depending on the ratio of the number of clusters and their sizes with respect to the system size that can

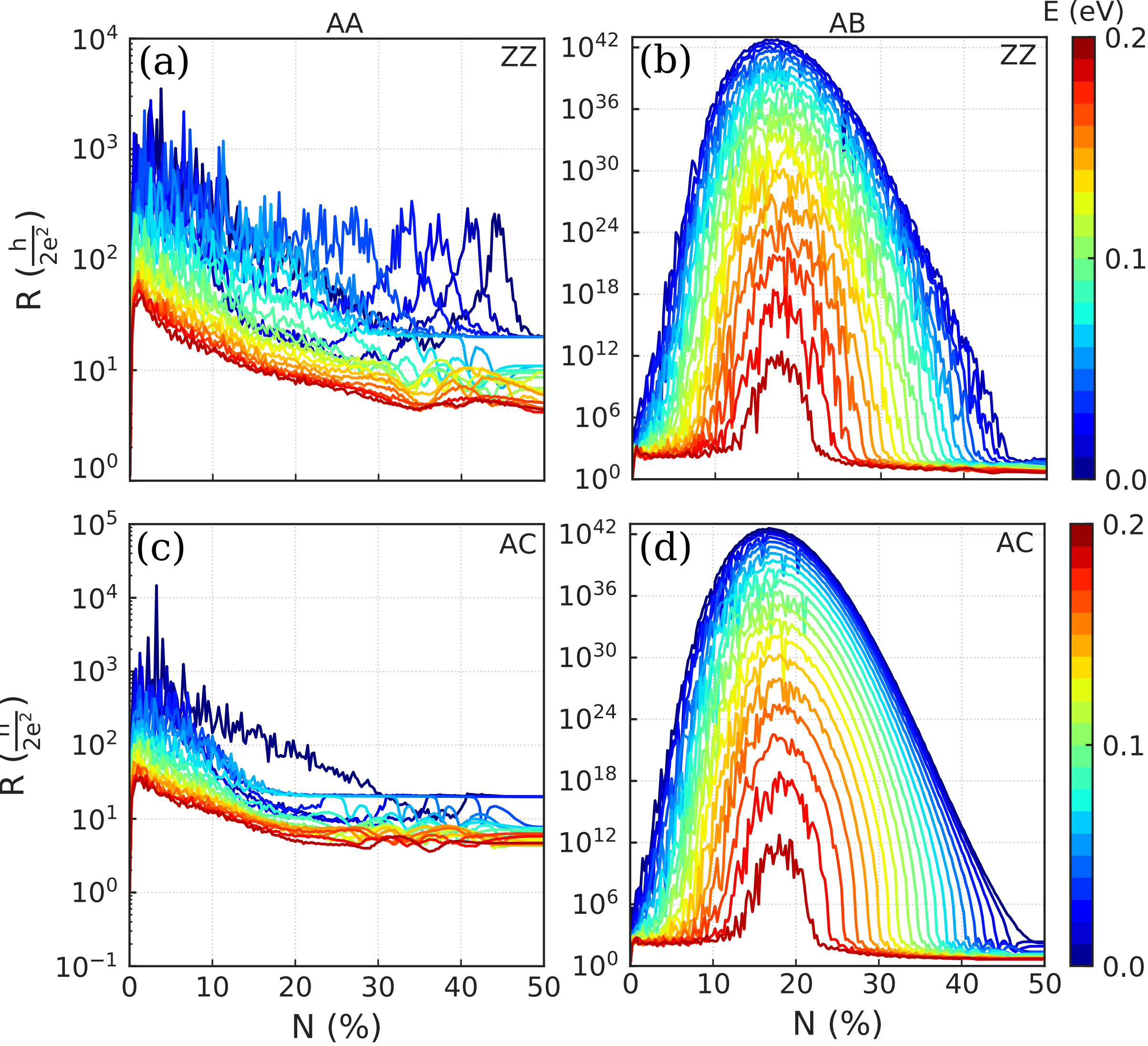

Figure 4.7: Resistance as a function of the vacancies density N for (top panels) zigzag and (bottom panels) armchair (left panels) AA-stacked and (right panels) AB-stacked BLG nanoribbons for different Fermi energies. Blue (red) color corresponds to low (high) Fermi energy. Each density configuration was averaged by taking twenty samples.

lead to variations on the characteristic transport lengths (e.g. phase relaxation length and mean free-path) and, consequently, causing transport regimes changes.(DATTA, 1997) For the AB stacking (right panels in Fig. 4.7), there is a rapid increase in the resistance with the number of vacancies, until a maximum is reached (close to N $\approx$ 17%), in an approximately similar way as the observed Gaussian-like DoS profile discussed in previous section. After that, the resistance decreases and reaches a fixed value. By comparing Figs. 4.7(b) and 4.7(d) for zigzag and armchair AB-stacked BLG nanoribbons, respectively, one notices a resistance independence on the edge orientation. Previous works reported similar Gaussian-like function characteristics in transport properties of AB-stacked BLG systems.(RATHI *et al.*, 2018; YU; DUAN, 2013) For instance, Yu and Duan(YU; DUAN, 2013) demonstrated that the on/off current ratio of AB-stacked BLG nanoribbons can be systematically increased upon applying a vertical electric field, which breaks the inversion symmetry, observing a Gaussian-like resistance modulation via applied perpendicular bias. For AA stacking, the results differs a lot from the AB case, even though the DoS are the same. Note that in the disordered investigated system here, we have the following situations: (i) for AA-stacked BLG nanoribbons, where both layers are exactly stacked on top of each other, the presence of a high concentration of randomly distributed multiple SVs in one of the layers does not break the sublattice symmetry on average in that layer(PETROVIĆ; PEETERS, 2016) and therefore, the inversion symmetry of the system is kept, since the removed interlayer hoppings correspond to the same sublattices on both layers; (ii) for AB-stacked BLG nanoribbons, although the sublattice symmetry is preserved on the disordered top layer, the inversion symmetry is broken in this case, since the removed interlayer connections link sublattices from different types in AB-BLG systems. This is the reason why resistances for both types of stacking and for very low densities ($N < 1\%$) exhibit roughly the same behavior (as will become clear and confirmed later in the discussion for the current densities in first column of Fig. 4.8), whereas for high vacancy densities the resistance behavior for AA and AB cases is drastically different due to the inversion symmetry to be preserved or broken in the system. Similarly to Ref. [Yu e Duan (2013)], the resistance is strongly modulated by the breaking of the inversion symmetry of the AB-stacked BLG system, exhibiting a Gaussian-like profile. In addition, it is worth mentioning that the noised results for the resistance calculated here at $T = 0$ will be smoothed for non-zero temperatures, but one expects that the main features in

Fig. 4.7 remain almost "intact" for non-zero temperatures.

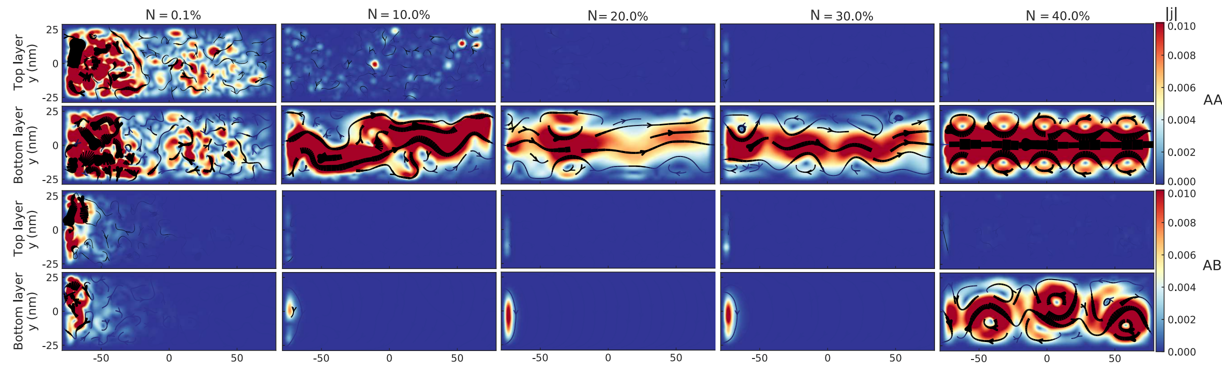

Figure 4.8: Current densities for different vacancy concentrations N for zigzag (top panels) AA-stacked and (bottom panels) AB-stacked BLG nanoribbons with ribbon size of 150 nm $\times$ 50 nm. Transport modes with energy $E = 0.1$ eV were injected by the left lead and collected in the right lead. Blue (red, black) color corresponds to low (high, very high) densities. Current densities for bottom and top layers are presented separately.

To better understand the resistance results, we analyse in Fig. 4.8 the current density for the same system setups as in Fig. 4.7, i.e. zigzag AA-stacked (top panels in Fig. 4.8) and AB-stacked (bottom panels in Fig. 4.8) BLG nanoribbons. Different vacancy densities were taken: (first column) 0.1%, (second column) 10%, (third column) 20%, (fourth column) 30%, and (fifth column) 40%. Plots for top and bottom layers are shown separately, in order to identify the origin of the decrease or increase of the resistance in Fig. 4.7 via insights into the current density amplitudes by increasing the dilution on the system's top layer. The electronic current is injected into the scattering region through the lead on the left side and collected in the lead on the right side. As expected, for low vacancy densities (see first column for $N = 0.1\%$) the current flows in both layers for both AA and AB stacking cases. By increasing the vacancy density on the top layer (analysing the contour plots from left to right columns), the projection of the current on the top layer is suppressed around threshold N–value for AA-stacked BLG case in accordance with the clustering analysis in Fig. 4.5(a) and with the Gaussian-like DoS profile in Fig. 4.3(a) for zigzag edge type. One can also notice by the current results for AA stacking that the current in the bottom layer is not strongly affected by changes on the vacancy densities presented in the top layer (see second row of contour plots in Fig. 4.8). This explains the reason why the resistance in Figs. 4.7(a) and 4.7(c) for AA-stacked BLG case remains practically constant for each energy value for vacancy concentration larger than the threshold N–value, disregarding the fluctuations that must be minimized

for results with non-zero temperatures. In contrast, for the AB-stacked BLG case with $N > 1\%$, the inversion symmetry broken due to high vacancy densities strongly affects the current, suppressing it in both layers. However, for very high vacancy densities (see fifth column for $N = 40\%$) the current between the two leads is restored for the bottom layer of AB-BLG nanoribbon, resulting in an increase in the conductance and, in turn, a decrease in the resistance, as observed in Figs. 4.7(b) and 4.7(d). The absence of current flow in both layers in the AB-stacked BLG case (third and fourth rows of panels in Fig. 4.8) is in agreement with the large scale of the resistance values, since there are no propagating modes, the conductance is practically null, leading to huge values for the resistance, as seen in Figs. 4.7(b) and 4.7(d), in comparison to the range scale of tens of $k\Omega$ to $M\Omega$ usually observed in experimental measurements in BLG systems for the resistance.(YU; DUAN, 2013) Although counter-intuitive, the removal of intralayer and interlayer hoppings due to the vacancies in the upper layer affects the electronic transport of the lower layer. It was demonstrated(COSTA *et al.*, 2016; MIRZAKHANI *et al.*, 2016) that nanostructures formed by MLG-BLG-MLG interfaces allow the confinement of states in the MLG region and also near the MLG-BLG junction even though the bottom layer of such structures does not present explicit edges the electron can nevertheless be influenced by the upper layer edges due to the interlayer coupling near the MLG-BLG junction. Similarly, one observes in our transport results here the important role of the existence of interlayer connections, which allows scattering between the layers, and the different stacking to avoid non-zero conductance or to suppress propagating states.

4.4 Conclusions

The effects of randomly distributed vacancies and its clustering on the electronic and transport properties of BLG nanoribbons were studied by means of the analysis of the DoS at the charge-neutrality point and the resistance, respectively. The disorder is simulated by subtracting carbon atoms of only one of the layers and clusters formations of point defects are allowed. For low densities of vacancies, the DoS at $E = 0$ eV increases as the number of removed atoms increases, owing the enhancement of the zero energy states degeneracy associated with the states localized around missing carbon atoms. This peak in the DoS has a threshold that is reached for a vacancy concentration value around $N \approx 21\%$. After this value of concentration, the DoS decreases until it approaches to its

MLG value. This behavior showed valid regardless the layer stacking (AA or AB), the ribbon orientation (armchair or zigzag), and the nanoribbon width. This result implies that for $N > 21\%$ the empty spaces left by the vacancies start to coalesce forming larger and larger clusters of vacancies in the specific layer.

Although the DoS behavior is the same regardless the stacking and nanoribbon orientation, the transport characteristic is shown to be quite different depending on the stacking. Defects can change the transport characteristics of the material increasing or reducing its conductivity depending on its concentration. Analyzing the resistances for the two investigated types of edges and stackings, it was observed that both zigzag and armchair AB-stacked BLG nanoribbons exhibit a similar feature found for the DoS with two equivalent concentration disorders giving the same resistance value, showing a direct relation between the effects on the DoS by the vacancies and on the electronic transport. The difference between the AA-BLG and AB-BLG transport results are explained by means of the preservation (breaking) of the inversion symmetry for AA (AB) case at high vacancy density. The results presented here emphasise the richness of the BLG properties when vacancies are introduced into the system.

5 SUMMARY AND PERSPECTIVES

In this thesis we studied how the presence of vacancies defects acts in phosphorene and BLG by analysing its electronic and transmission properties. Atomic defects in 2D materials can largely change the material properties, when compared to its defect free counterpart, by being the source of new and interesting behaviours, or causing degradation, that needs to be predicted and controlled.

Vacancies at the surface of phosphorene are preferential chemiabsorption sites for oxygen, leading to formation of oxygen defects and making the surface of phosphorene hydrophilic, ultimately resulting in the formation of a mixture of oxide and phosphoric acid(CARVALHO *et al.*, 2016), which can be avoided by encapsulating the material with a inert material(YOON; LEE, 2017; CARVALHO *et al.*, 2016; KIM *et al.*, 2014). Further, vacancies can significantly increase (close to 1 eV) the binding energy with lithium(GENCAI *et al.*, 2015), when compared with its defect free case. Such propertie makes phosphorene a promising anode material for lithium batteries(GENCAI *et al.*, 2015; AKHTAR *et al.*, 2017). The studies provide in Chapter 3 indicates how feature rich the transport is in phosphorene. By analysing the effects of single and double vacancies defects on the resistances of phosphorene Hall bar, our studies shown that the resistance are most noticeable affected for vacancy types with broken sublattice symmetry, when compared to the pristine system. The use of Hall bar becomes particularly important as the Landau levels in depends strongly on the ribbon orientation(ZHOU *et al.*, 2014), expressed in the leads properties. Also, the presence of quantized plateaus, in the Hall magnetoresistance, only happens in a sufficiently defect free system. In our studies we showed that the formation of Hall plateaus, in a defective system, depends on the type of vacancies. For vacancies with sublattice symmetry (DV2) the Hall plateaus are less affected then for vacancies with broken sublattice symmetry.

Vacancies in graphite are mobile. When a atom is removed it leaves dangling bounds, which undergoes to a Jahn–Teller distortion(TREVETHAN *et al.*, 2014; EL-BARBARY *et al.*, 2003b). This distortion results in a weak reconstructed bond and small out-of-plane atomic displacement(EL-BARBARY *et al.*, 2003b). These mobile vacancies interact with each other and start coalesce forming vacancy pairs and higher order structures(TREVETHAN *et al.*, 2014; YAZYEV; LOUIE, 2010) and they can greatly affects the material properties. Studies on vacancies properties in AA and AB stacks the behaviour of populations of vacancies is dramatically different each other, leading to the

formation of different types vacancies(VUONG *et al.*, 2017).

Although in a *tight-binding* system the Jahn-Teller distortion is neglected, the studies in Chapter 4 showed interesting results concern the vacancies clustering the BLG. We used a vacancy clustering analyses to associate the decrease in zero-modes with the proportional vacancy cluster size (related with defects coalescence). Further we analyse how this behaviour affects the electronic transport properties and how the results differentiates between the AA and AB stacks. Although in our studies we had only considered interlayer coupling between dimmers atoms, one expects that the incorporation of the next-nearest-neighbor interlayer hoppings (such as the skewed hopping γ_3) will not qualitatively change the electronic results, in particular the ones associated with the low-energy spectrum around $E = 0$, e.g. the DOS($E = 0$) results. On the other hand, the electronic transport in the adjacent layer of the BLG nanoribbons should not be drastically affected by point defects created in the other nanoribbon layer. For instance, the near-zero current densities on the adjacent layer due to vacancies on the other layer, as observed in Fig. 4.8 for $\gamma_3 = 0$, should exhibit a pronounced current to the case $\gamma_3 \neq 0$ even for higher values of vacancy densities than the $\gamma_3 = 0$ case and, therefore, leading to non-null conductance values. This can be envisaged from the fact that when removing an atomic site that has a first near-interlayer-neighbor, its connection is also removed, and thus interlayer scattering is hindered, whereas in the presence of interlayer hoppings such interlayer scattering is still allowed.

ADAM, S.; HWANG, E.; GALITSKI, V.; SARMA, S. D. A self-consistent theory for graphene transport. **Proceedings of the National Academy of Sciences**, National Acad Sciences, v. 104, n. 47, p. 18392–18397, 2007.

AKHTAR, M.; ANDERSON, G.; ZHAO, R.; ALRUQI, A.; MROCZKOWSKA, J.; SUMANASEKERA, G.; JASINSKI, J. Recent advances in synthesis, properties, and applications of phosphorene. **npj 2D Mater. and App.**, v. 1, p. 1–13, 12 2017.

AKINWANDE, D.; HUYGHEBAERT, C.; WANG, C.-H.; SERNA, M.; GOOSSENS, S.; LI, L.; WONG, H.-S.; KOPPENS, F. Graphene and two-dimensional materials for silicon technology. **Nature**, v. 573, p. 507–518, 09 2019.

ALLEN, M. T.; MARTIN, J.; YACOBY, A. Gate-defined quantum confinement in suspended bilayer graphene. **Nature Communications**, Nature Publishing Group, v. 3, n. 1, p. 1–6, 2012.

AMINI, M.; SOLTANI, M.; GHANBARI-ADIVI, E.; SHARBAFIUN, M. Tunable transmission due to defects in zigzag phosphorene nanoribbons. **Europhys. Lett.**, IOP Publishing, v. 125, n. 6, p. 67001, Apr 2019. ISSN 1286-4854.

ANINDYA, K. N.; ISLAM, M. S.; PARK, J.; BHUIYAN, A. G.; HASHIMOTO, A. Interlayer vacancy effects on the phonon modes in ab stacked bilayer graphene nanoribbon. **Current Applied Physics**, Elsevier, v. 20, n. 4, p. 572–581, 2020.

ARAUJO, P. T.; TERRONES, M.; DRESSELHAUS, M. S. Defects and impurities in graphene-like materials. **Materials Today**, Elsevier, v. 15, n. 3, p. 98–109, 2012.

ASHCROFT, N. D. M. N. W. **Solid state physics**. [S.l.]: Holt, Rinehart and Winston, 1976. (Solid State Physics). ISBN 9780030839931,0-03-083993-9.

BANDEIRA, N. S.; COSTA, D. R. da; CHAVES, A.; FARIAS, G. A.; FILHO, R. N. C. Gap opening in graphene nanoribbons by application of simple shear strain and in-plane electric field. **Journal of Physics: Condensed Matter**, IOP Publishing, v. 33, n. 6, p. 065503, 2020.

BANHART, F.; KOTAKOSKI, J.; KRASHENINNIKOV, A. V. Structural defects in graphene. **ACS Nano**, ACS Publications, v. 5, n. 1, p. 26–41, 2011.

BASU, S.; BHATTACHARYYA, P. Recent developments on graphene and graphene oxide based solid state gas sensors. **Sensors and Actuators B: Chemical**, v. 173, p. 1–21, 10 2012.

BREY, L.; FERTIG, H. A. Electronic states of graphene nanoribbons studied with the dirac equation. **Physical Review B**, APS, v. 73, n. 23, p. 235411, 2006.

BROCKS, G. **Electron transport at the nanoscale**. [S.l.]: University of Twente, 2005.

BÜTTIKER, M. Four-terminal phase-coherent conductance. **Phys. Rev. Lett.**, American Physical Society, v. 57, p. 1761–1764, Oct 1986.

C., K. **Introduction to Solid State Physics**. [S.l.]: Wiley, 1953.

CAO, Y.; FATEMI, V.; DEMIR, A.; FANG, S.; TOMARKEN, S.; LUO, J.; SANCHEZ-YAMAGISHI, J.; WATANABE, K.; TANIGUCHI, T.; KAXIRAS, E.; ASHOORI, R.; JARILLO-HERRERO, P. Correlated insulator behaviour at half-filling in magic angle graphene superlattices. **Nature**, v. 556, 04 2018.

CARVALHO, A.; RODIN, A. S.; NETO, A. H. C. Phosphorene nanoribbons. **Europhys. Lett.**, IOP Publishing, v. 108, n. 4, p. 47005, nov 2014.

CARVALHO, A.; WANG, M.; ZHU, X.; RODIN, A.; SU, H.; NETO, A. C. Phosphorene: From theory to applications. **Nature Reviews Materials**, v. 1, p. 16061, 08 2016.

CASTELLANOS-GOMEZ, A.; VICARELLI, L.; PRADA, E.; ISLAND, J.; NARASIMHA-ACHARYA, K.; BLANTER, S.; GROENENDIJK, D.; BUSCEMA, M.; STEELE, G.; ALVAREZ, J.; ZANDBERGEN, H.; PALACIOS, J.; ZANT, H. Isolation and characterization of few-layer black phosphorus. **2D Mater.**, v. 1, p. 025001, 08 2014.

CASTRO, E. V.; PERES, N.; SANTOS, J. M. B. L. D.; GUINEA, F.; NETO, A. H. C. Bilayer graphene: gap tunability and edge properties. **Journal of Physics: Conference Series**, v. 129, n. 1, p. 012002, 2008.

CHELI, M.; FIORI, G.; IANNACCONE, G. A semianalytical model of bilayer-graphene field-effect transistor. **IEEE Transactions on Electron Devices**, IEEE, v. 56, n. 12, p. 2979–2986, 2009.

CHEN, F. W.; ILATIKHAMENEH, H.; KLIMECK, G.; RAHMAN, R.; CHU, T.; CHEN, Z. Achieving a higher performance in bilayer graphene fet-strain engineering. In: IEEE. **2015 International Conference on Simulation of Semiconductor Processes and Devices (SISPAD)**. [S.l.], 2015. p. 177–181.

CHEN, P.; LI, N.; CHEN, X.; ONG, W.-J.; ZHAO, X. The rising star of 2d black phosphorus beyond graphene: synthesis, properties and electronic applications. **2D Mater.**, IOP Publishing, v. 5, n. 1, p. 014002, oct 2017.

COSTA, D. R. da; ZARENIA, M.; CHAVES, A.; JR, J. M. P.; FARIAS, G. A.; PEETERS, F. M. Hexagonal-shaped monolayer-bilayer quantum disks in graphene: A tight-binding approach. **Physical Review B**, APS, v. 94, n. 3, p. 035415, 2016.

CUNHA, S. M. **Wave-packet dynamics and electronic transport properties in 2D materials**. Tese (Doutorado) — Centro de Ciências, Universidade Federal do Ceará, 2022.

DATTA, S. **Electronic Transport in Mesoscopic Systems**. [S.l.]: Cambridge University Press, 1995. (Cambridge Studies in Semiconductor Physics and Microelectronic Engineering).

DATTA, S. **Electronic transport in mesoscopic systems**. [S.l.]: Cambridge university press, 1997.

DHANABALAN, S.; PONRAJ, J.; GUO, Z.; LI, S.; BAO, Q. Emerging trends in phosphorene fabrication towards next generation devices. **Adv. Sci.**, v. 4, p. 1600305, 02 2017.

DUTTA, S.; PATI, S. K. Novel properties of graphene nanoribbons: a review. **Journal of Materials Chemistry**, Royal Society of Chemistry, v. 20, n. 38, p. 8207–8223, 2010.

EISBERG, R. R. R. M. **Quantum physics of atoms, molecules, solids, nuclei, and particles**. 2. ed. [S.l.]: New York : Wiley, 2009.

EL-BARBARY, A. A.; TELLING, R. H.; EWELS, C. P.; HEGGIE, M. I.; BRIDDON, P. R. Structure and energetics of the vacancy in graphite. **Physical Review B**, APS, v. 68, n. 14, p. 144107, 2003.

EL-BARBARY, A. A.; TELLING, R. H.; EWELS, C. P.; HEGGIE, M. I.; BRIDDON, P. R. Structure and energetics of the vacancy in graphite. **Phys. Rev. B**, American Physical Society, v. 68, p. 144107, Oct 2003.

EZAWA, M. Topological origin of quasi-flat edge band in phosphorene. **New Journal of Physics**, v. 16, p. 115004, 10 2014.

EZAWA, M. Highly anisotropic physics in phosphorene. **Journal of Physics: Conference Series**, v. 603, p. 012006, 04 2015.

FERRY, D. K.; GOODNICK, S. M.; BIRD, J. **Transport in Nanostructures**. 2. ed. [S.l.]: Cambridge University Press, 2009.

FERRY, D. K.; GOODNICK, S. M.; BIRD, J. **Transport in Nanostructures**. 2. ed. [S.l.]: Cambridge University Press, 2009.

FILHO, R. N. C.; FARIAS, G. A.; PEETERS, F. M. Graphene ribbons with a line of impurities: Opening of a gap. **Physical Review B**, APS, v. 76, n. 19, p. 193409, 2007.

FIORI, G.; BONACCORSO, F.; IANNACCONE, G.; PALACIOS, T.; NEUMAIER, D.; SEABAUGH, A.; BANERJEE, S.; COLOMBO, L. Electronics based on two-dimensional materials. **Nature Nanotechnology**, v. 9, p. 768–779, 10 2014.

FITZPATRICK, R. **Quantum Mechanics**. [S.l.]: The University of Texas, Austin, 2010.

GE, Z.; JOUCKEN, F.; QUEZADA, E.; COSTA, D. R. D.; DAVENPORT, J.; GIRALDO, B.; TANIGUCHI, T.; WATANABE, K.; KOBAYASHI, N. P.; LOW, T.; JR., J. V. Visualization and manipulation of bilayer graphene quantum dots with broken rotational symmetry and nontrivial topology. **Nano Letters**, ACS Publications, v. 20, n. 12, p. 8682–8688, 2020.

GE, Z.; WONG, D.; LEE, J.; JOUCKEN, F.; QUEZADA-LOPEZ, E. A.; KAHN, S.; TSAI, H.-Z.; TANIGUCHI, T.; WATANABE, K.; WANG, F. *et al.* Imaging quantum interference in stadium-shaped monolayer and bilayer graphene quantum dots. **Nano Letters**, ACS Publications, v. 21, n. 21, p. 8993–8998, 2021.

GENCAI, G.; WEI, X.-L.; WANG, D.; LUO, Y.-P.; LIU, L.-M. Pristine and defect phophorene as promising anode materials for rechargeable li batteries. **J. Mater. Chem. A**, v. 3, 04 2015.

GRIFFTHS, D. J. **Mecânica Quântica**. 3. ed. [S.l.]: PEARSON, 2004.

GROTH, C. W.; WIMMER, M.; AKHMEROV, A. R.; WAINTAL, X. Kwant: a software package for quantum transport. **New Journal of Physics**, IOP Publishing, v. 16, n. 6, p. 063065, jun 2014.

GUSEV, G. **Basics of quantum transport**. [S.l.]: Instituto de Física, USP, 2005.

HÄFNER, V.; SCHINDLER, J.; WEIK, N.; MAYER, T.; BALAKRISHNAN, S.; NARAYANAN, R.; BERA, S.; EVERS, F. Density of states in graphene with vacancies: Midgap power law and frozen multifractality. **Physical Review Letters**, American Physical Society, v. 113, p. 186802, Oct 2014.

HAHN, J.; KANG, H. Vacancy and interstitial defects at graphite surfaces: Scanning tunneling microscopic study of the structure, electronic property, and yield for ion-induced defect creation. **Physical Review B**, APS, v. 60, n. 8, p. 6007, 1999.

ITRS. **International Technology Roadmap for Semiconductors(ITRS)**. Http://www.itrs.ieee.org/.

JIANG, Y.; ROLDÁN, R.; GUINEA, F.; LOW, T. Magnetoelectronic properties of multilayer black phosphorus. **Phys. Rev. B**, American Physical Society, v. 92, p. 085408, Aug 2015.

JOUCKEN, F.; BENA, C.; GE, Z.; QUEZADA-LOPEZ, E.; PINON, S.; KALADZHYAN, V.; TANIGUCHI, T.; WATANABE, K.; FERREIRA, A.; JR, J. V. Direct visualization of native defects in graphite and their effect on the electronic properties of bernal-stacked bilayer graphene. **Nano Letters**, ACS Publications, v. 21, n. 17, p. 7100–7108, 2021.

JOUCKEN, F.; BENA, C.; GE, Z.; QUEZADA-LOPEZ, E. A.; DUCASTELLE, F.; TANAGUSHI, T.; WATANABE, K.; JR, J. V. Sublattice dependence and gate tunability of midgap and resonant states induced by native dopants in bernal-stacked bilayer graphene. **Physical Review Letters**, APS, v. 127, n. 10, p. 106401, 2021.

KALADZHYAN, V.; JOUCKEN, F.; GE, Z.; QUEZADA-LOPEZ, E. A.; TANIGUCHI, T.; WATANABE, K.; JR, J. V.; BENA, C. Quasiparticle interference patterns in bilayer graphene with trigonal warping. **Physical Review B**, APS, v. 104, n. 23, p. 235425, 2021.

KALADZHYAN, V.; PINON, S.; JOUCKEN, F.; GE, Z.; QUEZADA-LOPEZ, E. A.; TANIGUCHI, T.; WATANABE, K.; JR, J. V.; BENA, C. Surface states and quasiparticle interference in bernal and rhombohedral graphite with and without trigonal warping. **Physical Review B**, APS, v. 104, n. 15, p. 155418, 2021.

KASIOREK, P. **Moore's Law Is Dead. Now What?** 2021. Https://builtin.com/hardware/moores-law.

KIM, J.-S.; LIU, Y.; ZHU, W.; KIM, S.; WU, d.; TAO, L.; DODABALAPUR, A.; LAI, K.; AKINWANDE, D. Toward air-stable multilayer phosphorene thin-films and transistors. **Scientific reports**, v. 5, 12 2014.

KIRALY, B.; HAUPTMANN, N.; RUDENKO, A.; KATSNELSON, M.; KHAJETOORIANS, A. Probing single vacancies in black phosphorus at the atomic level. **Nano Letters**, v. 17, p. 3607–3612, 02 2017.

KISHIMOTO, K.; OKADA, S. Electron-state tuning of multilayer graphene by defects. **Japanese Journal of Applied Physics**, IOP Publishing, v. 55, n. 6S1, p. 06GF06, 2016.

KNOTHE, A.; FAL'KO, V. Influence of minivalleys and berry curvature on electrostatically induced quantum wires in gapped bilayer graphene. **Physical Review B**, APS, v. 98, n. 15, p. 155435, 2018.

KOSTER, G. F.; SLATER, J. C. Simplified impurity calculation. **Phys. Rev.**, American Physical Society, v. 96, p. 1208–1223, Dec 1954.

KOTAKOSKI, J.; KRASHENINNIKOV, A.; KAISER, U.; MEYER, J. From point defects in graphene to two-dimensional amorphous carbon. **Physical Review Letters**, APS, v. 106, n. 10, p. 105505, 2011.

KRIEGER, J. B.; LAUFER, P. M. Critique of the tight-binding method: Ideal vacancy and surface states. **Phys. Rev. B**, American Physical Society, v. 23, p. 4063–4075, Apr 1981.

LEE, G.-D.; WANG, C.; YOON, E.; HWANG, N.-M.; KIM, D.-Y.; HO, K. Diffusion, coalescence, and reconstruction of vacancy defects in graphene layers. **Physical Review Letters**, APS, v. 95, n. 20, p. 205501, 2005.

LI, L.; YE, G.; TRAN, V.; FEI, R.; CHEN, G.; WANG, H.; WANG, J.; WATANABE, K.; TANIGUCHI, T.; YANG, L.; CHEN, X.; ZHANG, Y. Quantum oscillations in black phosphorus two-dimensional electron gas. **Nature nanotechnology**, v. 10, p. 608–613, 11 2014.

LI, L.; YU, Y.; YE, G.; GE, Q.; XUEDONG, O.; WU, H.; FENG, D.; CHEN, X.; ZHANG, Y. Black phosphorus field-effect transistors. **Nature nanotechnology**, v. 9, p. 372–377, 03 2014.

LI, L. L.; PEETERS, F. M. Quantum transport in defective phosphorene nanoribbons: Effects of atomic vacancies. **Phys. Rev. B**, American Physical Society, v. 97, p. 075414, Feb 2018.

LIU, H.; NEAL, A.; ZHU, Z.; LUO, Z.; XU, X.; TOMANEK, D.; YE, P. Phosphorene: An unexplored 2d semiconductor with a high hole mobility. **ACS nano**, v. 8, p. 4033–4041, 03 2014.

LIU, Y.; LOW, T.; RUDEN, P. P. Mobility anisotropy in monolayer black phosphorus due to scattering by charged impurities. **Phys. Rev. B**, American Physical Society, v. 93, p. 165402, Apr 2016.

LIU, Y.; XU, F.; ZHANG, Z.; PENEV, E.; YAKOBSON, B. Two-dimensional monoelemental semiconductor with electronically inactive defects: The case of phosphorus. **Nano Letters**, v. 14, p. 9917–9938, 08 2014.

LUCCHESE, M.; STAVALE, F.; FERREIRA, E. M.; VILANI, C.; MOUTINHO, M.; CAPAZ, R. B.; ACHETE, C.; JORIO, A. Quantifying ion-induced defects and raman relaxation length in graphene. **Carbon**, v. 48, n. 5, p. 1592–1597, 2010.

MAK, K. F.; LUI, C. H.; SHAN, J.; HEINZ, T. F. Observation of an electric-field-induced band gap in bilayer graphene by infrared spectroscopy. **Physical Review Letters**, APS, v. 102, n. 25, p. 256405, 2009.

MAPASHA, R. E.; IGUMBOR, E.; ANDRIAMBELAZA, N. F.; CHETTY, N. Electronic properties of vacancies in bilayer graphane. **Physica B: Condensed Matter**, Elsevier, v. 573, p. 67–71, 2019.

MCCANN, E. Asymmetry gap in the electronic band structure of bilayer graphene. **Physical Review B**, American Physical Society, v. 74, p. 161403, Oct 2006.

MCCANN, E.; KOSHINO, M. The electronic properties of bilayer graphene. **Reports on Progress in Physics**, IOP Publishing, v. 76, n. 5, p. 056503, 2013.

MILOVANOVIC, S.; MASIR, M. R.; PEETERS, F. Magnetic electron focusing and tuning of the electron current with a pn-junction. **Journal of Applied Physics**, v. 115, p. 043719–043719, 01 2014.

MIRZAKHANI, M.; ZARENIA, M.; KETABI, S. A.; COSTA, D. R. da; PEETERS, F. M. Energy levels of hybrid monolayer-bilayer graphene quantum dots. **Physical Review B**, APS, v. 93, n. 16, p. 165410, 2016.

MOORE, G. E. Cramming more components onto integrated circuits, reprinted from electronics, volume 38, number 8, april 19, 1965, pp.114 ff. **IEEE Solid-State Circuits Society Newsletter**, v. 11, n. 3, p. 33–35, 2006.

MOREAU, N. **Development of a tight-binding model to study Hofstadter's butterfly in graphene on h-BN exhibiting a moiré pattern**. Tese (Doutorado) — École polytechnique de Louvain (EPL), 2017.

MOROZOV, S.; NOVOSELOV, K.; KATSNELSON, M.; SCHEDIN, F.; ELIAS, D.; JASZCZAK, J. A.; GEIM, A. Giant intrinsic carrier mobilities in graphene and its bilayer. **Physical Review Letters**, APS, v. 100, n. 1, p. 016602, 2008.

NASCIMENTO, J.; COSTA, D. R. da; ZARENIA, M.; CHAVES, A.; JR, J. P. Magnetic properties of bilayer graphene quantum dots in the presence of uniaxial strain. **Physical Review B**, APS, v. 96, n. 11, p. 115428, 2017.

NETO, A. C.; GUINEA, F.; PERES, N. M.; NOVOSELOV, K. S.; GEIM, A. K. The electronic properties of graphene. **Reviews of Modern Physics**, APS, v. 81, n. 1, p. 109, 2009.

NETO, A. H. C.; GUINEA, F.; PERES, N. M. R.; NOVOSELOV, K. S.; GEIM, A. K. The electronic properties of graphene. **Reviews of Modern Physics**, APS, v. 81, n. 1, p. 109, 2009.

NOVOSELOV, K.; GEIM, A.; MOROZOV, S.; JIANG, D.; ZHANG, Y.; DUBONOS, S.; GRIGORIEVA, I.; FIRSOV, A. Electric field effect in atomically thin carbon films. **Nat. Mater.**, v. 6, 01 2004.

NOVOSELOV, K. S.; MCCANN, E.; MOROZOV, S.; FAL'KO, V. I.; KATSNELSON, M.; ZEITLER, U.; JIANG, D.; SCHEDIN, F.; GEIM, A. Unconventional quantum hall effect and berry's phase of 2π in bilayer graphene. **Nature Physics**, Nature Publishing Group, v. 2, n. 3, p. 177–180, 2006.

OOSTINGA, J. B.; HEERSCHE, H. B.; LIU, X.; MORPURGO, A. F.; VANDERSYPEN, L. M. Gate-induced insulating state in bilayer graphene devices. **Nature Materials**, Nature Publishing Group, v. 7, n. 2, p. 151–157, 2008.

OSTAHIE, B.; ALDEA, A. Phosphorene confined systems in magnetic field, quantum transport, and superradiance in the quasiflat band. **Phys. Rev. B**, American Physical Society, v. 93, p. 075408, Feb 2016.

OUYANG, Y.; CAMPBELL, P.; GUO, J. Analysis of ballistic monolayer and bilayer graphene field-effect transistors. **Applied Physics Letters**, American Institute of Physics, v. 92, n. 6, p. 063120, 2008.

OVDAT, O.; DON, Y.; AKKERMANS, E. Vacancies in graphene: Dirac physics and fractional vacuum charges. **Physical Review B**, APS, v. 102, n. 7, p. 075109, 2020.

PALACIOS, J.; YNDURÁIN, F. Critical analysis of vacancy-induced magnetism in monolayer and bilayer graphene. **Physical Review B**, APS, v. 85, n. 24, p. 245443, 2012.

PALACIOS, J. J.; FERNÁNDEZ-ROSSIER, J.; BREY, L. Vacancy-induced magnetism in graphene and graphene ribbons. **Physical Review B**, APS, v. 77, n. 19, p. 195428, 2008.

PASSONI, M.; DONATI, F.; BASSI, A. L.; CASARI, C. S.; BOTTANI, C. E. Recovery of local density of states using scanning tunneling spectroscopy. **Phys. Rev. B**, American Physical Society, v. 79, p. 045404, Jan 2009.

Peierls, R. Zur Theorie des Diamagnetismus von Leitungselektronen. **Zeitschrift fur Physik**, v. 80, n. 11-12, p. 763–791, nov. 1933.

PEREIRA, J.; KATSNELSON, M. Landau levels of single layer and bilayer phosphorene. **Physical Review B**, v. 92, p. 075437, 04 2015.

PEREIRA, J. M.; VASILOPOULOS, P.; PEETERS, F. Tunable quantum dots in bilayer graphene. **Nano Letters**, ACS Publications, v. 7, n. 4, p. 946–949, 2007.

PEREIRA, V. M.; SANTOS, J. M. B. Lopes dos; NETO, A. H. C. Modeling disorder in graphene. **Physical Review B**, American Physical Society, v. 77, p. 115109, Mar 2008.

PETROVIĆ, M.; PEETERS, F. Quantum transport in graphene hall bars: Effects of vacancy disorder. **Physical Review B**, APS, v. 94, n. 23, p. 235413, 2016.

PIERRET, R. F. **Semiconductor Fundamentals**. 2. ed. [S.l.]: Purdue University, 1989.

QIAO, J.; KONG, X.; HU, Z.-X.; YANG, F.; JI, W. High-mobility transport anisotropy and linear dichroism in few-layer black phosphorus. **Nature Communications**, Springer Science and Business Media LLC, v. 5, n. 1, p. 4475, Jul 2014. ISSN 2041-1723.

RAKHMANOV, A.; ROZHKOV, A.; SBOYCHAKOV, A.; NORI, F. Instabilities of the aa-stacked graphene bilayer. **Physical Review Letters**, v. 109, p. 206801, 11 2012.

RATHI, S.; LEE, I.; KANG, M.; LIM, D.; LEE, Y.; YAMACLI, S.; JOH, H.-I.; KIM, S.; KIM, S.-W.; YUN, S. J. *et al.* Observation of negative differential resistance in mesoscopic graphene oxide devices. **Scientific Reports**, Nature Publishing Group, v. 8, n. 1, p. 1–9, 2018.

ROY, M. **The Tight Binding method**. [S.l.]: Rutgers School of Arts and Science, 2015.

ROZHKOV, A.; GIAVARAS, G.; BLIOKH, Y. P.; FREILIKHER, V.; NORI, F. Electronic properties of mesoscopic graphene structures: Charge confinement and control of spin and charge transport. **Physics Reports**, Elsevier, v. 503, n. 2-3, p. 77–114, 2011.

ROZHKOV, A. V.; SAVEL'EV, S.; NORI, F. Electronic properties of armchair graphene nanoribbons. **Physical Review B**, APS, v. 79, n. 12, p. 125420, 2009.

ROZHKOV, A. V.; SBOYCHAKOV, A.; RAKHMANOV, A.; NORI, F. Electronic properties of graphene-based bilayer systems. **Physics Reports**, Elsevier, v. 648, p. 1–104, 2016.

RUDENKO, A.; KATSNELSON, M. Quasiparticle band structure and tight-binding model for single- and bilayer black phosphorus. **Physical Review B**, v. 89, p. 201408, 04 2014.

SAFARI, E. K.; SHOKRI, A.; BABAEIPOUR, M. Effects of vacancies on spin-dependent behavior of monolayer and bilayer graphene nanoribbons. **Journal of Magnetism and Magnetic Materials**, Elsevier, v. 441, p. 230–237, 2017.

SAKURAI, J. J. **Modern quantum mechanics**. Rev. ed. [S.l.]: Addison-Wesley Pub. Co, 1994.

SANGWAN, V.; HERSAM, M. Electronic transport in two-dimensional materials. **Annual Review of Physical Chemistry**, v. 69, 02 2018.

SHAH, N. A.; LI, L. L.; MOSALLANEJAD, V.; PEETERS, F. M.; GUO, G.-P. Transport characteristics of multi-terminal pristine and defective phosphorene systems. **Nanotechnology**, IOP Publishing, v. 30, n. 45, p. 455705, aug 2019.

SHEVTSOV, O.; CARMIER, P.; PETITJEAN, C.; GROTH, C.; CARPENTIER, D.; WAINTAL, X. Graphene-based heterojunction between two topological insulators. **Physical Review X**, v. 2, p. 031004, 07 2012.

SLATER, J. C.; KOSTER, G. F. Simplified lcao method for the periodic potential problem. **Phys. Rev.**, American Physical Society, v. 94, p. 1498–1524, Jun 1954.

SON, Y.-W.; COHEN, M. L.; LOUIE, S. G. Energy gaps in graphene nanoribbons. **Physical Review Letters**, APS, v. 97, n. 21, p. 216803, 2006.

SON, Y.-W.; COHEN, M. L.; LOUIE, S. G. Half-metallic graphene nanoribbons. **Nature**, Nature Publishing Group, v. 444, n. 7117, p. 347–349, 2006.

SOUSA, D. J. P. **Propriedades eletrônicas do fosforeno**. Tese (Doutorado) — Centro de Ciências, Universidade Federal do Ceará, 2018.

SOUSA, D. J. P. de; CASTRO, L. V. de; COSTA, D. R. da; PEREIRA, J. M.; LOW, T. Multilayered black phosphorus: From a tight-binding to a continuum description. **Phys. Rev. B**, American Physical Society, v. 96, p. 155427, Oct 2017.

STAMPFER, C.; FRINGES, S.; GÜTTINGER, J.; MOLITOR, F.; VOLK, C.; TERRÉS, B.; DAUBER, J.; ENGELS, S.; SCHNEZ, S.; JACOBSEN, A. *et al.* Transport in graphene nanostructures. **Frontiers of Physics**, Springer, v. 6, n. 3, p. 271–293, 2011.

STEGMAN, T. **Quantum transport in nanostructures**. Tese (Doutorado) — Von der Fakultät für Physik der Universität Duisburg-Essen, 2014.

SZAFRANEK, B. N.; SCHALL, D.; OTTO, M.; NEUMAIER, D.; KURZ, H. High on/off ratios in bilayer graphene field effect transistors realized by surface dopants. **Nano Letters**, ACS Publications, v. 11, n. 7, p. 2640–2643, 2011.

SZE, K. K. N. S. **Physics of Semiconductor Devices**. [S.l.]: Wiley-Interscience, 2006. ISBN 9780471143239.

TAHIR, M.; VASILOPOULOS, P.; PEETERS, F. M. Magneto-optical transport properties of monolayer phosphorene. **Phys. Rev. B**, American Physical Society, v. 92, p. 045420, Jul 2015.

TAKAGAKI, Y.; WAKAYA, F.; TAKAOKA, S.; GAMO, K.; MURASE, K.; NAMBA, S. Fabrication of ballistic quantum wires and their transport properties. **Japanese Journal of Applied Physics**, v. 28, p. 2188–2192, 10 1989.

TELLING, R. H.; EWELS, C. P.; AHLAM, A.; HEGGIE, M. I. Wigner defects bridge the graphite gap. **Nature Materials**, Nature Publishing Group, v. 2, n. 5, p. 333–337, 2003.

TREVETHAN, T.; LATHAM, C. D.; HEGGIE, M. I.; BRIDDON, P. R.; RAYSON, M. J. Vacancy diffusion and coalescence in graphene directed by defect strain fields. **Nanoscale**, The Royal Society of Chemistry, v. 6, p. 2978–2986, 2014.

VUONG, A.; TREVETHAN, T.; LATHAM, C.; EWELS, C.; ERBAHAR, D.; BRIDDON, P.; RAYSON, M.; HEGGIE, M. Interlayer vacancy defects in aa-stacked bilayer graphene: density functional theory predictions. **Journal of Physics: Condensed Matter**, IOP Publishing, v. 29, n. 15, p. 155304, 2017.

WAKABAYASHI, K.; SASAKI, K.-I.; NAKANISHI, T.; ENOKI, T. Electronic states of graphene nanoribbons and analytical solutions. **Science and Technology of Advanced Materials**, IOP Publishing, v. 11, n. 5, p. 054504, 2010.

WAKABAYASHI, K.; TAKANE, Y.; YAMAMOTO, M.; SIGRIST, M. Electronic transport properties of graphene nanoribbons. **New Journal of Physics**, IOP Publishing, v. 11, n. 9, p. 095016, 2009.

WEINGART, S.; BOCK, C.; KUNZE, U.; SPECK, F.; SEYLLER, T.; LEY, L. Low-temperature ballistic transport in nanoscale epitaxial graphene cross junctions. **Applied Physics Letters**, v. 95, p. 262101, 10 2009.

WEISS, N. O.; ZHOU, H.; LIAO, L.; LIU, Y.; JIANG, S.; HUANG, Y.; DUAN, X. Graphene: an emerging electronic material. **Advanced Materials**, Wiley Online Library, v. 24, n. 43, p. 5782–5825, 2012.

WEIßE, A.; WELLEIN, G.; ALVERMANN, A.; FEHSKE, H. The kernel polynomial method. **Reviews of Modern Physics**, American Physical Society (APS), v. 78, n. 1, p. 275, Mar 2006.

XIA, F.; FARMER, D. B.; LIN, Y.-m.; AVOURIS, P. Graphene field-effect transistors with high on/off current ratio and large transport band gap at room temperature. **Nano Letters**, ACS Publications, v. 10, n. 2, p. 715–718, 2010.

XU, H.; HEINZEL, T.; ZOZOULENKO, I. Edge disorder and localization regimes in bilayer graphene nanoribbons. **Physical Review B**, APS, v. 80, n. 4, p. 045308, 2009.

YAGMURCUKARDES, M.; PEETERS, F. M.; SENGER, R. T.; SAHIN, H. Nanoribbons: From fundamentals to state-of-the-art applications. **Applied Physics Reviews**, AIP Publishing LLC, v. 3, n. 4, p. 041302, 2016.

YANG, L.; PARK, C.-H.; SON, Y.-W.; COHEN, M. L.; LOUIE, S. G. Quasiparticle energies and band gaps in graphene nanoribbons. **Physical Review Letters**, APS, v. 99, n. 18, p. 186801, 2007.

YAZYEV, O. V.; LOUIE, S. G. Topological defects in graphene: Dislocations and grain boundaries. **Phys. Rev. B**, American Physical Society, v. 81, p. 195420, May 2010.

YOON, J.; LEE, Z. Effective passivation of black phosphorus under ambient conditions. **Applied Microscopy**, v. 47, p. 176–186, 09 2017.

YU, W. J.; DUAN, X. Tunable transport gap in narrow bilayer graphene nanoribbons. **Scientific Reports**, Nature Publishing Group, v. 3, n. 1, p. 1–5, 2013.

YUAN, S.; RUDENKO, A. N.; KATSNELSON, M. I. Transport and optical properties of single- and bilayer black phosphorus with defects. **Phys. Rev. B**, American Physical Society, v. 91, p. 115436, Mar 2015.

ZAWADZKI, W.; RUSIN, T. Nature of electron zitterbewegung in crystalline solids. **Physics Letters A**, v. 374, p. 3533–3537, 07 2010.

ZHANG, Y.; TANG, T.-T.; GIRIT, C.; HAO, Z.; MARTIN, M. C.; ZETTL, A.; CROMMIE, M. F.; SHEN, Y. R.; WANG, F. Direct observation of a widely tunable bandgap in bilayer graphene. **Nature**, Nature Publishing Group, v. 459, n. 7248, p. 820–823, 2009.

ZHOU, X.; ZHANG, R.; SUN, J.; ZOU, Y.; ZHOU, G.; ZHAI, F.; CHANG, K. Landau levels and magneto-transport property of monolayer phosphorene. **Scientific reports**, v. 5, p. 12295, 11 2014.

ZWIERZYCKI, M.; KHOMYAKOV, P.; STARIKOV, A. A.; XIA, K.; TALANANA, M.; XU, P. X.; KARPAN, V.; MARUSHCHENKO, I.; TUREK, I.; BAUER, E. W.; BROCKS, G.; KELLY, P. J. Calculating scattering matrices by wave function matching. **Physica Status Solidi B**, v. 245, n. 4, p. 623–640, 2008.

ÇAKıR, D.; SEVIK, C.; PEETERS, F. M. Significant effect of stacking on the electronic and optical properties of few-layer black phosphorus. **Phys. Rev. B**, American Physical Society, v. 92, p. 165406, Oct 2015.

APPENDIX A - WAVE FUNCTION MATCHING THECHNIQUE FOR QUANTUM TRANSPORT CALCULATIONS

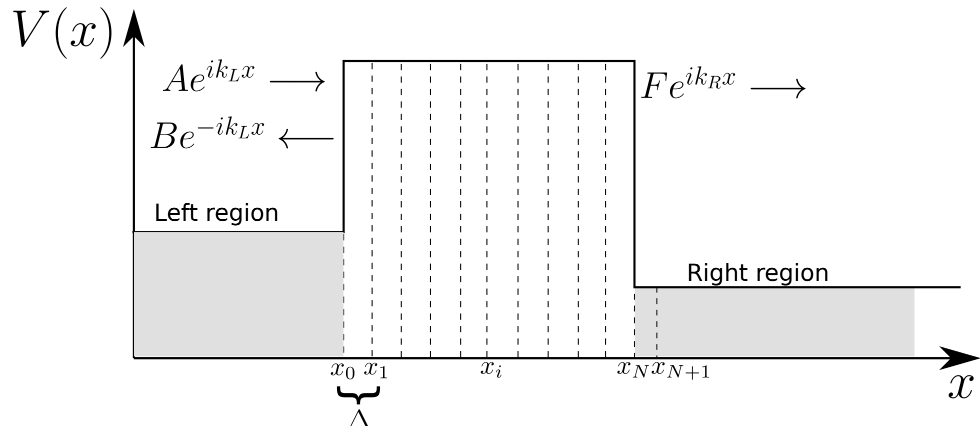

Figure 7.1: Finte difference representation of the scattering problem. To discretize the system a grid of equals size $\Delta = x_{i+1} - x_i$. The scattering potential is define inside the region $x_0 < x < x_N$.

By considering a simple one dimensional problem (as define in Fig. 7.1), we are going to introduce the mode matching technique to solve a scattering problem(BROCKS, 2005). Le's consider the first order finite difference of the Schrödinger equation(EISBERG, 2009),

$$E\psi_i + \frac{\hbar^2}{2m}\left(\frac{(\psi_{i+1} - \psi_i) - (\psi_i - \psi_{i-1})}{\Delta^2}\right) - V_i\psi_i = 0, \tag{7.1}$$

where ψ_i and V_i is discretize form of the wavefunction and electrons potential, and $\Delta = x_{i+1} - x_i$. For the left and right regions, the solutions of the Schrödinger equation are simple plane waves, with,

$$k_L = \frac{\sqrt{2m(E - V_L)}}{\hbar}; k_R = \frac{\sqrt{2m(E - V_R)}}{\hbar}. \tag{7.2}$$

Our job is to match the "modes" 7.2 to the wavefunctions in the regions of the scattering region. We will consider the origin of the scaterrgin region at $x_0 = 0$. The finite difference Schrödinger equation for $i = 0$ is,

$$E\psi_0 + \frac{\hbar^2}{2m\Delta^2}\left[\psi_1 - 2\psi_0 + \psi_{-1}\right] - V_0\psi_0 = 0. \tag{7.3}$$

The wavefunction on the left side ($x < 0$) is given by, $\psi_{-1} = Ae^{-k_L\Delta} + Be^{k_L\Delta}$. As the wavefunction must be continuos at $x = 0$

$$\psi_{-1} = Ae^{-k_L\Delta} + (\psi_0 - A)e^{k_L\Delta}. \tag{7.4}$$

With this, Eq. becomes,

$$E\psi_0 + \frac{\hbar^2}{2m\Delta^2}\left[\psi_1 - 2\psi_0 + e^{ik_L\Delta}\psi_0\right] - V_0\psi_0 = \frac{\hbar^2}{2m\Delta^2}A(e^{ik_L\Delta} - e^{-ik_L\Delta}). \tag{7.5}$$

The term on right hand can be considered as the source of the income wave.

On the right side of the scattering regio, at the boundary $i = N+1$, the Eq. 7 is writen as,

$$E\psi_{N+1} + \frac{\hbar^2}{2m\Delta^2}[\psi_{N+2} - 2\psi_{N+1} + \psi_N] - V_{N+1}\psi_{N+1} = 0. \tag{7.6}$$

Assuming that the wavefunction is only "transmitted" (no income wave from the right region),

$$\psi_{N+2} = Fe^{ik_R(N+2)\Delta} = \psi_{N+1}e^{ik_R\Delta}. \tag{7.7}$$

Equation 7 on the right region is defined as,

$$E\psi_{N+1} + \frac{\hbar^2}{2m\Delta^2}\left[\psi_{N+1}e^{ik_R\Delta} - 2\psi_{N+1}\psi_N\right] - V_{N+1}\psi_{N+1} = 0 \tag{7.8}$$

By combining Eqs. 7, 7.6 and 7.8, where Eq. 7 is used to defines the system for $i = 1, \cdot, N$, we can summarize the problem as,

$$(E\boldsymbol{I} - \boldsymbol{H})\boldsymbol{\psi}) = \boldsymbol{q}. \tag{7.9}$$

contains the coefficients ψ_i, for $i = 0, \cdot, N+1$. $\boldsymbol{q}$ is the define "source" vector with $N+1$, where all entries are zero, except,

$$q_0 = \frac{\hbar^2}{2m\Delta^2}A[e^{ik\Delta} - e^{-ik\Delta}]. \tag{7.10}$$

The Hamiltonian $\boldsymbol{H}$ is a $(N+2)x(N+2)$ matrix where all off diagonal matrix are zero except the sub- and super-diagonal,

$$H_{i,i+1} = H_{i,i-1} = -\frac{\hbar^2}{2m\Delta}, \tag{7.11}$$

and diagonal elementes, which are all equals,

$$H_{i,i} = -\frac{\hbar^2}{m\Delta^2} + V_i, \tag{7.12}$$

except the first and the last one,

$$H_{0,0} = -\frac{\hbar^2}{m\Delta^2} + V_0 + \Sigma_L(E), \tag{7.13}$$

$$H_{N+1,N+1} = -\frac{\hbar^2}{m\Delta^2} + V_{N+1} + \Sigma_R(E). \tag{7.14}$$

The terms,

$$\Sigma_L(E) = -\frac{\hbar^2}{2m\Delta^2} e^{ik_L\Delta},$$
$$\Sigma_R(E) = -\frac{\hbar^2}{2m\Delta^2} e^{ik_R\Delta}, \tag{7.15}$$

aree the self-energies of the left and right leads. They are responsible to proper couple the scattering region and the outer regions, and contains all the information the leads.

After solving Eq. 7.9, we can calculate the transmission and reflection amplitudes. The transmission amplitude is given bu wavefunction at the right side of the scattering region, normalized to the incoming wave, and normalized with the velocities,

$$t = \sqrt{\frac{v_R}{v_L}} \frac{{}_{N+1}}{A}. \tag{7.16}$$

The reflection amplitude can be determined from the wavefunction on the left side minus the incoming wave, normalized to the incoming wave,

$$r = \frac{\psi_0 - A}{A}. \tag{7.17}$$

To determine the velocities, we can look at the discretize expression for the current,

$$j = \frac{i\hbar}{2m} \left({}_i \frac{{}^*_{i+1} - {}^*_i}{\Delta} - {}^*_i \frac{\psi_{i+1} - \psi_i}{\Delta} \right). \tag{7.18}$$

For a simple plane wave $\psi_i = Ae^{ik\Delta}$, Eq. 7.18 leads to,

$$j = \frac{i\hbar^2 |A|^2}{2m\Delta} (e^{-ik\Delta} - e^{ik\Delta}). \tag{7.19}$$

From the de Broglie's relation $p = \hbar k$ for particle's momentum, from which we can find the velocity,

$$v = \frac{p}{m} = \frac{\hbar k}{m}, \tag{7.20}$$

By comparing Eq. 7.19 with Eqs. 2.28 and 7.20, we can find,

$$v = \frac{i\hbar}{2m\Delta}(e^{-ik\delta} - e^{ik\Delta}). \tag{7.21}$$

Then Eq. 7.10 can be simplified as,

$$q_0 = \frac{i\hbar A}{\Delta} v_L. \tag{7.22}$$

Combining Eqs. 7.15 and 7.20, the velocities and self-energies can be related,

$$v_{L/R} = \frac{2\Delta}{\hbar}\Sigma_{L/R}(E). \tag{7.23}$$

APPENDIX B - PUBLISHED ARTICLES

Hall and bend resistance of a phosphorene Hall bar

L. P. Miranda,[1,2,*] S. P. Milovanović,[2] R. N. Costa Filho,[1] and F. M. Peeters[2]
[1]*Departamento de Física, Universidade Federal do Ceará, Campus do Pici, 60455-760 Fortaleza, Ceará, Brazil*
[2]*Department of Physics, University of Antwerp, Groenenborgerlaan 171, B-2020 Antwerp, Belgium*

(Received 1 April 2021; revised 31 May 2021; accepted 11 June 2021; published 1 July 2021)

The dependence of the Hall and bend resistances on a perpendicular magnetic field and on vacancy defects in a four-terminal phosphorene single layer Hall bar is investigated. A tight-binding model in combination with the Landauer-Büttiker formalism is used to calculate the energy spectrum, the lead-to-lead transmissions, and the Hall and bend resistances of the system. It is shown that the terminals with zigzag edge orientation are responsible for the absence of quantized plateaus in the Hall resistance and peaks in the longitudinal resistance. A negative bend resistance in the ballistic regime is found due to the presence of high- and low-energy transport modes in the armchair and zigzag terminals, respectively. The system density of states, with single vacancy defects, shows that the presence of in-gap states is proportional to the number of vacancies. Quantized plateaus in the Hall resistance are only formed in a sufficiently clean system. The effects of different kinds of vacancies where the plateaus are destroyed and a diffusive regime appears in the bend resistance are investigated.

APPENDIX C - ONGOING ARTICLES

Vacancy clustering effect on the electronic and transport properties of bilayer graphene nanoribbons

L. P. Miranda,[1,*] D. R. da Costa,[1,†] F. M. Peeters,[2,‡] and R. N. Costa Filho[1,§]

[1] *Departamento de Física, Universidade Federal do Ceará, Campus do Pici, Fortaleza, Ceará, Brazil*
[2] *Department of Physics, University of Antwerp, Groenenborgerlaan 171, B-2020 Antwerp, Belgium*
(Dated: March 12, 2022)

Experimental realizations of two-dimensional materials are hardly free of structural defects such as e.g. vacancies, which, in turn, modify drastically its pristine physical defect-free properties. In this work, we explore effects due to point defect clustering on the electronic and transport properties of bilayer graphene nanoribbons, for AA and AB stacking and zigzag and armchair boundaries, by means of the tight-binding approach and scattering matrix formalism. Evident vacancy concentration signatures exhibiting a threshold amplitude and an universality regardless of the system size, stacking and boundary types, in the density of states around the zero-energy level are observed. Our results are explained via the coalescence analysis of the strong sizeable vacancy clustering effect in the system and the breaking of the inversion symmetry at high vacancy densities, demonstrating a similar density of states for two equivalent degrees of concentration disorder, below and above the threshold value.